Design and Implementation of a Battery Management System (BMS): Software and Hardware Development

A thesis submitted in fulfilment of the requirements

for the degree of Master of Science in Electrical Engineering

by

Amine Kraiem

Université du Québec en Outaouais

Mitacs Research Internship

Ciena Corporation

DEPARTMENT OF COMPUTER SCIENCE AND ENGINEERING

UNIVERSITÉ DU QUÉBEC EN OUTAOUAIS

November 2025

Certificate

It is certified that the work contained in this thesis entitled **"Design and Implementation of a Battery Management System (BMS): Software and Hardware Development"** by **Amine Kraiem** has been carried out under my supervision and that it has not been submitted elsewhere for a degree.

Prof. Larbi Talbi

Supervisor

Professor

CSE Department

Université du Québec en Outaouais

Dr. Tahar Haddad

Co-Supervisor

Senior Analog Engineer

Ciena Corporation

Declaration

This is to certify that the thesis titled **"Design and Implementation of a Battery Management System (BMS): Software and Hardware Development"** has been authored by me. It presents the research conducted by me under the supervision of **Prof. Larbi Talbi**. and **Dr. Tahar Haddad**.

To the best of my knowledge, it is an original work, both in terms of research content and narrative, and has not been submitted elsewhere, in part or in full, for a degree. Further, due credit has been attributed to the relevant state-of-the-art and collaborations with appropriate citations and acknowledgments, in line with established norms and practices.

Amine Kraiem
Roll No. KRAA18119907
CSE Department
Université du Québec en Outaouais

Abstract

Name of the student: **Amine Kraiem** Roll No: **KRAA18119907**

Degree for which submitted: **MSc** Department: **CSE Department**

Thesis title: **Design and Implementation of a Battery Management System (BMS): Software and Hardware Development**

Thesis supervisors: **Prof. Larbi Talbi** and **Dr. Tahar Haddad**

Month and year of thesis submission: **November 2025**

This thesis addresses the modelling, estimation, and hardware development of a Battery Management System for a 60 V lithium-ion battery pack used in electric scooter applications. A Dual Polarization equivalent circuit model was selected for its balance of accuracy and computational efficiency, and was formulated in the Laplace domain to enable stable, real-time embedded implementation. State of Charge dependent lookup tables were constructed from Open Circuit Voltage and pulse-response data to capture nonlinear cell behaviour. An enhanced Coulomb Counting method with Open Circuit Voltage based drift correction was developed, and MATLAB/Simulink simulations confirmed close agreement between model predictions and expected voltage responses under dynamic loading. To support future embedded deployment, a complete centralized Battery Management System hardware architecture was designed, including the STM32H563 microcontroller, the BQ76952 analog front end, current and temperature sensing circuits, MOSFET-based protection stages, and a compact 2-layer PCB.

The thesis establishes a validated modelling framework and a ready-to-integrate hardware platform, forming the foundation for subsequent firmware development, prototyping, and experimental validation on a physical e-scooter battery system.

Acknowledgements

I would like to express my sincere gratitude to my research director, Professor Larbi Talbi, for his continuous guidance, mentorship, and support throughout the course of this research. His insights were invaluable in shaping the direction of this thesis.

I am deeply thankful to Dr. Tahar Haddad for his commitment, technical guidance, and continuous support. Through his affiliation with Ciena, he facilitated a fruitful collaboration that enabled the applied and industrial dimensions of this work to flourish.

This thesis was carried out as part of a collaborative research internship between the Université du Québec en Outaouais (UQO), Ciena, and the Mitacs Accelerate program. The project was financially supported by Ciena, whose contribution made this work possible. I would especially like to thank Dr. Sadok Aouini, Director at Ciena, and Dr. Naim Ben-Hamida, Senior Director at Ciena, for their vision, encouragement, and support of this initiative.

I also wish to thank Professor Javad Fattahi from the University of Ottawa for his valuable insights and support during the course of this work.

I am grateful to my colleagues and collaborators for their stimulating discussions, critical feedback, and unwavering support. Their contributions were instrumental in overcoming technical challenges and advancing the project.

Finally, I extend my heartfelt thanks to my family and friends for their constant encouragement, patience, and belief in me. Their support has been a cornerstone of this journey.

Contents

List of Figures

List of Tables

Abbreviations

ADC	Analog-to-Digital Converter
AFE	Analog Front End
ANN	Artificial Neural Network
BMS	Battery Management System
CAN	Controller Area Network
CBD	Computational Battery Dynamics
DEC	Diethyl Carbonate
DMC	Dimethyl Carbonate
DP	Dual Polarization
EC	Ethylene Carbonate
EV	Electric Vehicle
HV	High Voltage
LCO	Lithium Cobalt Oxide
LFP	Lithium Iron Phosphate
LMO	Lithium Manganese Oxide
LTO	Lithium Titanate

MCU	Microcontroller Unit
NCA	Nickel Cobalt Aluminum
NiCd	Nickel Cadmium
NiMH	Nickel Metal Hydride
NMC	Nickel Manganese Cobalt
OCV	Open-Circuit Voltage
PE	Polyethylene
PNGV	Partnership for a New Generation of Vehicles
PP	Polypropylene
SEI	Solid Electrolyte Interphase
SOC	State of Charge
SOE	State of Energy
SOP	State of Power
SOF	State of Function
SOH	State of Health
DOD	Depth of Discharge
UPS	Uninterruptible Power Supply

Chapter 1

Introduction

1.1 Background

In the 21st century, batteries have become indispensable in powering modern life, enabling the operation of an extensive range of electronic devices, from consumer electronics such as mobile phones, laptops, and power tools to more advanced applications like electric vehicles and large-scale energy storage systems. Notably, Electric Vehicles (EVs) have emerged as the leading clean transportation solution, eliminating tailpipe emissions while reducing dependence on fossil fuels. Modern EVs leverage high-capacity lithium-ion batteries capable of delivering 300-400 km ranges per charge, with rapid charging technologies enabling 80% capacity in under 30 minutes. As industries and governments push toward electrification to reduce carbon emissions and enhance energy sustainability, the demand for efficient and reliable battery technology has surged.

Among the various rechargeable battery chemistries, lithium-ion batteries have emerged as the dominant solution due to their high energy density, long cycle life, and efficiency in energy conversion. These batteries are widely used in electric vehicles, where performance, longevity, and safety are critical factors. However, despite their advantages, lithium-ion batteries are subject to degradation over time due to factors such as overcharging, over-discharging, extreme temperatures, and frequent charge-discharge cycles. Such degradation not only reduces energy storage capacity but also impacts the economic and environmental sustainability of battery-powered applications.

To address these challenges, Battery Management Systems (BMSs) have become an essential component in modern battery-powered devices. A BMS is an intelligent electronic

control system designed to monitor and regulate key battery parameters such as voltage, current, state of charge, state of health, and temperature. By continuously assessing these factors, a BMS ensures battery safety, prevents hazardous conditions like thermal runaway, and optimizes battery performance to extend its lifespan. Advanced battery management solutions leverage real-time data processing and control strategies to improve battery efficiency and reliability, making them indispensable in applications requiring long-term energy storage.

1.2 Motivation

The increasing reliance on lithium-ion batteries for critical applications such as electric vehicles, renewable energy storage, and smart grids presents both opportunities and challenges. While the demand for these batteries continues to rise, their production remains resource-intensive, relying on materials like lithium, cobalt, and nickel, which are finite and often subject to geopolitical and economic constraints. This has heightened the urgency for battery lifecycle optimization, where extending battery lifespan and improving energy efficiency can significantly reduce costs and environmental impact.

One of the primary ways to achieve this optimization is through the development of advanced battery management technologies, which require improvements in both hardware and software. On the hardware side, the integration of high-performance microcontrollers, sensors, power management circuits, and custom-designed printed circuit boards can significantly enhance battery monitoring and control precision. Additionally, wireless communication modules and embedded systems are increasingly being incorporated to enable remote diagnostics and real-time monitoring.

On the software side, the application of machine learning algorithms, predictive analytics, and advanced control strategies can improve state of charge estimation accuracy, optimize charge-discharge cycles, and implement predictive maintenance techniques. The use of digital twins, cloud computing, and artificial intelligence-driven analytics further enhances the ability to detect anomalies, predict failures, and adapt charging strategies in real time. These innovations in both hardware and software development are essential for improving the reliability, efficiency, and longevity of battery systems.

Given that battery packs are one of the most expensive components of electric vehicles and other large-scale applications, even a small improvement in battery longevity can translate into substantial financial savings. For instance, extending battery life by just five percent

could save billions of dollars annually in the electric vehicle industry alone. Furthermore, as grid-scale energy storage and decentralized power solutions continue to evolve, there is a growing need for intelligent, adaptive, and highly efficient battery management solutions that can integrate seamlessly into smart energy networks.

The convergence of hardware advancements, software innovations, and intelligent control algorithms is shaping the future of battery technology. Ensuring the sustainability of these systems requires a holistic approach that combines precise hardware engineering with sophisticated software development to balance performance, longevity, and safety effectively.

1.3 Problem Statement

Lithium-ion battery packs present unique challenges due to their high energy density and susceptibility to degradation and hazardous failure modes. These batteries are prone to rapid performance decline, thermal instability, and safety risks when exposed to abusive conditions such as overcharging, over-discharging, or thermal imbalance. Their sensitivity requires continuous monitoring and control to ensure safe and reliable operation across a range of applications.

One of the foundational challenges in ensuring the safety and performance of lithium-ion batteries is the absence of a physical testing platform that allows for controlled experimentation under critical operating conditions. Direct testing under extreme scenarios, such as rapid charge/discharge rates, overheating, or deep cycling, poses considerable safety risks. This creates a need for a simulated environment that can replicate battery behavior and enable the study of its response under such conditions without physical hazard. However, building such simulation models that accurately reflect real-world behaviors remains difficult due to limitations in data availability, model complexity, and parameter accuracy.

Beyond simulation, the design of control algorithms for monitoring key battery states introduces further challenges. Accurate estimation of internal battery parameters, specifically State of Charge (SOC) and State of Health (SOH), is central to battery management. Yet these parameters are not directly measurable and must be estimated using indirect methods. Commonly used approaches like Coulomb Counting and Open-Circuit Voltage (OCV) estimation are plagued by limitations such as cumulative drift, dependence on rest conditions, and poor performance during dynamic operation.

Model-based estimation techniques, especially those relying on Kalman Filters, are widely used for SOC estimation but introduce challenges related to model sensitivity, numerical stability, and real-time feasibility. These methods often depend on simplified battery models, which do not fully capture dynamic system behavior, and require finely tuned parameters that are difficult to calibrate and validate across different battery chemistries and operating conditions.

Simultaneously, the physical hardware necessary to support real-time estimation and control presents its own set of constraints. Many embedded systems used in battery applications suffer from limited processing power, restricted memory, and insufficient sensor resolution. These limitations make it difficult to implement and execute advanced estimation algorithms with the accuracy and speed required for safety-critical applications. Inadequate integration of communication protocols and protective functions further compromises system performance and scalability.

1.4 Organization of the Thesis

This thesis establishes the theoretical, modelling, and preliminary hardware foundations required for building a complete BMS for a 60 V electric scooter battery pack. Chapter 1 introduces the context of lithium-ion energy storage, the challenges associated with battery safety and monitoring, and the motivation for developing an advanced BMS. Chapter 2 presents an extensive literature review on lithium-ion cell chemistry, battery modelling approaches, SOC and SOH estimation methods, and BMS hardware architectures. This chapter establishes the theoretical background used throughout the thesis. Chapter 3 outlines the general and specific objectives of the work, defining the expected contributions in both modelling and hardware development. Chapter 4 describes the research methodology, including the modelling workflow, the data-driven parameter identification process, and the simulation tools used for validation. Chapter 5 develops the Dual Polarization (2RC) equivalent circuit model, formulates it in the Laplace domain, and validates it through MATLAB/Simulink simulations using pulse-current test profiles. Chapter 6 introduces the SOC estimation approach based on Advanced Coulomb Counting with OCV-based drift correction and demonstrates its behaviour through simulation. Chapter 7 presents the system-level hardware design of the centralized BMS, including the AFE, microcontroller, sensing circuits, protection circuitry, power management, and the complete two-layer PCB

layout tailored for e-scooter integration. Chapter 8 concludes this thesis by summarizing the main contributions and outlining future work, including firmware implementation, hardware prototyping, and experimental testing on an actual e-scooter battery system.

Chapter 2

Literature Review

This chapter presents a comprehensive overview of the existing research landscape in battery modeling, SOC and SOH estimation techniques, as well as hardware development for BMSs. It aims to provide the necessary background to understand the technological evolution and current challenges in intelligent battery monitoring and control systems, ultimately framing the research gaps this thesis aims to address.

2.1 Architecture and System Integration of BMSs

BMS play a vital role in the safe and efficient operation of lithium-ion battery systems, particularly in demanding applications such as electric vehicles, renewable energy storage, and aerospace systems. The BMS interfaces with multiple hardware and software components arranged in a layered and scalable architecture that starts from individual cells and extends to full battery packs.

Figure 2.1 illustrates a comprehensive system view, showing the flow from electrochemical battery cells to modules, the formation of battery packs, and the integration of sensing, control, and estimation mechanisms via the BMS.

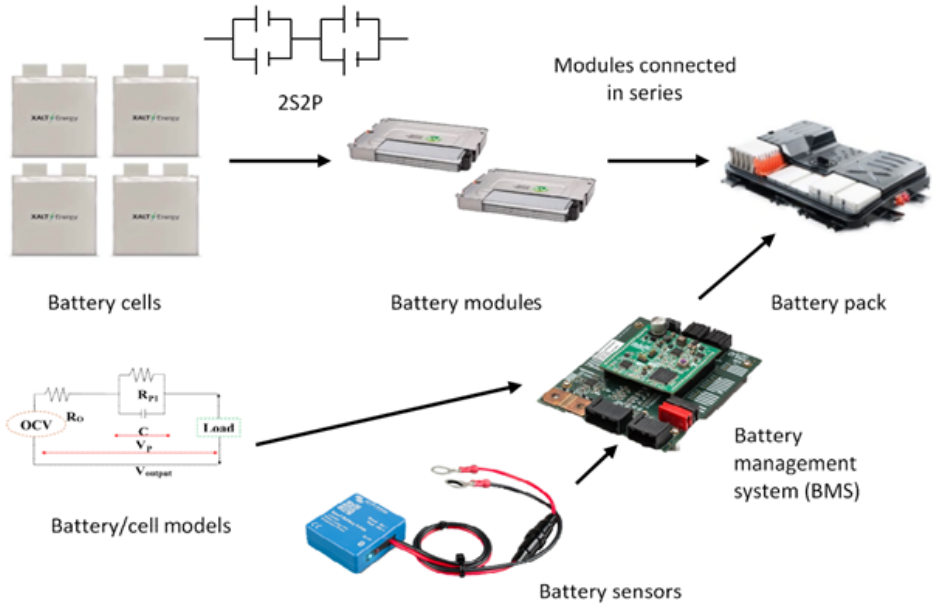

FIGURE 2.1: Overview of a battery system: cell modeling, 2S2P module configuration, pack integration, BMS controller, and sensors.

At the foundation of the system are the battery cells, the basic energy storage units. These are grouped into a 2S2P configuration, two cells connected in series to increase voltage and two such series connected in parallel to enhance capacity, resulting in battery modules. These modules are then connected in series to form a complete battery pack, delivering the voltage and energy required by the end application, such as an electric drivetrain.

To manage this complex architecture, a BMS is deployed to oversee all critical operational aspects. The BMS is connected to a network of sensors that continuously measure temperature, voltage, and current across cells and modules. These real-time measurements are used as inputs to embedded estimation algorithms based on cell models, typically implemented as equivalent electrical circuits (e.g., Thevenin models). These models act as digital twins of the battery's electrochemical behavior, enabling accurate prediction of internal states such as the SOC and SOH.

This estimation feeds into a control loop where the BMS actively monitors and regulates the battery system. It performs safety checks, thermal management, overcharge and over-discharge protection, and balancing between cells to ensure uniform performance. The closed-loop interaction, measurement, modeling, estimation, and control, ensures that the system remains within safe operating limits, optimizes energy usage, and extends battery lifespan.

In essence, this architecture represents the backbone of intelligent battery system integration. It reflects how individual hardware components and software models are orchestrated to create a reliable, scalable, and autonomous energy system suitable for real-world deployment. This section lays the foundation for the following chapters, where more detailed analyses of battery cell behavior, modeling techniques, and estimation algorithms will be explored.

High-Level Input-Output Architecture

A BMS operates by acquiring key physical measurements and using them to infer the internal states of the battery and control its operation. As illustrated in Figure 2.2, the BMS receives three primary input signals: temperature (T), voltage (V), and current (I). These measurements are processed through embedded algorithms to estimate critical outputs such as the SOC, SOH, and overall operational status.

FIGURE 2.2: Simplified I/O architecture of a BMS: inputs (T, V, I) drive estimation of SOC, SOH, and system status.

This structure highlights the model-based nature of a modern BMS, while internal states like SOC and SOH cannot be directly measured, they can be inferred using mathematical models, sensor data, and estimation algorithms. The accurate calculation of these states is crucial to ensure safety, prolong battery lifespan, and improve system performance.

Functional Overview of a BMS

The BMS plays a central role in monitoring, protecting, and optimizing battery operation. It ensures the safety, reliability, and longevity of battery packs by executing essential functions, including:

- **Voltage Monitoring:** Continuously measures the voltage of individual cells to prevent overvoltage and undervoltage conditions.

- **Current Monitoring:** Tracks current flows to detect overcurrent and short circuits, enabling immediate protective responses.
- **Temperature Monitoring:** Monitors cell and pack temperatures to prevent overheating, thermal imbalance, and runaway risks.
- **State Estimation:** Accurately estimates the SOC and SOH using model-based or data-driven algorithms.
- **Balancing Control:** Executes active or passive cell balancing strategies to minimize inconsistencies among cells, thereby improving performance and lifespan.
- **Charger and Protection Control:** Interfaces with external chargers and embedded protection circuits to manage the charging process safely.

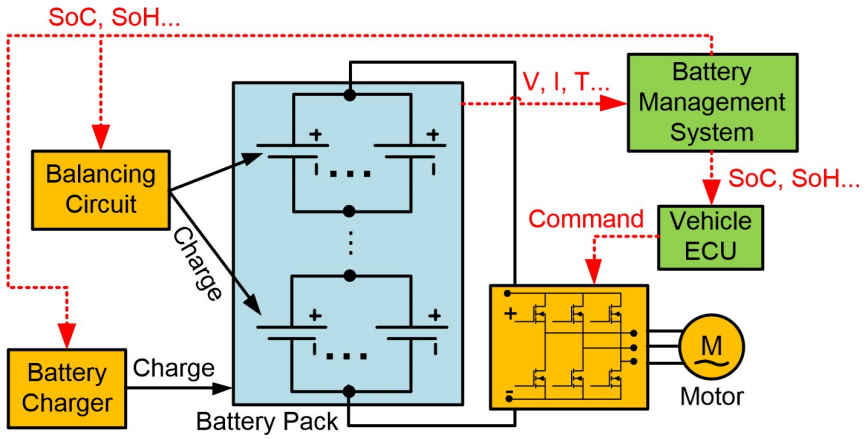

FIGURE 2.3: Main functions of a BMS.

From the functions listed above, the core task of a BMS is to estimate the internal states of the battery such as SOC and SOH. Due to the difficulty in direct measurement, state estimation is based on the battery model and control algorithms in the BMS software, which is considered one of the key technologies of EVs. In practice, incorrect SOC estimation can result in high SOC variation, reduced lifespan, and lower energy efficiency. Likewise, inaccurate SOH estimation can impact maintenance decisions and degrade SOC accuracy.

2.2 Battery Technology

An electric battery is a system made up of one or more electrochemical cells that may supply electricity to external loads through external terminals. Even though the term "battery"

is used frequently, its basic unit is the individual "cell." This indicates that, depending on the application and the necessary voltage and capacity, Cells can be connected in parallel, series or a combination of the two.

2.2.1 Classification of Cells and Batteries

Electrochemical cells and batteries are primarily classified as primary (non-rechargeable) or secondary (rechargeable) systems [1].

- **Primary cells:** These are designed for single-use applications and are not intended to be recharged after their initial depletion. These batteries are generally lightweight, cost-effective, and offer high energy density at low to moderate discharge rates. Due to their convenience and long shelf life, primary batteries are commonly used in consumer electronics, medical equipment, remote sensors, and other low-duty applications where rechargeability is not required.
- **Secondary cells:** These are, in contrast, rechargeable and reusable. They are capable of sustaining hundreds to thousands of charge-discharge cycles depending on their chemistry, construction quality, and usage conditions. Examples of secondary battery chemistries include lithium-ion, lead-acid, Nickel Cadmium (NiCd), and Nickel Metal Hydride (NiMH). These batteries serve as energy storage systems in EVs, aerospace and satellite applications, and uninterruptible power supplies Uninterruptible Power Supply (UPS). They are also widely used in portable electronics, power tools, and other applications requiring a rechargeable power source.

2.2.2 Electrical Characteristics of Cells and Batteries

The performance and application of a battery are fundamentally determined by several electrical parameters [1].

- **Voltage (Standard Cell Potential):** The standard potential of an electrochemical cell is determined by the types of active materials used at the electrodes. It is calculated as the sum of the oxidation potential of the anode and the reduction potential of the cathode, mathematically expressed as:

  $$\text{Standard Cell Potential} = \text{Anode (oxidation potential)} + \text{Cathode (reduction potential)} \tag{2.1}$$

This value provides the theoretical voltage available from a fully charged cell under standard conditions.

- **Nominal voltage:** This refers to the average operating voltage of a cell under standard discharge conditions. It varies with battery chemistry, for example, 2.1 V for lead-acid, 1.2–1.35 V for nickel-based cells, and over 3.0 V for lithium-ion cells.
- **Charge capacity:** This is expressed in ampere-hours (Ah) and defines the total quantity of electric charge a battery can store and deliver. It determines how long a battery can supply current before it must be recharged.
- **Series configuration:** Cells are connected end-to-end such that their voltages add up, while the overall capacity remains equal to that of a single cell. This configuration is used to increase the total voltage of the battery pack without changing the available charge capacity.
- **Parallel configuration:** Cells are connected side-by-side such that their capacities add up, while the overall voltage remains equal to that of a single cell. This configuration is used to increase the total charge capacity of the battery pack without altering the system voltage.

2.2.3 Energy and Power Capabilities:

This subsection introduces key terms used to describe the energy and power behavior of batteries. Understanding these definitions is essential for evaluating battery performance and selecting appropriate technologies for specific applications [1], [2].

- **Power (W):** The instantaneous rate at which energy is delivered or consumed. It is defined as the product of voltage and current: $P = V \times I$.
- **Power density (W/L):** The maximum power output per unit volume of the battery. It indicates how much power a battery can deliver relative to its physical size and is useful for space-constrained applications.
- **Specific power (W/kg):** The maximum power output per unit mass of the battery. It is a critical metric for applications where weight is a limiting factor, such as electric vehicles and aerial systems.

- **Energy (Wh or J):** The total amount of electrical work a battery can perform. It represents the integral of power over time and reflects the battery's ability to sustain a load.
- **Capacity (Ah):** The total amount of electric charge a battery can store and deliver. It is a fundamental measure of how long a battery can supply current before needing to be recharged.
- **Energy capacity (Wh):** The maximum amount of energy that a battery is designed to store when fully charged. It is calculated as the product of nominal voltage and charge capacity: $E = V_{\text{nom}} \times Q$.
- **Energy density (Wh/L):** The total energy stored per unit volume. It is used to compare batteries in applications where space optimization is important.
- **Specific energy (Wh/kg):** The total energy stored per unit mass. This metric determines how much energy a battery can store for a given weight and is especially relevant for portable and transportation applications.

Batteries with higher specific energy and energy density are preferred in applications requiring light weight or compact size, though they may involve more reactive and less stable chemical materials.

2.2.4 Practical vs. Theoretical Energy Output:

- **Theoretical energy output:** This is the ideal energy a battery could deliver based on chemical composition.
- **Practical energy output:** In reality, only about 25% to 35% of the theoretical energy is typically available. This discrepancy is caused by voltage inefficiencies, internal resistance, and non-reactive cell materials like packaging and separators.

Understanding this difference is critical for accurate and realistic system design [1].

2.2.5 Battery Terminology :

Characterizing battery performance under practical operating conditions requires an understanding of the relationship between C-rate, discharge behavior, voltage parameters, and the technical specifications critical for system integration [3].

2.2.5.1 Battery Condition :

- **C-rate:** This is a normalized expression of the rate at which a battery is charged or discharged. A 1C rate means the battery will be fully discharged in one hour. A 0.5C rate means the battery will discharge in two hours, while a 2C rate discharges it in 30 minutes. Discharging at high C-rates increases internal heating and reduces the effective capacity due to resistive losses.
- **Cut-off voltage:** This is the minimum terminal voltage to which a battery should be discharged to avoid damage and ensure long-term performance.
- **OCV:** The voltage across the terminals when no external load is applied.
- **Working voltage:** Also called terminal voltage, this is the voltage under load. It varies with current and SOC.
- **Depth of Discharge (DOD):** The percentage of the battery's total capacity that has been used. A DOD: of 80% or more is considered a deep discharge.
- **SOC:** The current charge level of a battery as a percentage of its full capacity. It is commonly estimated through current integration or voltage-based methods.
- **SOH:** A measure of the battery's condition compared to its original performance. It reflects factors like capacity loss, increased resistance, and reduced efficiency.
- **Internal resistance:** The inherent opposition to current flow within the battery, which affects voltage drop and heat generation.
- **Self-discharge:** A phenomenon in which the battery loses capacity over time due to internal chemical reactions, even when not connected to a load.

2.2.5.2 Battery Technical Specifications:

Battery technical specification sheets provide standardized metrics used to describe the electrical and operational characteristics of individual cells, battery modules, and complete packs. These specifications are crucial for proper battery selection, accurate modeling, and safe integration into energy systems.

- **Nominal Voltage:** The average voltage a battery maintains during a full discharge cycle, typically measured at a standard discharge rate (e.g., 0.2C). It represents the "normal" voltage used in system design and performance calculations.

- **Cut-off Voltage:** The minimum terminal voltage allowed during discharge. Discharging below this value can cause irreversible damage to the cell and degrade long-term performance.
- **Discharge curve:** This represents the variation in terminal voltage as the battery discharges over time or state of charge.
- **Nominal Capacity (Ah):** The total charge that a battery can deliver at a specified discharge current. It is computed by multiplying the discharge current (A) by discharge time (h). Capacity typically decreases at higher C-rates due to losses.
- **Nominal Energy (Wh):** The total energy a battery can deliver when discharged at a defined rate. It is calculated as the product of power (W) and time (h). Like capacity, available energy also decreases at higher discharge rates.
- **Cycle Life:** The number of complete charge-discharge cycles a battery can sustain before its capacity falls below a set threshold, commonly 80% of its initial value. Cycle life is dependent on battery chemistry, temperature, depth of discharge, charge/discharge rates, and environmental conditions.
- **Maximum Continuous Discharge Current:** The maximum current a battery can supply continuously without overheating or accelerating degradation. This value is set by the manufacturer and is vital for defining operational limits in high-load scenarios.

2.2.6 Types of Cell Construction

The mechanical packaging and form factor of lithium-ion cells also influence their thermal, electrical, and mechanical performance in applications [4].

- **Cylindrical:** Most commoditized and mature form, especially in 18650 and 21700 formats. Provides robust structure and is widely used in consumer electronics and power tools.
- **Prismatic:** Housed in rigid aluminum or steel cans, offering higher packaging efficiency and better safety features such as pressure relief vents. Common in automotive packs.

- **Pouch:** Lightweight and flexible, offering the highest energy density per volume. However, they require careful mechanical support within battery modules to prevent swelling and failure.

The three primary lithium-ion cell form factors are illustrated in Figure 2.4.

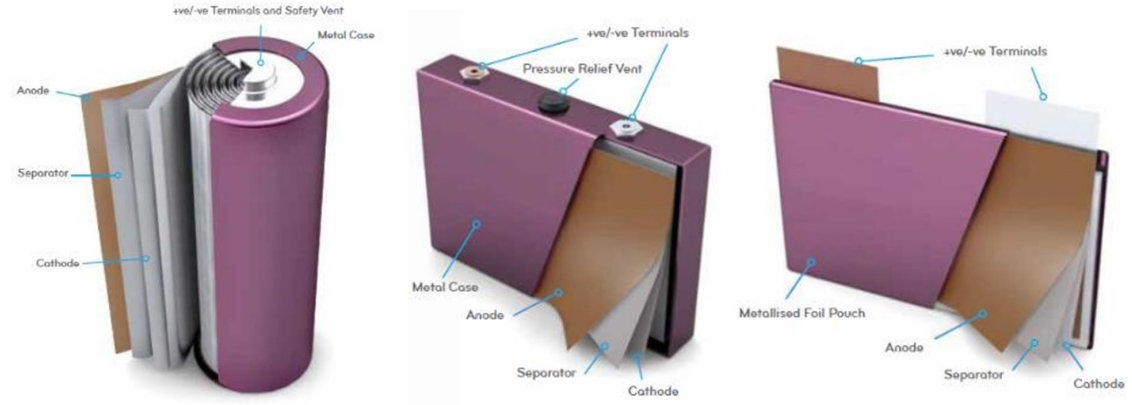

FIGURE 2.4: Cell Types: Cylindrical, Prismatic, Pouch

2.2.7 Electrochemical Cell Structure and Operation

Electrochemical cells function by converting chemical energy into electrical energy through controlled redox reactions between materials with differing electrochemical potentials. This section presents the internal structure of these cells, their modes of operation, and a particular focus on lithium-ion technology due to its critical role in modern energy systems [2].

2.2.7.1 Internal Components of Electrochemical Cells:

Traditional electrochemical cells operate based on reduction–oxidation (redox) reactions involving active material transformations. These reactions occur between a negative electrode (where oxidation occurs during discharge) and a positive electrode (where reduction occurs during discharge), facilitated by an electrolyte and separated by an ionically conductive separator. A schematic representation of a general electrochemical cell is shown in Figure 2.5 [2].

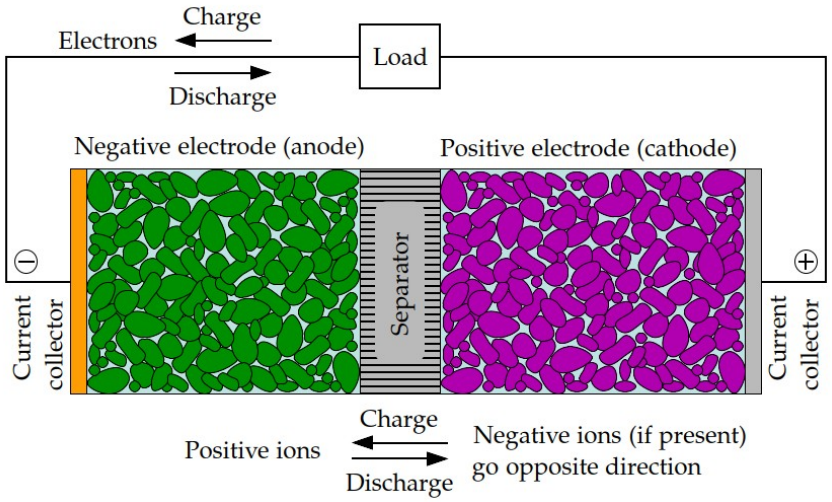

FIGURE 2.5: Schematic diagram of electrochemical cell

Key internal components include:

- **Negative electrode:** Releases electrons during discharge (oxidation) and absorbs them during charging.
- **Positive electrode:** Accepts electrons during discharge (reduction) and releases them during charging.
- **Electrolyte:** A conductive medium (liquid or solid) that allows ions to move between electrodes but blocks electrons.
- **Separator:** A porous barrier that prevents electrodes from touching while letting ions pass through.
- **Current collectors:** Metal foils or grids that carry electrons between electrodes and the external circuit.

2.2.7.2 Example – Lead-Acid Battery: Discharge and Charge Processes:

In a lead-acid battery, both electrodes are composed of lead compounds immersed in a sulfuric acid electrolyte. The reactions involve a traditional redox process where materials are consumed and regenerated during cycling [2].

Electrochemical reactions during discharge:

During discharge, metallic lead at the negative electrode oxidizes to form lead sulfate ($PbSO_4$), releasing electrons (e^-) into the external circuit. Simultaneously, lead dioxide (PbO_2) at the positive electrode is reduced to lead sulfate ($PbSO_4$) by consuming sulfate ions (${SO_4}^{2-}$), protons (H^+), and incoming electrons. Electrons flow externally from the negative to the positive electrode, generating usable electrical energy. Internally, the concentration of sulfuric acid (H_2SO_4) in the electrolyte decreases while water content increases, resulting in a lower electrolyte density.

The detailed half-reactions are as follows:

- **Oxidation reaction at the negative electrode:**

$$\mathrm{Pb_{(s)} + SO^{2-}_{4(aq)} \rightleftharpoons PbSO_{4(s)} + 2\,e^-} \tag{2.2}$$

- **Reduction reaction at the positive electrode:**

$$\mathrm{PbO_{2(s)} + SO^{2-}_{4(aq)} + 4\,H^+_{(aq)} + 2\,e^- \rightleftharpoons PbSO_{4(s)} + 2\,H_2O_{(l)}} \tag{2.3}$$

- **Overall Redox Reaction:**

  Combining the two half-reactions, the overall reaction during discharging is:

$$\mathrm{Pb_{(s)} + PbO_{2(s)} + 2\,H_2SO_{4(aq)} \rightleftharpoons 2\,PbSO_{4(s)} + 2\,H_2O_{(l)}} \tag{2.4}$$

Electrochemical Reactions During Charge:

During charging, the above reactions are reversed. Lead sulfate ($PbSO_4$) at the negative electrode is reduced back to solid lead (Pb), and lead sulfate ($PbSO_4$) at the positive electrode is oxidized back into lead dioxide (PbO_2). Concurrently, the sulfuric acid (H_2SO_4) concentration in the electrolyte increases, restoring the battery's active chemical composition.

Over time, however, repeated charge-discharge cycling, natural self-discharge, and side reactions progressively alter the structure of the electrodes. In particular, the growth of irreversible large lead sulfate crystals, loss of active material, and degradation of the electrode surfaces contribute to the aging and capacity fading of lead-acid batteries.

2.2.7.3 Lithium-Ion Cells and Their Operation

While traditional electrochemical cells fundamentally rely on chemical transformations of the active materials during each cycle, lithium-ion technology introduced a revolutionary mechanism based on intercalation and deintercalation processes. Instead of significant chemical alteration, lithium-ion cells shuttle lithium ions between the positive and negative electrodes without major structural change to the host material, resulting in higher energy and power densities, much longer cycle life, and improved thermal stability and efficiency. During discharge, lithium atoms at the negative electrode release electrons to the external circuit and become lithium ions (Li^+) that migrate through the electrolyte toward the positive electrode, where they recombine with electrons and intercalate into the crystal structure of the positive electrode. During charging, an external voltage drives the reverse process, where electrons flow from the positive to the negative electrode externally, and lithium ions move internally through the electrolyte, re-intercalating into the negative electrode material. Thus, lithium-ion cells rely on reversible ionic movement and intercalation, rather than the bulk material consumption and regeneration typical of traditional batteries. A schematic representation of this mechanism is provided in Figure 2.6 [1], [2].

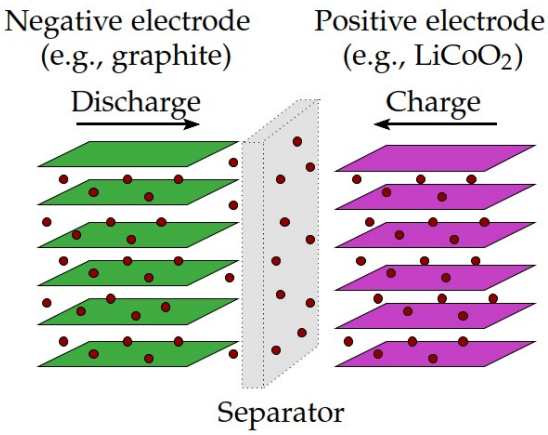

FIGURE 2.6: Simplified schematic of lithium-ion cell operation

Electrochemical Reactions in Lithium-Ion Batteries

Lithium-ion batteries operate based on reversible redox reactions involving lithium ions shuttling between the negative and positive electrodes through the electrolyte. While the fundamental mechanism remains the same, lithium insertion and removal, the specific electrochemical reactions vary depending on the electrode materials used.

Negative Electrode (Graphite)

Discharge (lithium deintercalation):

$$\mathrm{LiC_6} \rightarrow \mathrm{C_6} + \mathrm{Li^+} + \mathrm{e^-} \tag{2.5}$$

Charge (lithium intercalation):

$$\mathrm{C_6} + \mathrm{Li^+} + \mathrm{e^-} \rightarrow \mathrm{LiC_6} \tag{2.6}$$

Positive Electrode (Lithium Metal Oxide, e.g., $\mathbf{LiCoO_2}$)

Discharge (lithium deintercalation):

$$\mathrm{LiCoO_2} \rightarrow \mathrm{CoO_2} + \mathrm{Li^+} + \mathrm{e^-} \tag{2.7}$$

Charge (lithium intercalation):

$$\mathrm{CoO_2} + \mathrm{Li^+} + \mathrm{e^-} \rightarrow \mathrm{LiCoO_2} \tag{2.8}$$

Overall Reversible Cell Reaction

Combining the half-cell reactions, the overall reversible electrochemical reaction of the lithium-ion cell can be expressed as:

$$\mathrm{LiC_6} + \mathrm{CoO_2} \rightleftharpoons \mathrm{C_6} + \mathrm{LiCoO_2} \tag{2.9}$$

Material-Dependent Reactions and Voltage Behavior

Although the underlying mechanism is always based on lithium intercalation and deintercalation, the exact chemical reactions and resulting open-circuit voltages (OCV) vary depending on the electrode materials. For instance:

- Lithium Iron Phosphate (LFP) cells tend to exhibit a flat voltage plateau over a wide range of SOC.

- NMC (Nickel Manganese Cobalt), Nickel Cobalt Aluminum (NCA), and Lithium Cobalt Oxide (LCO) exhibit sloped voltage curves.

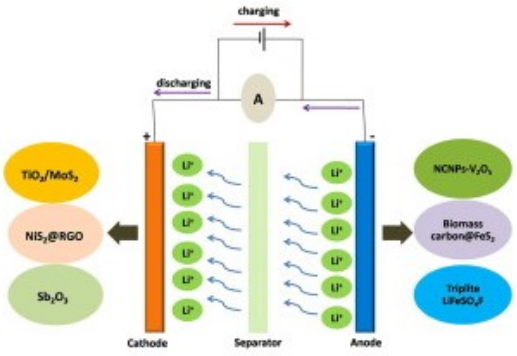

FIGURE 2.7: Schematic of lithium-ion battery showing lithium-ion movement between electrodes during charge and discharge.

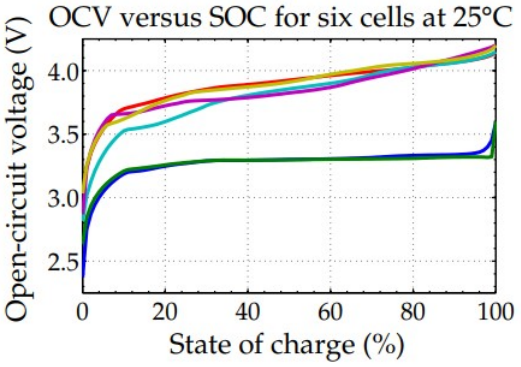

FIGURE 2.8: OCV versus SOC for six cells at 25°C showing material-dependent voltage behavior.

As shown in Figure 2.8, different cells exhibit distinct OCV-SOC profiles due to their cathode and anode material combinations. The two lowest curves correspond to different types of LFP cells from separate manufacturers, while the top four curves represent various high-energy chemistries such as LCO, NMC, and NCA.

Moreover, this OCV-SOC relationship is temperature-dependent. As temperature affects the thermodynamic equilibrium and ionic mobility within the cell, the OCV must be modeled as a function of both SOC and temperature:

$$\text{OCV} = f\big(z(t), T(t)\big) \tag{2.10}$$

This dependency becomes especially important when the battery is used in dynamic environments. Future models will integrate $T(t)$ explicitly into the battery model and SOC estimation logic.

Key Components and Their Roles

TABLE 2.1: Key Components of a Lithium-Ion Cell

Component	**Material Examples**	**Key Characteristics**
Negative Electrode (Anode)	Graphite (C_6), Lithium Titanate ($Li_4Ti_5O_{12}$), Silicon-based	High cyclability (graphite), fast charging (Lithium Titanate (LTO)), high capacity (silicon)
Positive Electrode (Cathode)	$LiCoO_2$ (LCO), Nickel Manganese Cobalt (NMC), LFP, Lithium Manganese Oxide (LMO), NCA	Determines voltage, capacity, thermal behavior, and cost
Electrolyte	$LiPF_6$ in Ethylene Carbonate (EC)/Dimethyl Carbonate (DMC)/Diethyl Carbonate (DEC), $LiBF_4$, $LiClO_4$	High ionic conductivity, electrochemical stability, must not react with electrodes
Separator	Polyethylene (PE), Polypropylene (PP), Ceramic-coated PE	Microporous, thermally shut-down capable, chemically inert
Current Collectors	Copper foil (negative), Aluminum foil (positive)	High electrical conductivity, chemically stable, lightweight, electrochemically inert

2.2.8 Traditional vs. Modern Battery Chemistries

The table 2.2 compares the most common battery chemistries used across different generations of applications. The data reflects their electrical characteristics, performance metrics, environmental impact, and application suitability [4]:

TABLE 2.2: Comparison of Traditional and Modern Battery Chemistries

Chemistry	**Voltage (V)**	**Specific Energy (Wh/kg)**	**Cycle Life**	**Self-Discharge (%/month)**	**Toxicity**	**Applications**
Lead-Acid	∼2.0	30–40	200–400	3–4	High (Lead)	SLI, UPS, E-bikes
NiCd	∼1.2	35–80	300–1000	15–20	Very High (Cadmium)	Aerospace, Medical, Legacy Devices
NiMH	∼1.2	55–110	500–1000	15–30	Moderate	Hybrid EVs, Tools, Electronics
Li-Ion	2.4–3.8	100–300	>2000	2–3	Low to Moderate	EVs, Laptops, Power Tools

2.2.9 Lithium-Ion Advantages

Lithium-ion batteries dominate modern energy storage due to their superior electrochemical characteristics. Their performance has enabled widespread application across electric vehicles, renewable energy systems, and portable electronics. The key advantages include:

- **High specific energy** (up to 230 Wh/kg) and **energy density** (up to 600 Wh/L), making them ideal for space- and weight-sensitive applications.
- **High nominal voltage** (around 3.6 V), which reduces the number of cells required in a battery pack.
- **Excellent power density** (up to 5000 W/kg), supporting high-performance load demands.
- **Low self-discharge rate**, typically less than 3% per month, enhancing storage efficiency.
- **No memory effect**, allowing flexible and partial charging cycles without performance loss.

- **Wide operating temperature range**, functioning reliably from –30°C to +70°C.
- **Fast charging capability**, achieving up to 80% charge in under one hour at 1C rates.
- **Long cycle life**, enduring more than 2000 full charge-discharge cycles or over 5000 shallow cycles.

These advantages explain the extensive integration of lithium-ion batteries in modern technologies where performance, compactness, and longevity are critical.

2.3 Modeling and Estimation Techniques for BMS

2.3.1 Battery Modeling Techniques

As discussed in Section 2.1, one of the fundamental roles of a BMS is to estimate internal battery states such as SOC and SOH. These internal parameters are not directly measurable via sensors. Instead, developing control and estimation algorithms requires a reference model, commonly known as a *plant model*, which acts as a virtual replica of the actual battery. Constructed within a simulation environment, this model allows the BMS algorithms to be tested under extreme or hazardous conditions, such as thermal abuse, overcharging, or high C-rate discharges, that would be unsafe to reproduce with actual hardware. Once validated, these algorithms are embedded into the BMS microcontroller to manage the real battery system.

Battery modeling also enables advanced analyses such as thermal performance evaluation, structural layout optimization, and airflow simulation during battery pack design. By mimicking the internal physical, chemical, and electrical processes of the battery in a virtual environment, engineers can optimize performance and reliability, shorten development cycles, and reduce the need for costly prototyping.

Li-ion battery models in most literature can be mainly divided into three categories: electrochemical models, black-box models, and equivalent circuit models (ECMs). Each of these categories varies in fidelity, computational demand, and suitability for integration within real-time systems. In what follows, we discuss each of these modeling approaches.

2.3.1.1 Electrochemical Models

Electrochemical models, also known as principle-based models, are rooted in the fundamental physics and chemistry of the battery. These models simulate intricate electrochemical reactions and transport phenomena in electrodes and electrolytes. They typically involve solving partial differential equations (PDEs), which account for species concentration, potential distribution, and reaction kinetics.

Notable contributions include the porous electrode model developed by J. S. Newman [5] and subsequent advancements by Doyle, Fuller, and Wang [6, 7, 8]. C. Y. Wang also introduced a multiscale framework known as Computational Battery Dynamics (CBD) [9], and M. Doyle developed simplified 1D isothermal models [10]. V. R. Subramanian further refined these models under galvanostatic conditions [11].

Although accurate, these models require extensive parameterization and are computationally expensive, limiting their feasibility in embedded real-time applications.

2.3.1.2 Black-Box Models

Black-box models treat the battery as a system whose internal mechanisms are unknown or too complex to model directly. Instead, they use statistical or machine learning methods to learn the mapping between input-output relationships based on experimental data.

These models include polynomial regressions, support vector machines (SVM), fuzzy logic systems, and Artificial Neural Network (ANN). For example, J. P. Wang developed nonlinear black-box models using SVM [12] and fuzzy neural networks [13]. While black-box models can capture highly nonlinear dynamics and are useful when physical parameters are unavailable, they require extensive, high-quality training data and may suffer from poor generalization when tested outside the trained operating window.

Moreover, many black-box models lack physical interpretability and robustness, especially in edge cases. For these reasons, while informative for pattern recognition and anomaly detection, black-box models are not widely favored for core BMS estimation tasks where reliability and transparency are paramount.

2.3.1.3 Equivalent Circuit Models (ECMs)

Equivalent Circuit Models (ECMs) are behavior-based models that approximate the battery's electrical response using resistors, capacitors, and voltage sources. These models simplify the complex physical behavior of the battery into a format that is computationally efficient and easy to integrate into BMS firmware.

Min Chen proposed an ECM capable of predicting both I–V characteristics and runtime [14], while G. L. Plett developed a family of ECMs incorporating dynamic elements such as hysteresis and self-correction to enhance accuracy [15]. The flexibility of ECMs allows for parameter tuning based on real-world measurements, and their state-space formulation facilitates real-time estimation using Kalman filtering techniques.

2.3.2 State Estimation Algorithms

As established in Section 2.3.1.3, Equivalent Circuit Models (ECMs) provide a robust and practical foundation for implementing state estimation algorithms within embedded BMS [14, 15]. In line with the core functionalities outlined in Section **??**, one of the most critical responsibilities of the BMS is the estimation of internal battery states, particularly the SOC and SOH.

In addition to these primary state variables, advanced BMS architectures may also compute secondary metrics such as State of Energy (SOE), State of Power (SOP), and State of Function (SOF). However, SOC and SOH remain the cornerstones of battery diagnostics and control strategies due to their direct influence on safety, performance, and service life [16].

2.3.2.1 SOC Estimation

As introduced in Section 2.2.5.1, SOC represents the battery's charge level as a percentage of its full usable capacity. It plays a fundamental role in energy planning, vehicle range estimation, and protection against operational extremes like over-discharge or overcharge [17, 15]. A reliable SOC estimate allows for optimal energy utilization and ensures system longevity by regulating the battery's usable capacity within safe limits.

2.3.2.2 SOH Estimation

As also defined in Section 2.2.5.1, the SOH is a diagnostic metric that reflects the battery's ability to store and deliver energy relative to its original condition. It typically quantifies degradation through capacity fade or internal resistance growth over time [18, 19, 17]. Accurate SOH estimation facilitates condition-based monitoring, helping prevent failures and enabling strategic maintenance planning to maximize the battery's service life.

2.3.2.3 SOE and SOP Estimations

SOE represents the total energy currently stored within the battery, while SOP estimates its ability to deliver or absorb power instantaneously under present operating conditions. These parameters are key to dynamic power management and safe allocation of energy resources. Accurate SOE and SOP estimations ensure that performance demands are met without violating the thermal and electrical constraints of the battery system [20, 16].

2.3.2.4 SOF Estimation

SOF characterizes the battery's operational readiness by integrating variables such as SOC, temperature, and voltage. This state defines real-time limits on allowable current draw, offering multiple thresholds, such as recommended operating limits, safety limits, and maximum safe boundaries. SOF estimation helps dynamically regulate battery output to prevent failures and safeguard the battery against potentially damaging conditions [21, 22].

The development and implementation of algorithms for estimating these state estimations will be explored in detail in subsequent chapters, with a focus on their real-time integration into BMS control frameworks based on ECM models.

2.4 Hardware Design Considerations in BMS

As highlighted in Section 2.1, the BMS is required to ensure the safety, reliability, and optimal performance of lithium-ion battery packs, particularly in critical applications like electric vehicles. This is achieved through a suite of core functionalities, including voltage, current, and temperature monitoring, state estimation, cell balancing, and protection

control. However, the successful execution of these tasks relies not only on robust software algorithms but also on the availability of an appropriate and dependable hardware platform.

The importance of the hardware design stems from its role as the physical infrastructure that enables real-time data acquisition, secure computation, and effective actuation. High-fidelity estimation algorithms and control strategies can only function as intended if they are supported by precise sensors, efficient microcontrollers, and reliable communication interfaces. Therefore, transitioning from modeling and estimation to hardware design is a critical step in bridging theoretical development with practical deployment.

This section provides an overview of the key considerations and architectural choices made in the development of the BMS hardware, which serves as the foundation for implementing the proposed battery management strategies.

2.4.1 Generic Block Diagram of a BMS

A generic BMS architecture typically consists of a battery pack connected to both protective and sensing hardware elements distributed across its positive and negative terminals. On the positive side, common components include a fuse, a Hall-effect current sensor, and a series of contactors, such as a pre-charge contactor, pre-charge resistor, and a High Voltage (HV) positive contactor. On the negative side, devices like a pyro fuse, a precision shunt sensor, and a negative HV contactor are employed.

All these components are linked via an HV connector to external systems, such as the on-board charger. Central to this system is the BMS controller, a dedicated electronic control unit that continuously monitors operating conditions, makes safety-critical decisions, and regulates energy flow. This integrated setup enables the BMS to protect the battery from faults such as overcurrent, thermal excursions, or unsafe voltages.

An illustrative diagram of this complete system architecture is presented in Figure 2.9, which outlines the interconnection between protective devices, sensors, the controller, and the high-voltage interfaces.

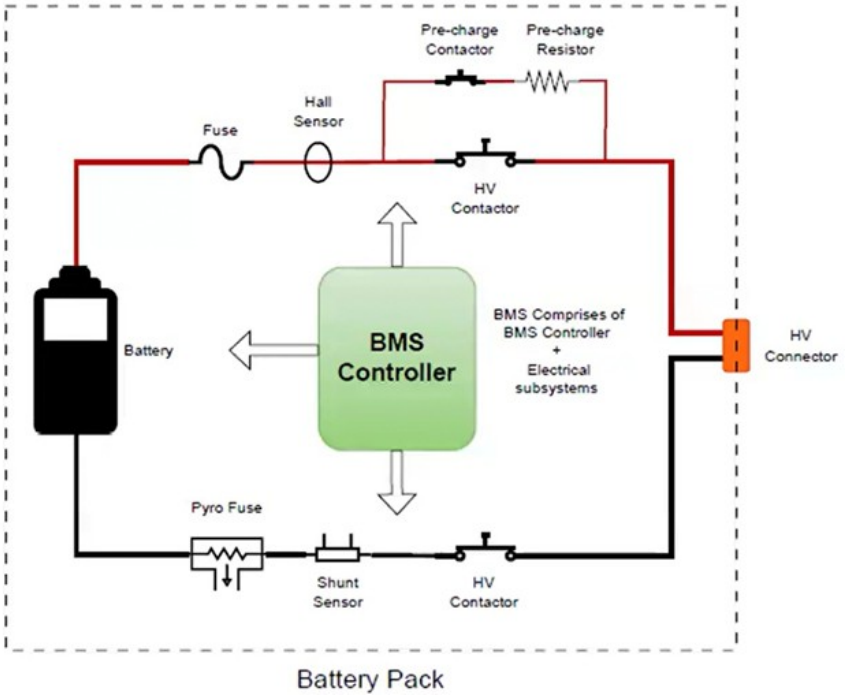

FIGURE 2.9: Generic Block Diagram of a BMS

2.4.2 Architecture of BMSs

BMS can be classified into two main categories based on the control method employed and the battery system voltage. As illustrated in Figure 2.10, the control method separates BMS into centralized and distributed, while the voltage classification separates BMS into low-voltage (typically under 60V) and high-voltage (typically above 60V) systems.

Centralized BMS architectures are mainly used in small-scale, low-voltage battery configurations, due to their simplicity and cost-effectiveness. In contrast, distributed BMS architectures are better suited to high-voltage or large-scale battery systems, where scalability, robustness and measurement accuracy are essential.

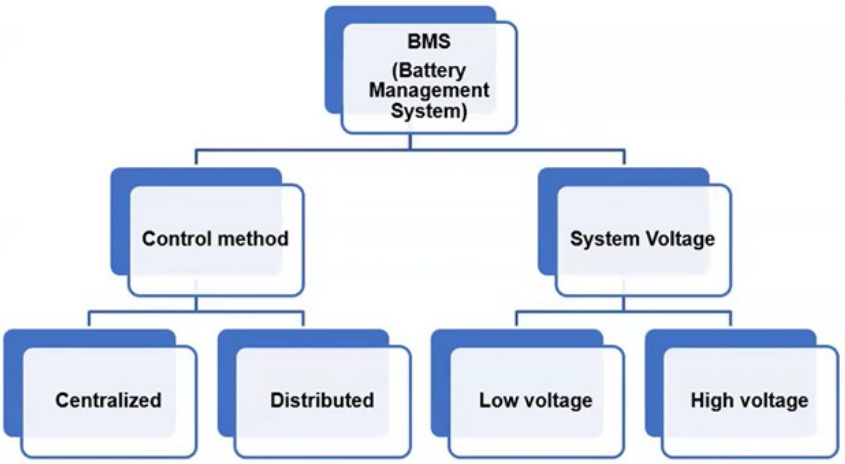

FIGURE 2.10: Classification of BMSs based on control method and system voltage.

2.4.2.1 Centralized BMS

In a centralized BMS architecture, a single control unit is responsible for monitoring and managing all the battery pack cells. This includes the measurement of voltages, temperatures, current, and the execution of balancing and protection strategies. As shown in Figure 2.11, centralized BMS architectures simplify data acquisition and integration but are generally suitable only for low-voltage systems due to wiring complexity and scalability limitations.

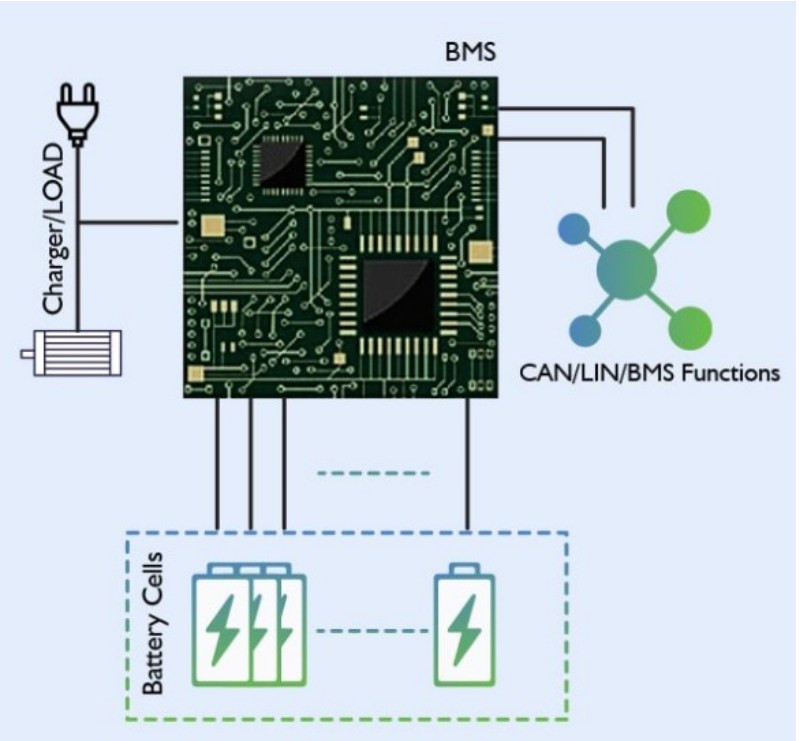

FIGURE 2.11: Centralized BMS Architecture: A single control unit interfaces with all cells.

This configuration is ideal for compact systems such as electric bicycles, scooters, and other low-power devices. However, as the number of cells increases, the extensive wiring required introduces signal degradation, complexity in PCB layout, and increased cost. The centralized unit must manage long wire runs to distant cells, which can result in voltage drops and measurement errors, particularly in high-voltage battery packs.

2.4.2.2 Distributed BMS

A distributed BMS consists of multiple controllers, typically a master-slave configuration, where each module has its own measurement unit. The master controller processes the data received from slave modules and computes key parameters such as SOC, SOH, voltage, and power. This setup is shown in Figure 2.12.

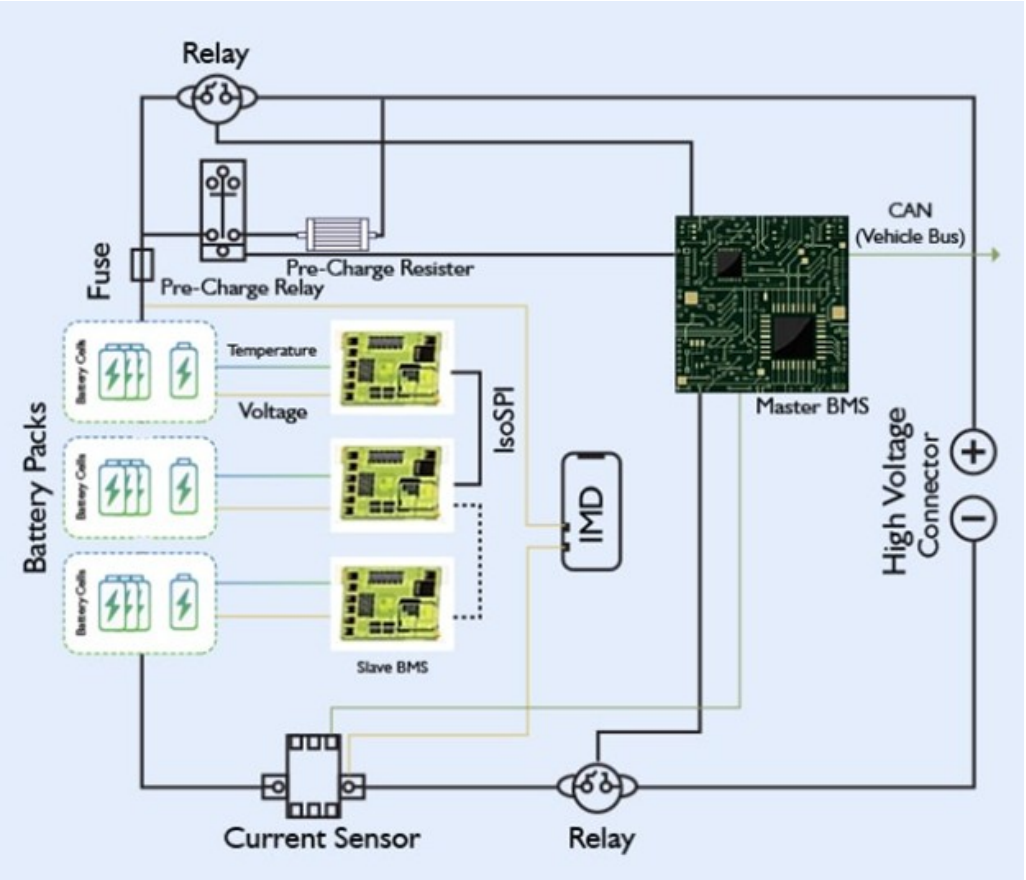

FIGURE 2.12: Distributed BMS Architecture: Multiple slave units communicate with a master BMS over a CAN network.

Distributed architectures are optimal for high-voltage applications such as electric vehicles and grid energy storage systems. By placing a local PCB near each cell module, wiring is minimized, digital communication is enhanced, and the system becomes more robust and scalable. CAN or UART networks are commonly used to transmit information from slave units to the master unit and to higher-level vehicle control units or cloud services.

2.4.2.3 Comparative Overview

A concise comparison of centralized and distributed BMS architectures is presented in Table 2.3, summarizing key attributes such as cost, scalability, complexity, and applications.

TABLE 2.3: Comparison of Centralized and Distributed BMS Architectures

Feature	**Centralized BMS**	**Distributed BMS**
Architecture	Single central unit monitors all cells	Multiple nodes manage subsets of cells
Scalability	Limited, difficult to scale for large systems	High, easily scalable for large systems
Complexity	Simpler design and integration	More complex due to multiple controllers
Cost	Lower initial cost	Higher due to added components
Wiring	Requires extensive wiring	Reduced wiring complexity
Applications	Ideal for small, low-voltage systems	Suitable for EVs and large energy storage

2.4.3 Design of the BMS

The design of a BMS relies on accurately measuring and processing critical battery parameters. This is achieved through the integration of two main components: the Analog Front End (AFE) and the Microcontroller Unit (MCU) [21]. Together, they form the core architecture of the BMS, enabling real-time monitoring, control, and communication across the system [23].

2.4.3.1 Analog Front End (AFE)

The AFE serves as the primary interface with the battery cells, responsible for capturing real-time analog data. The AFE is critical for monitoring essential parameters such as:

- **Cell Voltage**: Necessary for cell balancing, overvoltage/undervoltage protection, and accurate SOC estimation [24].
- **Cell/Module Temperature**: Vital for thermal management and ensuring the system remains within safe operational temperatures [25].
- **Pack Voltage and Insulation**: For some systems, this also includes monitoring the pack voltage and insulation resistance for system-level protection and diagnostics [23].

It is essential to select the AFE wisely, as some sensors are integrated directly into the AFE, reducing the need for separate components. For instance, voltage and temperature sensors are often integrated into the AFE, which simplifies the overall design and improves measurement accuracy. However, the AFE typically does not include current sensors, which are usually handled by external components such as *Hall effect sensors* or *shunt resistors* [26].

When selecting an AFE, the designer must consider the number of cells to be monitored, the required measurement accuracy, and the system's voltage and temperature monitoring needs. Integrated solutions like the bq76952 from Texas Instruments provide high-accuracy voltage and temperature measurement, but careful attention should be given to the system's overall sensor requirements to ensure optimal performance and reliability [27].

The AFE typically operates at the module level, managing groups of series-connected cells. This modular approach simplifies wiring and enhances scalability, but it also requires careful selection of components to ensure accurate measurements and proper isolation, particularly as the number of series-connected cells increases.

2.4.3.2 Microcontroller (MCU)

The **Microcontroller (MCU)** is the central processing unit of the BMS, responsible for controlling and coordinating the overall system. Its key functions include:

- **Data Acquisition**: Collecting digitized data from the AFE and preparing it for processing.
- **Control Logic**: Running algorithms for SOC and SOH estimation, thermal regulation, and fault detection [28].
- **Balancing Control**: Triggering either active or passive balancing circuits to ensure the cells are evenly charged, which prolongs battery life [29].
- **Communication**: Managing the flow of data between the BMS and external systems such as vehicle control units (VCUs), chargers, or cloud platforms, using communication protocols like CAN, UART, or SPI [30].
- **Diagnostics and Logging**: Storing historical data, fault logs, and operational parameters in memory, facilitating system evaluation and future updates [31].

- **Power Control**: The MCU is also responsible for managing the power-on and power-off control of the BMS, ensuring safe startup and shutdown sequences for the system.

2.4.3.3 Integration of AFE and MCU

In essence, the AFE focuses on accurate analog signal acquisition, while the MCU handles the digital processing and system-level coordination. The seamless interaction between the two ensures that the BMS can safely manage the battery pack, optimize performance, and extend its service life. This integration is essential for maintaining the system's reliability and efficiency, particularly in high-demand environments such as electric vehicles.

2.4.3.4 Sensing Technologies

To ensure the BMS functions accurately, various sensing technologies are employed for voltage, current, and temperature measurements. These include:

- **Voltage Sensing**: Typically achieved using resistance dividers and integrated voltage sensing chips, which offer high precision for monitoring individual cell voltages [32].
- **Current Measurement**: Achieved through Hall effect sensors (for galvanic isolation) and shunt resistors (for high-accuracy measurements), allowing precise monitoring of charge and discharge currents [33].
- **Temperature Monitoring**: Achieved using thermistors, thermocouples, and digital temperature sensors, which are critical for managing thermal conditions within the battery pack and preventing thermal runaway [34].

These sensing mechanisms ensure that the BMS can monitor all relevant parameters with high accuracy, contributing to the overall safety and efficiency of the battery system.

2.4.3.5 Power Management Considerations

Power management is a key consideration in BMS design, particularly for energy-efficient applications. The AFE and MCU should be selected not only based on accuracy but also considering their power consumption. Low-power components, including microcontrollers

with sleep modes, can significantly reduce overall system power consumption, enhancing the overall efficiency of the BMS. This is particularly important in battery-powered systems like electric vehicles, where reducing power consumption can directly extend operational range.

Battery Equalization Techniques, which help optimize energy usage, are an important part of power management. These techniques can either be energy dissipative (passive balancing) or energy non-dissipative (active balancing) [35].

- **Energy Non-Dissipative (Active Balancing)**: These methods, such as the use of *Forward-Flyback Converters* and *Shared Converters*, enable the transfer of energy between cells to balance their voltage levels without dissipating excess energy as heat [36]. These methods are more efficient but tend to be more complex and costly.
- **Energy Dissipative (Passive Balancing)**: This simpler method uses resistive circuits to dissipate excess energy from higher-voltage cells, resulting in slower equalization but lower cost and simplicity [37].

By ensuring proper balancing of cell voltages, these techniques help reduce energy loss and improve the efficiency and lifespan of the battery pack. Thus, effective equalization can significantly enhance overall power management in BMS design.

Additionally, precharge control is essential for managing the inrush current when the system is powered on. The precharge circuit helps limit the current flowing into the battery pack during initial power-up, protecting the cells and other components from sudden surges. This is particularly important in high-voltage systems to avoid damage to sensitive electronics [38].

2.4.3.6 Safety and Fault Tolerance

The design of a BMS must incorporate safety mechanisms to protect both the battery and the system in the event of faults. These mechanisms include overcurrent protection, overvoltage protection, thermal management, and the use of pyrofuses [39]. A pyrofuse is a critical component for battery safety, providing an added layer of protection by disconnecting the circuit in the event of a short-circuit or thermal fault, ensuring the system remains safe.

2.4.3.7 Real-Time Requirements

Given the safety-critical nature of BMS systems, real-time data processing is crucial. The MCU must be capable of performing quick calculations for SOC and SOH estimation, fault detection, and thermal regulation to ensure the safe operation of the battery pack at all times. The BMS must provide timely feedback to other components, such as vehicle control units (VCUs), to ensure coordinated control of the battery system.

Chapter 3

Objectives

3.1 General Objectives

The objective of this thesis is to develop the theoretical, modelling, and hardware foundations of a complete BMS for a 60 V lithium-ion battery pack used in electric scooter applications. This includes the development of an accurate real-time battery model, the design of robust SOC and SOH estimation methods, and the implementation of a custom BMS hardware platform. The outcomes of this first part establish a validated modelling framework and a ready-to-integrate embedded hardware architecture that will support future firmware deployment and full experimental validation.

3.2 Specific Objectives

1. To model a lithium-ion battery cell using a Dual Polarization (2RC) equivalent circuit formulated in the Laplace domain, enabling stable and computationally efficient real-time simulation.

2. To identify battery parameters using OCV–SOC and Hybrid Pulse Power Characterization (HPPC) test data, and to implement SOC-dependent lookup tables capturing nonlinear cell behaviour.

3. To develop and validate an SOC estimation algorithm based on advanced Coulomb Counting with OCV-based drift correction, and evaluate its performance under dynamic load conditions in MATLAB/Simulink.

4. To study SOH estimation principles and define a methodology based on measurable indicators such as capacity fade and internal resistance for future embedded implementation.

5. To design a centralized BMS hardware architecture incorporating the BQ76952 analog front end, STM32H563 microcontroller, current and temperature sensing circuits, power management, protection MOSFETs, and a compact two-layer PCB suited for e-scooter integration.

6. To prepare the hardware platform for future embedded deployment, including interfaces for CAN and SPI communication, and a modular firmware structure to host real-time estimation algorithms.

7. To establish a complete system foundation that enables, in future work, the development of full BMS firmware, hardware prototyping, and experimental validation on a physical electric-scooter battery system.

Chapter 4

Methodology

This chapter presents the methodology adopted for developing the modeling, estimation, and hardware foundations of the BMS designed for a 60 V lithium-ion battery pack in an electric scooter application. The work follows a structured model-based engineering workflow combining analytical modeling, numerical simulation, hardware-oriented design, and system integration. The objective is to create a coherent foundation for future embedded implementation and experimental validation.

4.1 Research Design and Approach

The methodology adopted in this thesis follows a model-based design (MBD) workflow, integrating battery modeling, algorithm development, hardware architecture design, and simulation-driven validation. The process begins with analytical modeling of the battery system, where a computationally efficient yet physically meaningful representation is developed to support state estimation. This model is then used to design and validate SOC estimation algorithms prior to any embedded implementation. The workflow further extends to hardware development, where the BMS architecture is designed around safety, sensing accuracy, and microcontroller integration. All of these elements are verified through incremental simulation and design reviews to ensure compatibility and future expandability.

4.2 Battery Modeling Methodology

Accurate battery modeling is essential for SOC estimation and for predicting voltage behavior under dynamic loads. Based on the analysis of modeling strategies in Chapter 2, Equivalent Circuit Models (ECMs) were selected for this work due to their computational efficiency and suitability for embedded BMS execution.

Figure 4.1 summarizes the trade-offs between Equivalent Circuit Models, Electrochemical Models, and Multiphysics Models in terms of complexity, modeling accuracy, and computational cost. As illustrated, ECMs provide the optimal balance for embedded BMS applications, combining sufficient physical fidelity with low computational requirements.

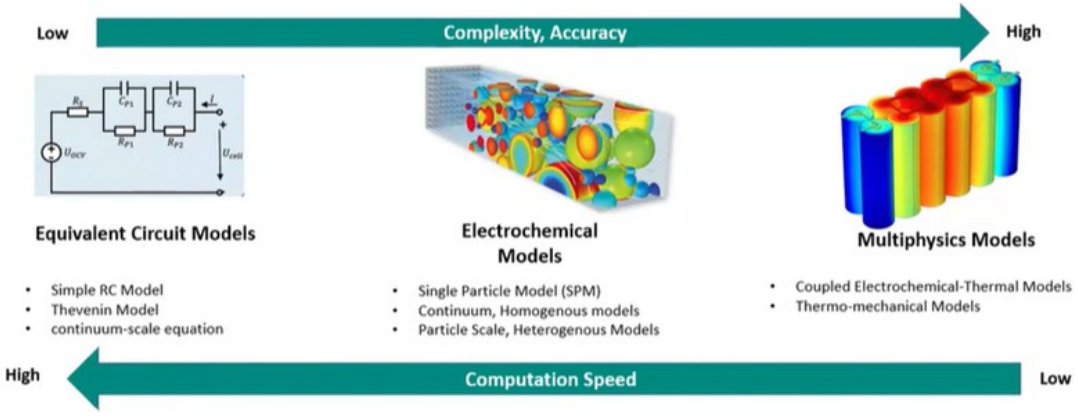

FIGURE 4.1: Comparison of battery modeling techniques in terms of complexity, accuracy, and computational speed.

A Dual Polarization (2RC) model was therefore implemented, consisting of an open-circuit voltage (OCV) source, a series ohmic resistance, and two RC networks capturing fast and slow polarization effects. To improve numerical stability, the model was expressed using transfer functions in the Laplace domain, rather than time-domain differential equations. This formulation avoids numerical drift and is well adapted to digital control implementations.

SOC-dependent lookup tables were generated to map internal resistance, polarization resistances, and time constants as functions of SOC. This ensures that the model dynamically reflects nonlinear battery behavior, particularly during low-SOC and high-SOC conditions. The model was validated in MATLAB/Simulink using pulse-current tests that reproduced expected transient and relaxation dynamics.

4.3 SOC Estimation Framework

The SOC estimation methodology is based on Advanced Coulomb Counting combined with OCV-based correction. Coulomb Counting provides the core mechanism, integrating current over time while applying saturation limits. To correct long-term drift, the algorithm incorporates an OCV–SOC lookup table during rest periods, detected through thresholds on current magnitude and voltage slope. This hybrid approach maintains estimation accuracy without requiring the computational complexity of Kalman filtering. A complete Simulink implementation was constructed to evaluate estimator performance under variable current pulses and to ensure proper integration with the validated 2RC model.

4.4 Hardware Development Methodology

The hardware development methodology focuses on designing a robust, compact, and feature-complete BMS architecture suitable for electric scooter applications. The process began with defining electrical, safety, and sensing requirements, followed by selecting components that meet thermal, noise, protection, and computational constraints.

The analog front-end (AFE) design centers on the Texas Instruments BQ76952, chosen for its integrated protection features, passive balancing capability, and compatibility with embedded microcontroller interfaces. Each cell input is conditioned using a 20 Ω input resistor and a 100 nF filtering capacitor to ensure measurement stability. Current sensing is performed through a precision shunt resistor connected to the SRP and SRN pins, while temperature sensing is implemented using NTC thermistors connected through dedicated low-pass filter networks.

The microcontroller subsystem is built around the STM32H563RIT6, selected for its processing performance, native CAN communication, and extensive peripheral support. The MCU is clocked through a 24 MHz crystal for core timing and a 32.768 kHz crystal for RTC functionality. Vehicle-grade CAN communication is ensured by integrating the TJA1042T CAN transceiver, configured with appropriate ESD protection, decoupling, and termination components.

Protection circuitry is implemented using MOSFET-based switching for charge and discharge paths, arranged in a back-to-back configuration to allow bidirectional control. A pre-charge circuit is included to limit inrush currents when energizing capacitive loads.

Transient voltage suppressors, reverse-polarity protection elements, and a secondary resettable fuse enhance the fault tolerance and overall robustness of the system. The power stage is supplied through an LMR51430 buck converter producing a stable 3.3 V rail, complemented by a precision voltage reference regulator to support critical analog measurements.

4.5 PCB Layout Methodology

The PCB layout was designed using Autodesk Eagle with a 100 mm × 80 mm two-layer board, balancing manufacturability and performance. Special attention was given to separating high-current paths, analog sensing traces, and digital communication lines. Copper pours were used for PACK and BAT rails to reduce impedance, while Kelvin routing ensured accuracy in shunt current measurements. Thermal considerations informed the placement of MOSFETs, power components, and via stitching patterns. Decoupling capacitors were positioned as close as possible to IC power pins, and ground return paths were optimized to minimize noise coupling, particularly around the AFE and MCU.

4.6 Methodological Considerations

The methodological choices throughout this thesis were consistently guided by real-time viability, accuracy of state estimation, scalability to larger battery systems, and robustness in embedded environments. The integrated approach, combining modeling, estimation development, hardware design, and simulation, ensures that the resulting BMS architecture is well-prepared for future firmware development and hardware validation phases.

Chapter 5

Battery Modeling for BMS Integration

This chapter presents the methodology for battery modeling that will serve as the foundation for subsequent development and integration of advanced BMS functionalities. The modeling approach will focus on accurately capturing the electrical and dynamic characteristics of lithium-ion cells using equivalent circuit representations suitable for real-time embedded systems. The implemented models will support the development of SOC estimation algorithms and will be validated through simulation and parameter identification procedures. This modeling work will enable future experimental testing, hardware-in-the-loop validation, and deployment of robust energy management strategies in embedded platforms.

5.1 Equivalent Circuit Modeling Approach

Batteries are inherently unstable systems, exhibiting nonlinear and time-dependent behavior rather than a stable, static output. When subjected to charge or discharge currents, the terminal voltage responds with immediate transients and gradual relaxations due to complex internal electrochemical processes. Simple models often fail to represent these dynamics accurately, particularly under variable real-world operating conditions.

As discussed in Section 2.3, several modeling techniques can be used to represent lithium-ion battery behavior, each offering varying levels of complexity and accuracy. For embedded

BMS applications, Equivalent Circuit Models (ECMs) are particularly promising due to their balance between computational efficiency and modeling fidelity.

However, even within the ECM family, selecting the most suitable model structure requires careful consideration. The configuration must be able to capture the dynamic behavior of the battery while remaining lightweight enough for real-time implementation on microcontrollers. This selection process is guided by a thorough analysis of the literature to identify the model that best aligns with the performance, stability, and efficiency requirements of our application.

To address these challenges, the selected model must balance fidelity, accurately capturing the battery's transient and steady-state responses, with simplicity, to enable robust and efficient implementation in real-time embedded systems. In the following sections, we analyze several ECM configurations commonly cited in the literature and evaluate their ability to meet these demands, with the goal of identifying the most appropriate model for our application.

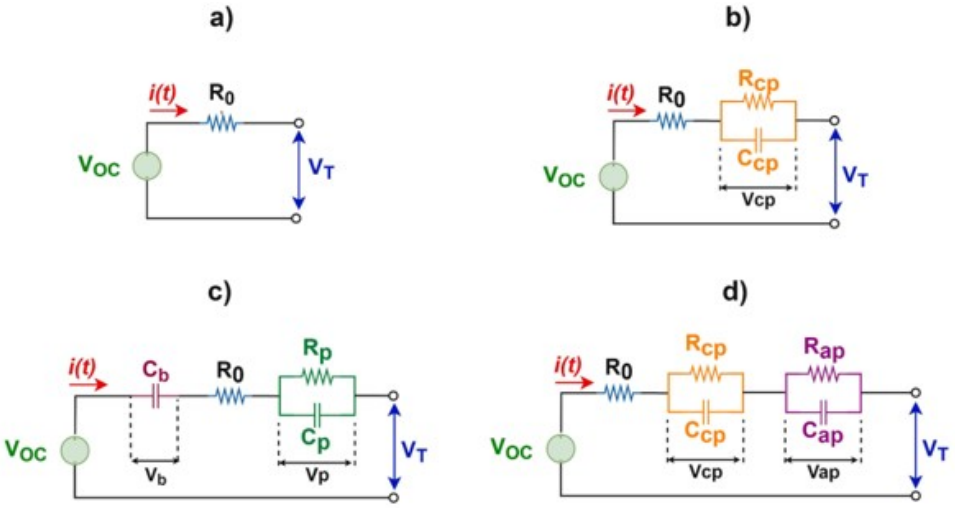

FIGURE 5.1: Common Equivalent Circuit Models: (a) Rint model, (b) Thevenin (1RC) model, (c) PNGV model, (d) Dual Polarization (2RC) model.

Figure 5.1 presents the most commonly used ECM configurations in the literature. Each model exhibits a different level of complexity and fidelity in representing battery dynamics. The following sections examine their limitations and advantages in detail, with the goal of determining the most suitable model for our application based on literature evidence and practical constraints.

5.1.1 Limitations of Simplified ECM Approaches

- **Rint Model:** Early equivalent-circuit models treat the battery almost like a static source with internal resistance (the so-called `Rint` model). The `Rint` model tracks SOC by coulomb counting and uses an OCV vs SOC relationship, but it ignores dynamic polarization effects, meaning it cannot reproduce the voltage drop and recovery that real batteries show during pulses. As a result, `Rint` can be fairly accurate only for steady, low-demand use and over short periods; under dynamic loads its voltage error grows significantly [40]. In one study, the `Rint` and simple RC models had large voltage errors during aggressive load changes, indicating they lack key dynamics and "need much improvement" [40].

- **1RC Thevenin Model:** The next step up is the one-RC Thevenin model (sometimes just called an "RC model" or first-order RC model). This adds a single resistor-capacitor pair to mimic battery transient response (one time constant). The 1RC model indeed improves dynamic performance; for example, it can follow the voltage during pulses with smaller error (often under ∼1% deviation) [40]. However, a single RC branch captures only one relaxation time. Real lithium-ion batteries have multiple relaxation processes (fast surface charge equilibration and slower diffusion processes), so a 1RC model may still miss some long-term drift or short-term spikes. It also doesn't inherently handle voltage hysteresis (the difference in OCV between charge and discharge for the same SOC) unless augmented. Researchers have noted that while a one-RC model is almost as good as more complex models in some cases, more demanding applications reveal its limitations [40]. For instance, a 1RC model might struggle with accuracy over a wide range of SOC and dynamic regimes, or its error spikes under rapid changes.

- **PNGV Model:** Another enhanced variant is the PNGV model (from the Partnership for a New Generation of Vehicles), which adds a bulk capacitance in series with a 1RC network to represent the battery's charge storage capability and slower OCV changes. The intent is to account for the OCV variation due to accumulated charge withdrawal (sometimes called the charge depletion or "capacitive" effect) beyond the immediate RC transient [40]. However, studies show mixed results for the PNGV model: the added capacitance can introduce unstable voltage estimates or numerical oscillations if not tuned well. In one comparison, the PNGV model actually worsened the voltage prediction error (producing noticeable fluctuations), and its average error was higher than the simpler 1RC Thevenin model in dynamic tests [40]. While the PNGV did slightly reduce the peak error in some cases (by preventing

extreme voltage deviations through the capacitive buffer), it did not yield the overall accuracy expected. This outcome underlines that adding components arbitrarily can complicate the model without guaranteed benefit – model structure matters.

Models with insufficient dynamics (like `Rint` or even 1RC in some scenarios) cannot reliably capture the "unstable" characteristics of a battery's voltage response. On the other hand, adding complexity beyond a certain point (e.g. the bulk capacitor in PNGV or additional RCs without clear physical correspondence) may introduce diminishing returns or even new errors. There is a trade-off between simplicity and fidelity: *"Generally, the simpler the model, the faster it will simulate, but the lower its fidelity"* [40]. We seek a sweet spot on this trade-off curve for our application.

5.1.2 Battery Model Selection for Effective BMS Deployment

To capture the battery's dynamic behavior involving multiple time constants without resorting to full electrochemical models, the Thevenin equivalent circuit with two RC pairs, also known as the Dual Polarization (DP) model, is widely accepted, particularly in automotive applications. It achieves over 95% accuracy for SOC estimation and at least 85% accuracy for SOC estimation, which is sufficient given the slow degradation dynamics. This model simplifies algorithm development, reduces the number of parameters requiring calibration, and aligns well with the resource constraints of embedded systems, such as limited memory and processing time. More complex Thevenin models, such as the 3RC configuration, are typically reserved for high-precision applications like biomedical systems or research settings where 99% accuracy is essential. The 2RC model consists of an ideal voltage source, a series resistance, and two resistor-capacitor (RC) networks, each representing a distinct physical phenomenon within the battery cell. Resistors model energy dissipation (power loss), while capacitors capture voltage dynamics and storage behavior. Since BMS typically operates at the module or pack level rather than the individual cell level, such lumped models are both practical and effective for real-time estimation and control tasks [41].

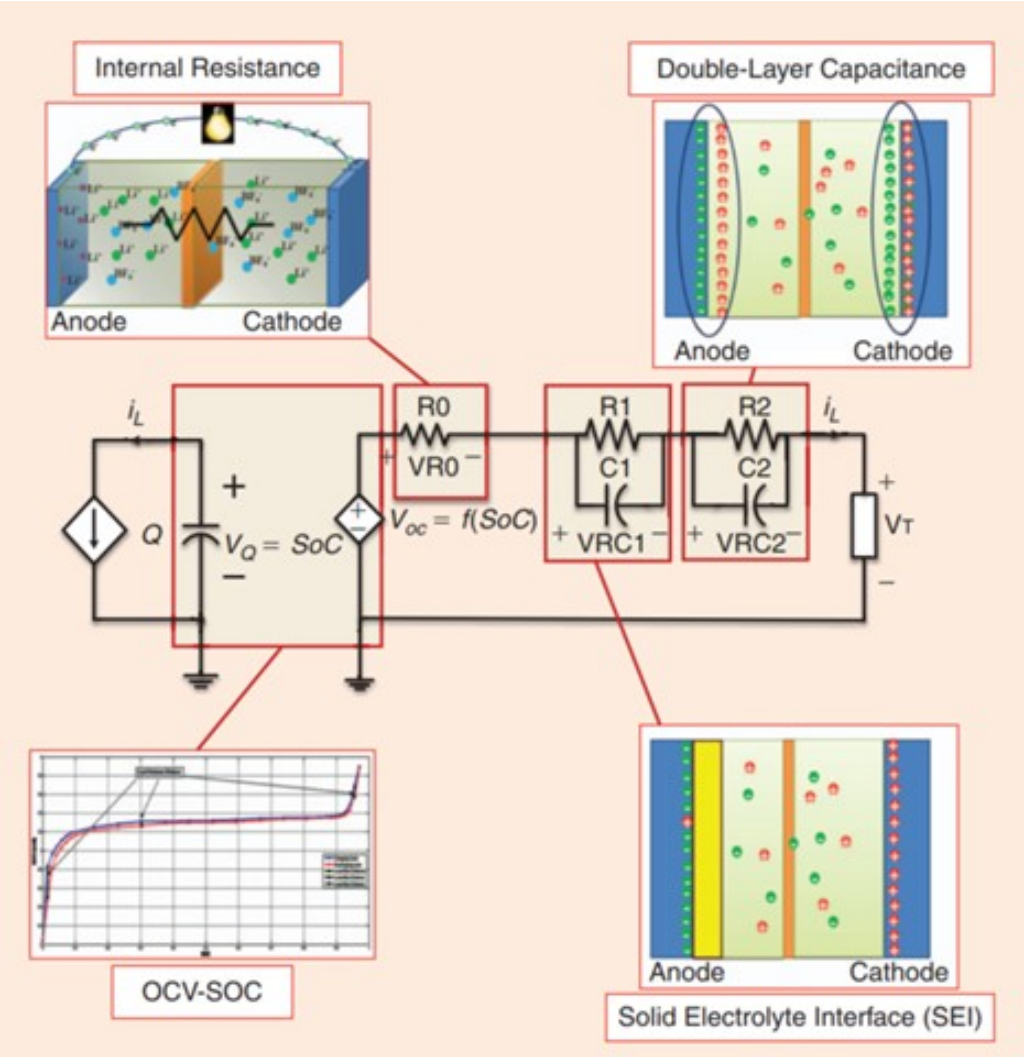

FIGURE 5.2: Physical Interpretation of Equivalent Circuit Elements in the 2RC Model

The components of a 2RC model typically include:

- **Open-Circuit Voltage source (Voc(SOC))**: Represents the battery's equilibrium voltage based on SOC. It includes minor hysteresis and SOC-dependent effects.
- **Series Resistance (R0)**: Captures the immediate IR voltage drop during current flow. . Higher resistance leads to greater energy losses and decreased efficiency during charge/discharge cycles.
- **First RC Pair (R1–C1)**: Models short-term relaxation due to the Solid Electrolyte Interphase (SEI) layer at the anode, including ion migration and transport. These components influence the battery's response time and rate capability.

- **Second RC Pair (R2–C2)**: Represents long-term diffusion polarization, mainly at the double-layer interfaces, such as concentration polarization and charge transfer resistance. These components affect the battery's voltage response and efficiency.

This two-RC architecture enables simulation of fast and slow transient responses, such as voltage drops, rebound, and drift [41].

The detailed physical origin of each component is illustrated in Figure 5.2, which links the resistor and capacitor elements of the 2RC model to actual electrochemical processes. The SEI layer, responsible for fast relaxation, is represented by R_1 and C_1, while the double-layer capacitance contributes to the slower diffusion response modeled by R_2 and C_2. The series resistance R_0 reflects internal ohmic losses, and $V_{OC}(SOC)$ is derived from SOC-OCV characterization curves.

- **Accuracy Benefits:** The 2RC model has consistently shown low voltage error in validation tests. For example, under aggressive dynamic stress profiles, its maximum voltage error was only 0.22 V, significantly better than Rint and 1RC models [41].
- **Optimal Complexity:** Adding more than two RC pairs yields minimal improvement. Studies confirm two RC branches strike the best balance between complexity and accuracy [40].
- **Real-Time and Practicality:** The model is computationally efficient. While electrochemical models are numerically intensive, 2RC models run in real time and can be calibrated to mimic complex dynamics at a fraction of the cost [42].
- **Adaptive and Robust:** Parameters such as R_0, R_1, R_2, C_1, and C_2 can adapt to SOC, temperature, and aging, making the model flexible across operating conditions [42].
- **Scalability to Packs:** Since cells of the same chemistry behave similarly, a single 2RC model can represent multiple cells or modules, simplifying BMS implementation [40].

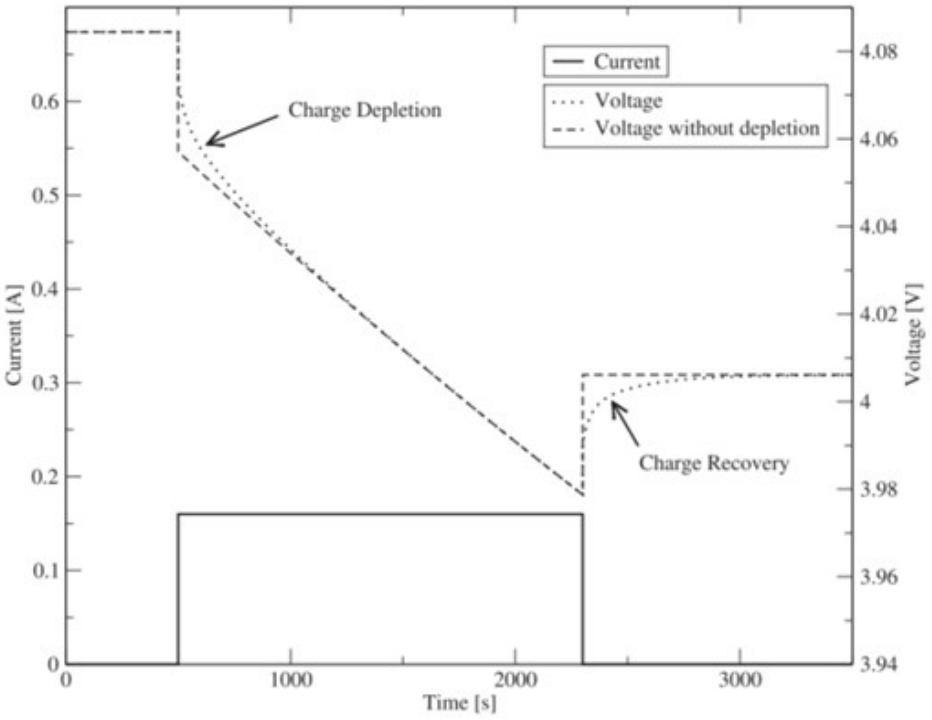

Fig. C.2. Charge depletion and recovery.

FIGURE 5.3: Illustration of Charge Depletion and Recovery in Battery Voltage Response

As illustrated in Figure 5.3, the battery voltage exhibits an initial drop when a load is applied, followed by a gradual recovery once the load is removed. This behavior results from the interaction between fast-responding surface charge effects and slower diffusion-driven processes. The 2RC model captures these dual transients accurately, unlike simpler models that cannot represent the curved recovery profile.

Ultimately, the 2RC model provides the optimal balance between modeling fidelity and implementation complexity, making it well-suited for our application. Therefore, it is selected as the preferred model for this work. The following sections detail its implementation within an embedded BMS framework.

5.2 Battery Modeling Implementation

To implement the selected 2RC Thevenin model, two main approaches can be used to represent the dynamics of the circuit: the time domain and the Laplace domain.

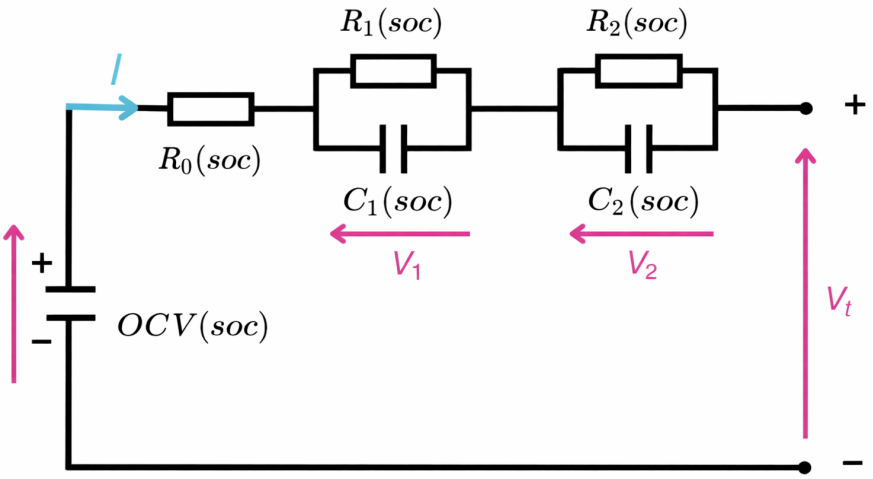

FIGURE 5.4: Dual Polarization (2RC) Equivalent Circuit Model for Lithium-Ion Battery

5.2.1 Time Domain Implementation

In the time domain, the battery terminal voltage V_t is computed by analyzing the current flow through each branch of the 2RC circuit illustrated in Figure 5.4. The voltages V_1 and V_2 across the capacitors C_1 and C_2, respectively, evolve dynamically in response to charging and discharging events and contribute to the overall terminal voltage behavior.

$$V_t = OCV - V_0 - V_1 - V_2 \tag{5.1}$$

Expanded:

$$V_t = OCV - i \cdot R_0 - ((i - i_1) \cdot R_1) - ((i - i_2) \cdot R_2) \tag{5.2}$$

Expressing capacitor dynamics using differential equations:

$$V_t = OCV - i \cdot R_0 - \left((i - C_1 \frac{dV_1}{dt}) \cdot R_1\right) - \left((i - C_2 \frac{dV_2}{dt}) \cdot R_2\right) \tag{5.3}$$

5.2.1.1 Limitations of Time Domain Implementation:

- **Noise Amplification:** Differentiation amplifies high-frequency noise in current and voltage signals.
- **Numerical Instability:** Discretized differential equations may exhibit unstable behavior under finite precision and low sampling rates.
- **Difficult Calibration:** Tuning derivative-based models often requires additional filtering, increasing system complexity.
- **Hardware Sensitivity:** Real-time execution suffers on resource-limited microcontrollers due to sensitivity to sampling rate and Analog-to-Digital Converter (ADC) resolution.

5.2.2 Laplace Domain Implementation

To overcome the challenges of the time domain formulation, the Laplace domain approach models the same 2RC structure from Figure 5.4 using first-order transfer functions in the Laplace domain. In this formulation, the dynamic behavior of V_1 and V_2 is represented using rational expressions in the Laplace variable s, which facilitates more stable and noise-resilient computation.

The terminal voltage expression in the Laplace domain becomes:

$$V_t = OCV - i(s) \cdot \left(R_0 + \frac{R_1}{1 + sR_1C_1} + \frac{R_2}{1 + sR_2C_2} \right) \tag{5.4}$$

Alternatively, using impedance notation:

$$V_t = OCV - i \cdot (R_0 + Z_1 + Z_2) \tag{5.5}$$

In the Laplace domain:

- Resistors remain unchanged as they are non-reactive.
- Capacitor impedance is expressed as $Z_C = \frac{1}{sC}$.

To transform the time-domain RC network to the s-domain (Laplace domain), we model the RC impedance with feedback using a control representation. The transfer function of a closed-loop system is:

$$T(s) = \frac{O(s)}{I(s)} = \frac{G(s)}{1 + G(s)H(s)} \tag{5.6}$$

Now, to derive the transfer function of an RC branch such as $Z_1 = R_1 \parallel C_1$, we apply control theory principles. The closed-loop transfer function is given by:

$$R_{eq} = \frac{R_1 \cdot \frac{1}{C_1 s}}{R_1 + \frac{1}{C_1 s}} = \frac{R_1}{1 + R_1 C_1 s} \tag{5.7}$$

Therefore:

$$G(s) = \frac{1}{R_1 C_1 s}, \quad H(s) = 1 \tag{5.8}$$

5.2.2.1 Advantages of Laplace Domain Implementation:

- **Numerical Stability:** Transfer functions avoid explicit differentiation, reducing susceptibility to noise and improving solver convergence.
- **Noise Immunity:** Filters and transfer functions suppress sensor noise more effectively than raw derivatives.
- **Laplace-Domain Analysis:** Allows the use of Bode plots and system identification tools for tuning and analysis.
- **Simplified Control Design:** Facilitates gain/phase margin analysis, essential for closed-loop BMS estimation and control.
- **Embedded Compatibility:** Enables efficient real-time simulation using discrete transfer function blocks, making it ideal for STM32-based systems.

The Laplace domain model is then selected for BMS implementation due to its robustness, simplicity in control design, and better suitability for real-time embedded applications.

5.3 Model Parameter Identification

To accurately implement the 2RC equivalent circuit model, the parameters, including the open-circuit voltage (OCV) curve, the ohmic resistance R_0, and the polarization branch parameters (R_1, C_1) and (R_2, C_2), must be identified from experimental data. In this work, parameter identification is structured around two complementary test procedures: (i) an OCV–SOC characterization, which provides the static voltage map required by the model and SOC correction, and (ii) a Hybrid Pulse Power Characterization (HPPC) test, which captures the dynamic voltage response needed to extract the RC parameters. Although presented separately for clarity, both tests rely on the same pulse–rest excitation principle and are derived from the same underlying measurement data.

5.3.1 Open-Circuit Voltage vs. State of Charge (OCV–SOC) Test

The objective of the OCV–SOC test is to determine the open-circuit voltage as a function of the state of charge, which is later used as a lookup table in the battery model and in SOC estimation algorithms. The test procedure is illustrated in Figure 5.5a, where the cell is first fully charged, then subjected to a sequence of controlled discharge pulses. After each pulse, the current is set to zero and the cell is allowed to rest until the terminal voltage stabilizes.

The stabilized voltage measured during each rest interval is considered an approximation of the OCV corresponding to that SOC level. Since each pulse removes a known quantity of charge, the SOC reduction is computed by integrating the current over time using Coulomb counting. By repeating this process with a constant SOC step size (e.g., approximately 5% per step), the full OCV–SOC characteristic shown in Figure 5.5b is obtained. When the same procedure is performed at different temperatures, the result can be extended to a two-dimensional lookup table $OCV(SOC, T)$.

It is important to note that Figure 5.5b not only provides the static OCV–SOC relationship, but also contains the transient voltage behavior during each pulse. By zooming into an individual pulse–rest segment of this figure, the dynamic voltage responses analyzed in the HPPC test are obtained.

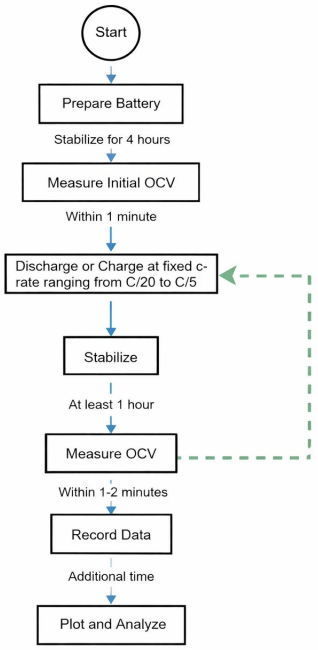

(A) OCV–SOC test procedure flowchart

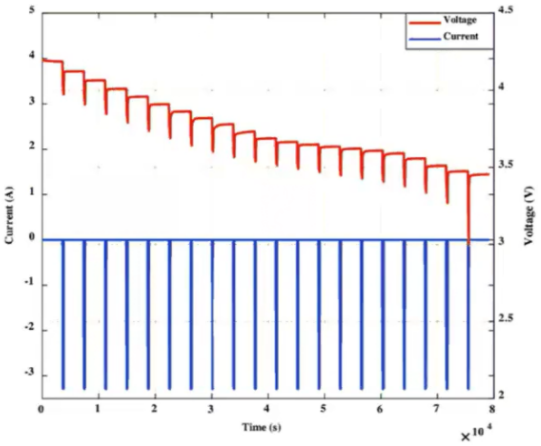

(B) OCV–SOC characteristic obtained from pulse–rest discharge

FIGURE 5.5: Open-Circuit Voltage (OCV) versus State of Charge (SOC) test: procedure and resulting characteristic

5.3.2 Hybrid Pulse Power Characterization (HPPC) Test

The HPPC test focuses on extracting the dynamic parameters of the battery by analyzing its voltage response to short current pulses. The overall HPPC procedure is summarized in Figure 5.6a, where current pulses are applied at predefined SOC levels, followed by rest periods during which voltage relaxation is observed.

The voltage and current waveforms during a single pulse event are shown in Figure 5.6b, which corresponds to a zoomed-in view of one pulse segment from the OCV–SOC test data in Figure 5.5b. The immediate voltage drop at the onset of the pulse reflects the ohmic contribution of the cell and is used to estimate the series resistance R_0 through the relation $\Delta v_0 \approx I R_0$.

Following the pulse, the voltage relaxation behavior during the rest phase is illustrated in Figure 5.6c. This slower, exponential recovery captures the polarization effects associated with the RC branches of the equivalent circuit. By fitting first- and second-order RC dynamics to this relaxation curve, the parameters (R_1, C_1) and (R_2, C_2) are identified. Because this analysis must be repeated across multiple SOC levels (and potentially different

temperatures), the parameter extraction process is typically automated using MATLAB scripts or Simulink-based estimation tools.

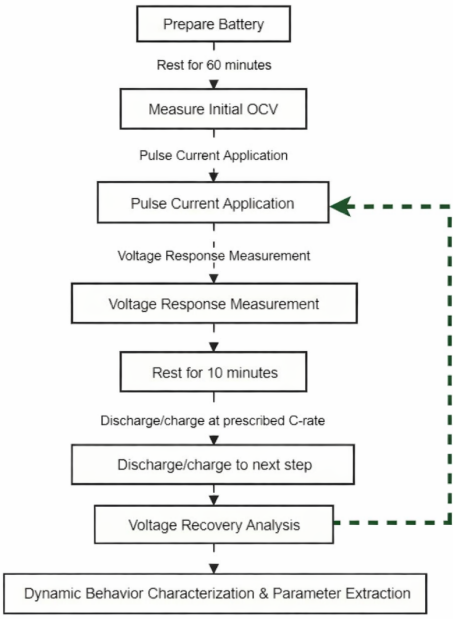

(A) HPPC test procedure

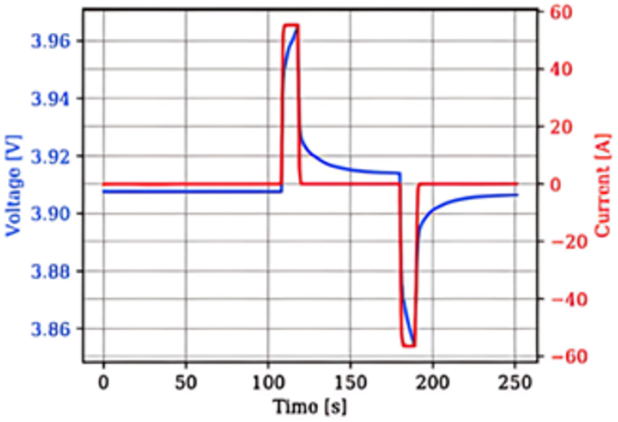

(B) Voltage and current response during HPPC pulse

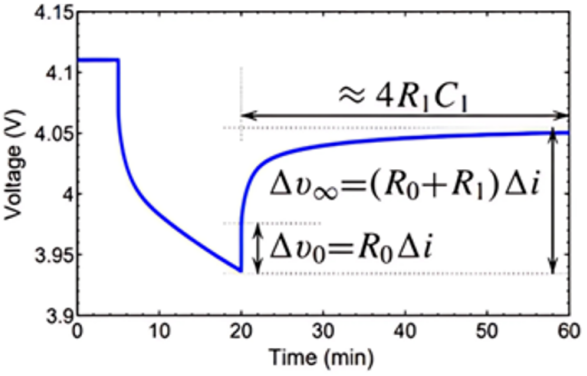

(C) Voltage relaxation and polarization behavior for RC parameter extraction

FIGURE 5.6: Hybrid Pulse Power Characterization (HPPC) test and parameter extraction methodology

By combining the static OCV–SOC map obtained from Figure 5.5b with the dynamic parameters extracted from the HPPC analysis in Figures 5.6b and 5.6c, the 2RC equivalent circuit model is fully parameterized. This unified approach ensures consistency between static and dynamic characterization and provides a solid foundation for accurate battery simulation and embedded SOC estimation.

5.3.3 Extracted Parameters and Applications

- **Series Resistance (R_0):** The instantaneous voltage drop upon applying a current pulse is used to calculate the ohmic resistance of the battery, which includes contact and electrolyte resistance.
- **RC Time Constants (R_1C_1, R_2C_2):** The post-pulse exponential decay is fitted using nonlinear regression or curve fitting techniques to identify the values of resistances and capacitances that describe fast and slow dynamics in the 2RC model.

While this chapter focused on establishing a foundation for the 2RC model using empirical pulse testing, more advanced techniques are planned for future work to enhance the robustness and adaptability of the battery model. These future steps will include:

- **Extended Kalman Filter (EKF)-Based Parameter Estimation:** To enable real-time tracking of battery state and parameter evolution, EKF techniques will be applied for adaptive model calibration.
- **Signal Processing and Data Conditioning:** Further processing of HPPC data, such as segmentation by SOC and filtering of measurement noise, will support more accurate and consistent parameter estimation.

The RC-based modeling approach remains a practical and effective method for lithium-ion battery characterization. Its ability to represent dynamic behavior such as impedance spectra and transient response makes it suitable for applications demanding real-time response, including electric vehicle energy systems. Furthermore, the simplicity of the RC structure, combined with widespread toolchain support in simulation environments, enhances its integration into embedded BMS platforms. This balance of accuracy, computational efficiency, and interpretability solidifies the RC model's status as a preferred framework for battery modeling and parameter extraction.

5.3.4 Parameter Variation Using Lookup Tables

To accurately capture the nonlinear behavior of lithium-ion batteries, the parameters of the 2RC equivalent circuit model are implemented as state-dependent quantities rather than fixed constants. In particular, the open-circuit voltage OCV, the ohmic resistance R_0, and

the polarization parameters (R_1, C_1) and (R_2, C_2) are modeled as explicit functions of the state of charge (SOC) using lookup tables within the MATLAB/Simulink environment.

The numerical values used to populate these lookup tables are obtained from experimentally performed battery characterization tests, namely the Open-Circuit Voltage versus State of Charge (OCV–SOC) test described in Section 5.3.1 and the Hybrid Pulse Power Characterization (HPPC) test presented in Section 5.3.2. Since these parameters are directly extracted from controlled laboratory measurements, they represent physically meaningful and robust characteristics of the battery cell over its operating SOC range. For completeness and reproducibility, the numerical lookup table data used in this work are provided in Appendix A.

To implement this model, a custom block diagram was developed in MATLAB/Simulink. A logical SOC value of 80% was chosen for initialization. Figure 5.7 shows the developed simulation structure based on the Laplace-domain 2RC Thevenin model.

5.3.4.1 Lookup Table Implementation and Numerical Handling

The model parameters are discretized at fixed SOC breakpoints and implemented as one-dimensional lookup tables indexed by SOC. During simulation, the instantaneous SOC value continuously addresses these tables, enabling real-time adaptation of the model parameters to the battery operating point. Linear interpolation between adjacent SOC nodes is applied to compute intermediate values. This interpolation method was selected due to its numerical stability, low computational complexity, and suitability for real-time embedded implementation. Given the smooth and monotonic variation of OCV, R_0, R_1, R_2, C_1, and C_2 with SOC, linear interpolation provides sufficient accuracy without introducing oscillations or overfitting effects.

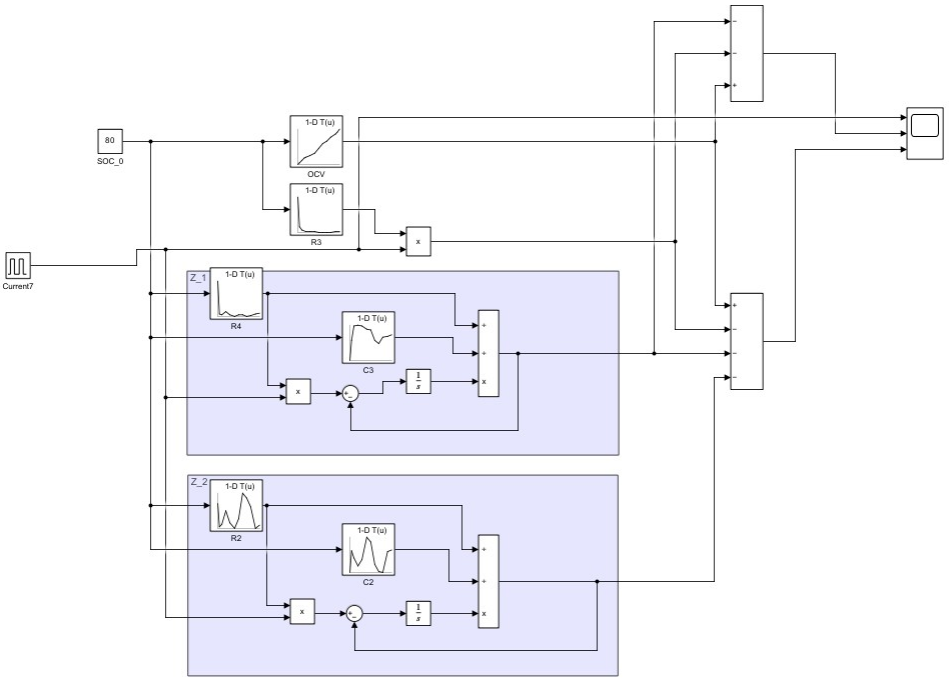

FIGURE 5.7: Simulink implementation of the 2RC model

Extrapolation outside the defined SOC range is intentionally avoided. Instead, parameter values are saturated at the minimum and maximum SOC boundaries to prevent unphysical behavior at extreme operating conditions. All parameters are handled using double-precision floating-point representation during simulation. For embedded deployment, these values may be quantized or rounded according to the numerical resolution of the target processor, with care taken to preserve numerical stability and voltage prediction accuracy.

5.3.4.2 Method Selection and Model Validation

The lookup-table-based parameterization strategy was selected because it offers a direct and transparent way to represent SOC-dependent battery behavior while maintaining low computational cost. Unlike adaptive observers or online optimization techniques, this approach does not introduce additional dynamic states or tuning complexity, making it well suited for deterministic and reliable operation in embedded BMSs.

To validate the model, a charge pulse was applied, and the voltage response was analyzed. The simulation results, shown in Figure 5.8, display the current profile (top) and the corresponding terminal voltage (bottom) for both 1RC and 2RC models. The procedure

mimics a common battery testing method used for system identification, in which a constant current I_0 is applied for a brief period while monitoring the voltage response.

Upon application of the current pulse, the model exhibits an instantaneous voltage drop due to the internal ohmic resistance R_0, known as the ohmic drop $V_\Omega = I_0 \cdot R_0$. This is followed by a fast voltage relaxation governed by the $R_1 \parallel C_1$ branch, representing rapid electrochemical reactions near the electrode surface. Subsequently, a slower voltage evolution emerges due to the $R_2 \parallel C_2$ branch, which accounts for ionic diffusion and transport processes within the cell. After the pulse ends and the current returns to zero, the voltage begins to recover in reverse order: first the fast dynamics (RC1), then the slow relaxation associated with RC2.

The point where the voltage reaches approximately 63.2% of its full recovery corresponds to one time constant ($\tau = RC = 1200$ s), while the system reaches near full recovery (99%) at around $4\tau \approx 3600$ s.The agreement between the simulated response and the expected electrochemical behavior confirms the validity of the lookup-table-based parameterization approach.

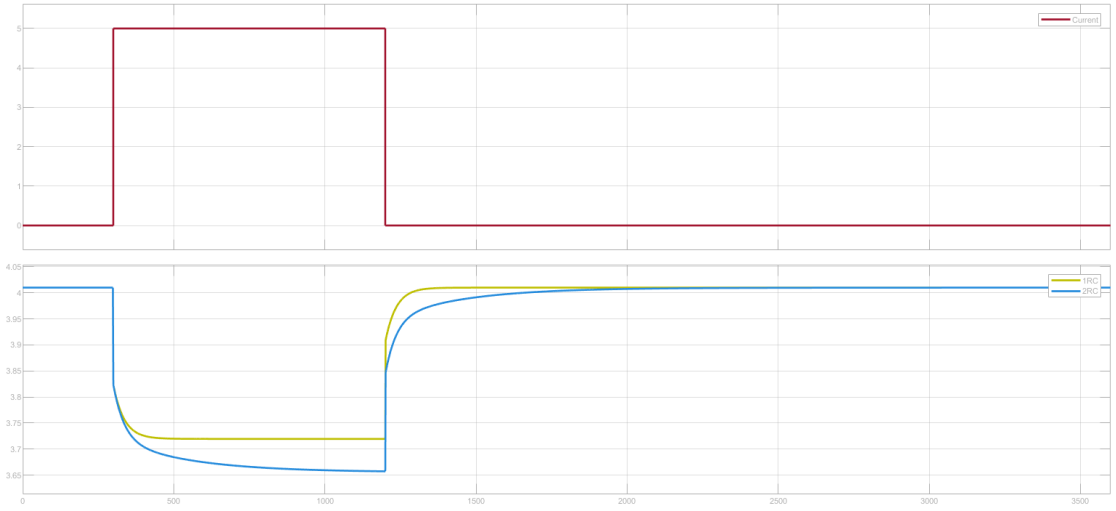

FIGURE 5.8: Simulated voltage response to a charge pulse: 1RC vs. 2RC models.

5.3.4.3 Physical Interpretation of Model Components

- **Ohmic Resistance (R_0):** Accounts for instantaneous voltage changes due to resistance in electrodes, electrolyte, and interconnects.
- **RC1 Branch ($R_1 \parallel C_1$):** Represents fast dynamic effects such as charge transfer and double-layer formation near the electrode surface.

- **RC2 Branch ($R_2 \parallel C_2$):** Captures slower ion diffusion and mass transport phenomena within the battery.

5.3.4.4 Comparison of 1RC and 2RC Simulation Results

- The 1RC model captures only a single time constant, making it insufficient for modeling long-term voltage relaxation. It tends to oversimplify real battery dynamics and converges prematurely.
- The 2RC model, on the other hand, accurately captures both fast and slow relaxation behaviors, resulting in a more realistic and complete voltage profile under dynamic loading.
- In Figure 5.8, the voltage output of the 2RC model shows a more gradual and smooth transition, matching expected physical behavior more closely than the 1RC model.

The implementation of parameter-dependent lookup tables and the use of a 2RC equivalent circuit provide a robust modeling framework for lithium-ion battery behavior. The model effectively captures the voltage dynamics at multiple time scales, making it highly suitable for BMS applications that require accurate real-time state estimation and control under varying load conditions.

Chapter 6

State of Charge Estimation Algorithm

This chapter presents a concise study of the SOC estimation framework developed for the BMS used in electric mobility applications. It outlines the theoretical foundations of SOC behaviour in lithium-ion batteries, including the mathematical representation of charge depletion, the distinctions between charge-based and energy-based estimation, and the impact of nonlinear voltage characteristics on accuracy. These fundamentals support safe operation, reliable diagnostics, and efficient energy utilisation in modern electric vehicles. To address the shortcomings of classical Coulomb Counting, such as integration drift and temperature-dependent capacity variations, the chapter motivates the adoption of an Advanced Coulomb Counting strategy incorporating OCV-based correction and rest-state detection. The approach is validated using a simulation environment that couples the 2RC cell model developed in the previous chapter with the proposed estimation algorithm, enabling realistic evaluation of dynamic response and embedded implementation feasibility. Together, these elements establish a robust methodological foundation for the SOC estimation technique implemented in this work.

6.1 Fundamentals of SOC Estimation

SOC represents the amount of energy remaining in a battery relative to its full capacity. It is one of the most essential variables for battery control and diagnostics, ensuring safe operation, optimal performance, and long-term battery health [43, 44]. As introduced in

Section 2.3.2.1, SOC reflects the battery's available charge as a percentage of its usable capacity and is crucial for managing energy flow, estimating vehicle range, and implementing protection mechanisms in electric mobility applications [45].

The SOC at time t is mathematically defined as:

$$\mathrm{SOC}(t) = \frac{Q_{\mathrm{remaining}}(t)}{Q_{\mathrm{total}}} \times 100\% \tag{6.1}$$

where $Q_{\mathrm{remaining}}(t)$ is the remaining charge at time t, and Q_{total} is the nominal or rated capacity of the battery [46].

In practical BMS applications, batteries operate under dynamically varying loads. Under such conditions, SOC evolution is non-linear, and accurate estimation requires integrating the battery current over time:

$$\mathrm{SOC}(t) = \mathrm{SOC}(t_0) - \frac{1}{C_{\mathrm{rated}}} \int_{t_0}^{t} I(t)\, dt \tag{6.2}$$

Here, $I(t)$ is the discharge current (positive during discharge), and C_{rated} is the rated capacity in ampere-hours (Ah). This method, known as *Coulomb Counting*, is widely adopted in embedded BMS platforms due to its computational efficiency and straightforward implementation [47, 48].

Despite its popularity, Coulomb Counting suffers from well-known limitations such as integration drift, sensor offset, accumulator error, and its inability to account for self-discharge or temperature-dependent capacity changes [43, 49]. To improve robustness, SOC estimation is typically combined with additional techniques such as Open Circuit Voltage (OCV) correlation, Kalman filtering, or machine learning models, as extensively reviewed in [44, 46]. These hybrid methods reduce drift accumulation and improve long-term accuracy in dynamically varying conditions, especially for lithium-ion chemistries.

The work presented here builds upon the ECM-based modelling strategy described in Section 2.3.1.3, which is consistent with established methodologies in battery modelling [49, 50]. The SOC estimation scheme is aligned with the implementation strategies discussed in Chapter 5 and introduces a refined Advanced Coulomb Counting method tailored to embedded systems. This enhanced approach prioritizes computational efficiency, drift mitigation, and practical accuracy under real-world electric mobility operating scenarios.

6.2 Charge-Based vs. Energy-Based SOC Estimation

SOC quantifies the remaining usable capacity of a battery and can be estimated either in terms of charge (Ah) or energy (Wh). The charge-based method is the most widely implemented in Battery Management Systems due to its simplicity and low computational burden [43, 48]. It relies on integrating the measured current over time, a technique known as Coulomb Counting. This approach assumes that the current flowing into or out of the battery is accurately measurable and that an initial SOC value is known. Mathematically, it is expressed as:

$$\mathrm{SOC}_{\mathrm{Ah}}(t) = \mathrm{SOC}(t_0) - \frac{1}{C_{\mathrm{rated}}} \int_{t_0}^{t} I(t)\, dt \tag{6.3}$$

where $I(t)$ is the current drawn from the battery and C_{rated} is the rated capacity in ampere-hours.

Alternatively, energy-based SOC estimation computes the energy removed from the battery by multiplying the instantaneous current with the terminal voltage [46, 44]. This method inherently captures the nonlinear voltage behaviour of lithium-ion batteries during discharge and is given by:

$$\mathrm{SOC}_{\mathrm{Wh}}(t) = \mathrm{SOC}(t_0) - \frac{1}{E_{\mathrm{rated}}} \int_{t_0}^{t} V(t) \cdot I(t)\, dt \tag{6.4}$$

where $V(t)$ is the terminal voltage and E_{rated} is the total energy capacity in watt-hours.

Because lithium-ion cell voltage exhibits a nonlinear relationship with SOC, the difference between $\mathrm{SOC}_{\mathrm{Ah}}$ and $\mathrm{SOC}_{\mathrm{Wh}}$ becomes significant under dynamic load conditions. Whereas charge-based estimation assumes linear depletion under constant current, energy-based estimation reflects the true available energy more accurately by accounting for voltage sag, internal resistance effects, and relaxation behaviour [49, 50]. This distinction is illustrated by the OCV–SOC curve in Figure 6.1, where the open-circuit voltage varies nonlinearly across the SOC range.

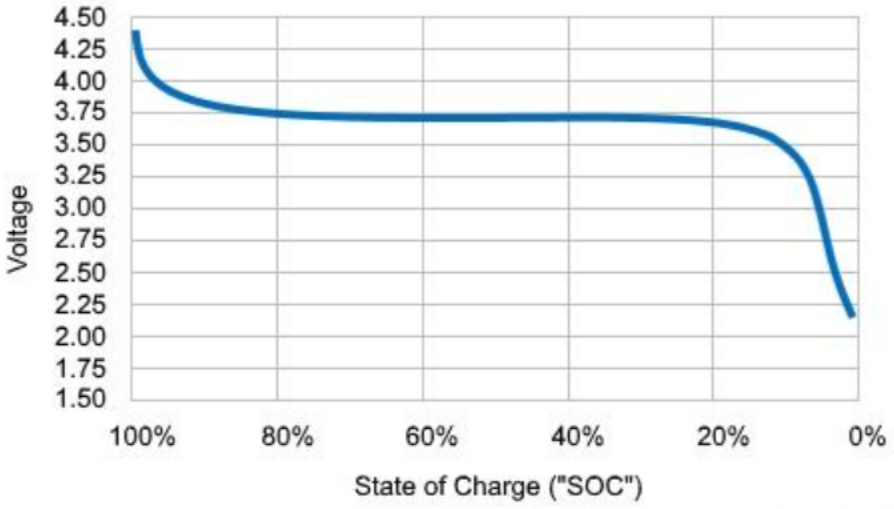

FIGURE 6.1: Open Circuit Voltage (OCV) vs. SOC curve showing nonlinear voltage behavior during discharge.

Ultimately, the choice between charge-based and energy-based SOC estimation depends on system requirements. Charge-based estimation offers computational simplicity and is suitable for low-cost embedded systems, whereas energy-based estimation provides improved accuracy in scenarios where voltage dynamics play a significant role, such as high-power or highly dynamic electric mobility applications.

6.3 Coulomb Counting and Its Limitations

Coulomb counting is one of the most widely adopted methods for estimating the SOC in battery management systems due to its simplicity, low computational cost, and suitability for embedded platforms [43, 48]. As introduced in Equation 6.3, this method computes $\mathrm{SOC}_{\mathrm{Ah}}(t)$ by integrating the measured current over time and comparing it to the battery's rated capacity. It is commonly implemented in electric mobility applications, portable electronics, and industrial battery systems because it does not require complex battery models or intensive numerical computations [44].

While robust under ideal measurement conditions, Coulomb counting suffers from several critical limitations that reduce its accuracy over long operational periods [43, 46]:

- **Sensor Accuracy and Drift:** The method relies heavily on current measurement accuracy. In practice, current sensors are subject to bias drift, calibration error,

and stochastic noise. Even small deviations, such as a drift of only a few milliamps, accumulate significantly over time, leading to SOC estimation errors [48].

- **Cumulative Error:** Because Coulomb counting is an open-loop integration method, any measurement error accumulates indefinitely. This long-term integration drift is one of the primary weaknesses of pure Coulomb counting schemes and can lead to SOC estimates deviating several percent after extended use [43].
- **Self-Discharge Neglect:** Batteries exhibit natural self-discharge due to internal parasitic reactions. Since Coulomb counting registers SOC changes only when a measurable external current flows ($I(t) = 0$ otherwise), self-discharge is ignored, causing discrepancies between estimated and true SOC, especially under long rest periods [49].
- **Temperature Dependence:** Coulomb counting assumes a constant battery capacity. However, the effective capacity varies with temperature and aging. At low temperatures the available capacity decreases significantly, while battery ageing reduces it permanently [44]. If unaccounted for, these variations lead to SOC misrepresentation.

These limitations motivate the adoption of hybrid SOC estimation methods that combine current integration with voltage-based correction mechanisms such as OCV correlation, Kalman filtering, or model-based observers [46, 44]. Such techniques compensate for drift, improve long-term accuracy, and enhance robustness in dynamic electric mobility environments.

6.4 Advanced Coulomb Counting

To address the limitations of classical Coulomb Counting, Advanced Coulomb Counting incorporates the battery's Open Circuit Voltage (OCV) as a correction mechanism. When a battery is at rest (i.e., near-zero current and a stable terminal voltage), the measured terminal voltage approximates the true OCV [43, 44]. By referencing an OCV–SOC lookup table, the integrated SOC value can be corrected to compensate for drift accumulated during dynamic operation [46]. This hybrid approach improves long-term accuracy while retaining the computational simplicity of Coulomb Counting.

In practice, the battery voltage is sampled periodically, and if the system detects a rest state, defined by a sufficiently small current and a negligible rate of change in terminal

voltage, the measured value is mapped to the corresponding SOC from the OCV curve [45]. This corrected SOC replaces the integrated value, effectively resetting drift and ensuring consistency with the cell's electrochemical characteristics. Rest periods naturally occur in electric mobility applications (e.g., after full discharge, during parking phases, or low-power idle modes), providing ideal opportunities for recalibration [44]. These correction events typically maintain SOC accuracy within a 2–3% margin, whereas deviations larger than 7–8% may indicate sensor faults or capacity degradation, prompting additional diagnostic checks.

An alternative technique that offers continuous real-time correction is Kalman Filtering. Kalman-based observers incorporate a full battery model, including OCV, internal resistance, and transient dynamics from RC networks, and adjust SOC estimates at every time step using probabilistic state estimation theory [46, 51]. Unlike Advanced Coulomb Counting, which relies on rest states for recalibration, Kalman filtering provides ongoing drift suppression but requires higher computational capability and accurate model parameterisation, making it less practical for low-power embedded BMS platforms [52].

Overall, Advanced Coulomb Counting provides an effective compromise between computational efficiency and estimation accuracy. By leveraging OCV-based corrections at strategically detected rest intervals, it preserves the simplicity of current integration while mitigating drift, making it well-suited for embedded BMS architectures in electric mobility applications.

6.5 Implementation of Advanced Coulomb Counting for SOC Estimation

6.5.1 Overview of the Simulation System

The implemented system simulates the interaction between a battery pack and a SOC estimation algorithm using a current integration method, commonly referred to as Coulomb Counting. The goal of this simulation is to validate the SOC estimation algorithm under realistic battery behavior conditions by mimicking the operation of an actual battery pack.

The system consists of two major blocks: a battery model and the SOC estimation block. The battery is modeled using an RC equivalent circuit at the cell level, enabling the computation of both terminal voltage and current. The SOC estimation algorithm consumes

these signals to track the state of charge of the battery. Figure 6.2 illustrates the overall simulation setup.

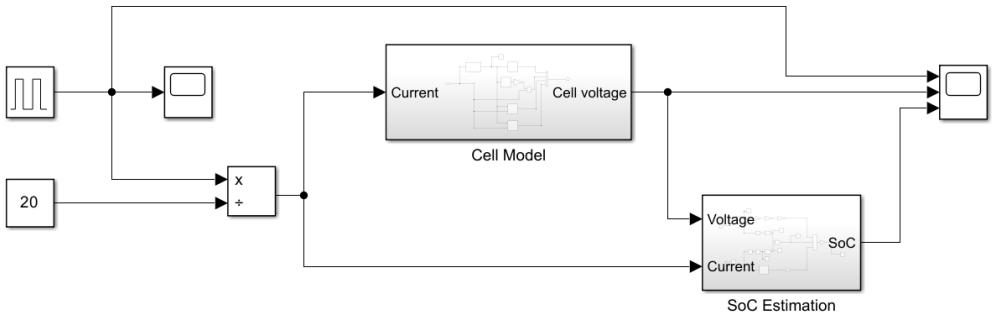

FIGURE 6.2: Simulink block diagram of the overall system showing the Cell Model and SOC Estimation interaction

In this setup, a synthetic 500 A current profile is generated. Assuming the battery pack is made up of 20 cells connected in parallel, the current per cell becomes 25 A. Each cell has a rated capacity of 5 Ah, resulting in a total pack capacity of 100 Ah. This configuration emulates a 5C discharge condition.

The current signal alternates between 500 A discharge and 0 A rest in 50-second intervals, representing a dynamic load profile.

The RC cell model is primarily used to provide voltage outputs that mimic the behavior of a real battery cell. During rest periods (i.e., when the current is approximately zero), the terminal voltage approximates the Open Circuit Voltage (OCV), which is critical for OCV-SOC table referencing.

In the cell model, an ideal SOC computation is included using a basic Coulomb Counting equation without sensor drift or noise, ensuring accurate voltage generation from SOC-OCV lookup tables. This ideal SOC acts as a proxy for the true SOC of a physical battery pack.

Conversely, the SOC estimation block represents the real algorithm to be deployed in hardware. It integrates noisy or drifted current measurements and applies correction strategies such as rest-state detection and voltage settling analysis to update SOC. This block is the only component targeted for embedded code generation and deployment on the actual BMS hardware, while the cell model remains purely a simulation construct.

This simulation framework enables co-simulation of both virtual battery behavior and SOC algorithm performance, providing a closed-loop environment to verify algorithm robustness before deployment.

6.5.2 Ideal SOC Implementation in the Cell Model

The cell model used in this study is based on an RC equivalent circuit representation. This modeling strategy is chosen primarily because it enables simulation of both current and voltage behaviors, which serve as critical inputs to the SOC estimation algorithm. The simulation setup is designed at the cell level to ensure high fidelity in representing individual cell behavior.

In the structure of the cell model, SOC is used internally as an input to multiple look-up tables such as SOC-OCV and SOC-Rs. To accurately retrieve terminal voltage from these tables, we require SOC to be accurate and free from any form of drift or sensor noise. In real battery systems, terminal voltage is physically measurable; however, in simulation environments, we need to mimic this behavior by providing ideal SOC.

Initially, we tested the system by assigning a constant SOC value of 80% to validate the overall architecture. As shown in Figure 6.3, the cell model includes key mappings between SOC and various electrical parameters including open circuit voltage (OCV), internal resistance (Rs), and voltage drops across components. This configuration allows us to produce realistic terminal voltage values that closely mimic a physical battery's response.

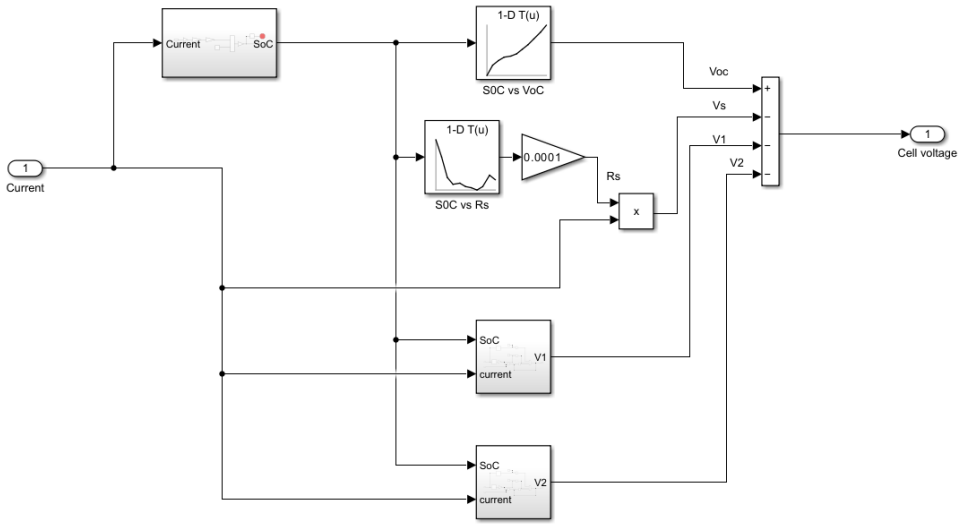

FIGURE 6.3: RC-based cell model using SOC-dependent lookup tables for voltage generation.

Since this SOC is only used for mimicking a real battery's behavior, it must be ideal and immune to any estimation inaccuracies. Therefore, the SOC in the cell model is derived directly from current using a pure Coulomb Counting implementation. This allows for error-free generation of voltage from the SOC-OCV table.

The corresponding implementation of the Coulomb Counting equation is illustrated in Figure 6.4. Here, SOC is initialized with a predefined value and updated through integration of current over time. The process accounts for sign conventions (e.g., negative current for discharge), unit conversions (Ampere to Ampere-hour and seconds to hours), and incorporates a safety stop condition. Specifically, the simulation halts when SOC falls below 0% during discharge. The SOC value is scaled by 100 to represent it as a percentage.

This structure ensures the ideal SOC remains undisturbed by any algorithmic or sensor errors, thus allowing the cell model to behave like a real, physical cell pack. Meanwhile, any noise, drift, or dynamic correction is confined to the separate SOC estimation algorithm, preserving the integrity of the voltage generation in the cell model.

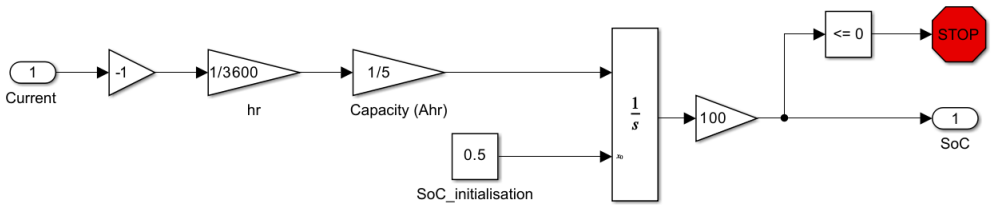

FIGURE 6.4: Ideal SOC computation block using Coulomb Counting for accurate cell model input.

6.6 SOC Estimation with OCV-Based Drift Correction

The proposed SOC estimation approach combines Coulomb Counting with an OCV-based correction mechanism to ensure accurate and drift-resilient tracking under real operating conditions. During normal operation, the algorithm relies on Coulomb Counting by integrating the measured current over time and updating the SOC relative to the rated cell capacity. This provides fast and dynamic response during charging and discharging phases, with the integrator constrained between the physical limits of 0% and 100%.

Because open-loop integration gradually accumulates drift due to sensor bias, noise, and modelling uncertainties, the algorithm incorporates an OCV correction stage activated only during verified rest conditions. A rest state is detected when three criteria are simultaneously met: the absolute current falls below a small threshold (0.01 A), the voltage derivative approaches zero (below 10^{-6} V/s), and no disturbance or drift term is active. Under such conditions, the measured terminal voltage approximates the true Open Circuit Voltage (OCV), allowing the algorithm to retrieve a corrected SOC value from a pre-characterized OCV–SOC lookup table. This corrected SOC replaces the integrator state, effectively eliminating accumulated drift while preserving the responsiveness of Coulomb Counting during dynamic phases.

The workflow of the hybrid estimation strategy is summarized in Figure 6.5. The integrated Simulink implementation is shown in Figure 6.6, where Coulomb Counting and OCV correction operate as two coordinated branches governed by rest-state detection logic.

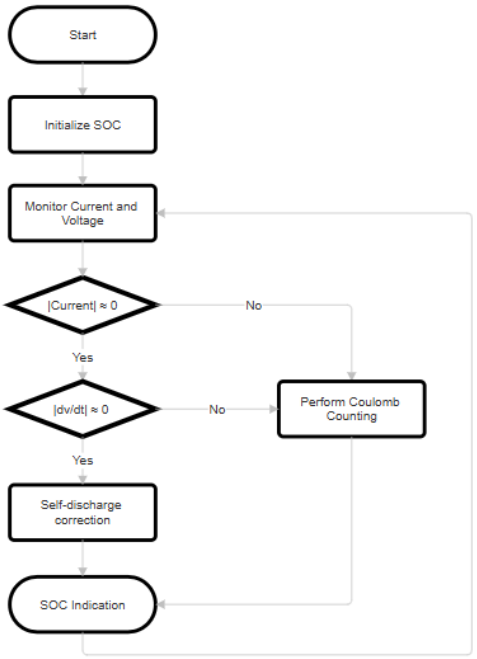

FIGURE 6.5: Flowchart of the Advanced Coulomb Counting SOC estimation algorithm.

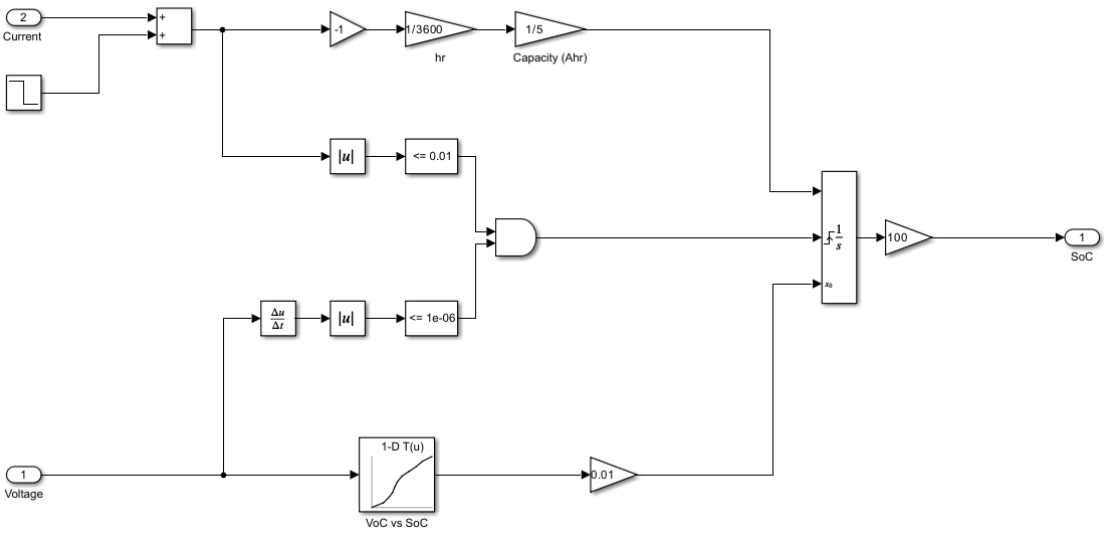

FIGURE 6.6: Simulink implementation of the hybrid SOC estimation algorithm combining Coulomb Counting and OCV-based correction.

The effectiveness of the method is demonstrated in the simulation results presented in Figure 6.7. The applied current profile alternates between high discharge pulses and rest intervals, producing corresponding voltage transients and relaxation behaviour. The estimated SOC closely follows the reference SOC generated by the cell model. During active

discharge, SOC decreases linearly as expected; once the system enters a rest phase, the OCV correction is applied and the estimated SOC converges to the true value, eliminating accumulated drift. This pattern is consistently observed over multiple cycles, validating the robustness of the hybrid approach.

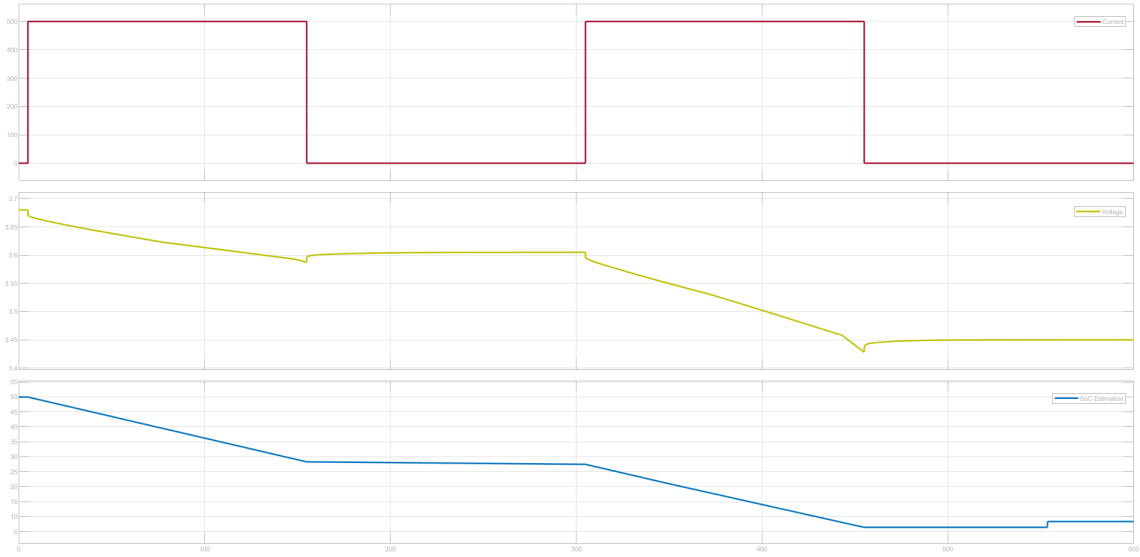

FIGURE 6.7: Simulation results showing input current, terminal voltage, and SOC response with OCV-based correction applied during rest phases.

This hybrid Coulomb Counting–OCV strategy therefore provides an optimal balance between dynamic responsiveness and long-term accuracy, making it well suited for embedded BMS applications where computational constraints and drift sensitivity must be carefully managed.

6.6.1 Enhancements for Robust SOC Estimation: Slope Matching and Temperature Compensation

To further refine the robustness and precision of the SOC estimation algorithm, two advanced features can be incorporated: *slope matching* and *temperature-aware OCV referencing*. These augmentations address limitations arising from dynamic load variations and thermal effects, both of which significantly influence the electrical behaviour of lithium-ion cells [44, 46].

Slope matching enhances SOC accuracy during transient events such as rapid acceleration or regenerative braking, where terminal voltage may shift abruptly due to changes in current and internal resistance. By analysing the derivative of terminal voltage over time

and comparing it against expected dynamic voltage patterns based on historical or model-derived data, the algorithm can detect inconsistencies in its SOC trajectory. When a mismatch is observed between the measured slope and the predicted response, the algorithm can adjust or validate the current SOC estimate, improving resilience under aggressive load conditions [52, 51].

Temperature-aware OCV referencing accounts for the intrinsic dependence of the Open Circuit Voltage (OCV) on cell temperature, a well-documented characteristic of lithium-ion chemistry [49, 50]. Incorporating temperature as an additional input dimension in the OCV–SOC lookup table enables the algorithm to correct SOC estimates for temperature-induced voltage shifts. Two common approaches exist:

1. **Direct sensor-based compensation:** When the battery pack includes reliable thermistors or temperature sensors, their readings can be directly incorporated into the SOC–OCV mapping to extract temperature-corrected OCV values. This method is computationally efficient and suitable for embedded BMS platforms [45].

2. **Model-based temperature estimation:** If sensor data are noisy, delayed, or spatially limited, a thermal model of the battery can be used. Approaches such as lumped thermal models or empirical heat-generation equations can estimate internal cell temperature based on ambient conditions, current flow, and thermal dynamics [53]. The estimated temperature is then used to reference the appropriate temperature-adjusted OCV value.

Both enhancements are modular and can be embedded within the Advanced Coulomb Counting framework without altering its fundamental logic. Their inclusion improves robustness against operational uncertainties such as fast transients and thermal variability, thereby enhancing SOC estimation accuracy in real-world electric mobility applications.

6.7 Embedded Implementation of the SOC Estimation Algorithm

Following the validation of the hybrid SOC estimation strategy in simulation, the algorithm is prepared for real-time deployment on the BMS hardware. To achieve this, the complete Coulomb Counting and OCV-based correction logic is converted into embedded C code using automatic code generation tools integrated within the Simulink environment. This

process ensures a consistent and error-free translation of the validated model into a form suitable for execution on resource-constrained embedded platforms.

The generated C code is incorporated into the firmware of the STM32 microcontroller that serves as the central processing unit of the BMS. System configuration, including ADC sampling routines, current and voltage acquisition, timing management, and memory allocation for SOC variables, is handled within the STM32 development environment. The SOC estimation module operates as part of the periodic control loop, processing sensor data at a fixed sampling rate and updating the SOC estimate accordingly.

Once integrated, the firmware is compiled and flashed onto the actual BMS hardware for hardware-in-the-loop (HIL) and on-device testing. This stage verifies not only the correctness of the algorithm but also its real-time performance, numerical stability, and interaction with the full measurement chain, including current sensing circuits, voltage dividers, temperature sensors, and communication interfaces. Testing on the physical BMS allows observation of drift behaviour, rest-state detection accuracy, and the responsiveness of the OCV correction mechanism under realistic operating conditions.

By deploying the SOC estimation method on the STM32-based BMS, the implementation moves from simulation into a practical, hardware-validated system capable of supporting reliable battery monitoring in electric mobility applications.

Chapter 7

Hardware Design

This chapter presents a comprehensive description of the proposed BMS developed for an electric scooter application. It outlines the system requirements and all design stages, including the conceptual design, technical justification of selected components, and the detailed hardware development process. Particular emphasis is placed on system-level design, electrical dimensioning, and the rationale behind architectural decisions. Additionally, this chapter includes the evaluation and integration of the system's critical subsystems, ensuring their suitability for performance, safety, and reliability.

7.1 System-Level Hardware Design

To ensure optimal performance and safety in electric mobility applications, a custom BMS was developed instead of relying on a commercial off-the-shelf (COTS) solution. Although COTS BMS units offer rapid deployment and low cost, they often operate as closed systems with limited firmware access, restricted configurability, and inadequate support for advanced estimation algorithms or research-oriented diagnostics [54, 55]. A custom-designed BMS enables full control over hardware and software, allowing integration of advanced SOC and SOH algorithms, enhanced fault detection, and higher-resolution telemetry features as recommended in modern EV battery system design literature [56, 57].

The resulting BMS architecture is tailored for a 16-series lithium-ion battery configuration typical of a 60 V electric mobility platform. It provides complete monitoring, balancing, and protection capabilities while maintaining flexibility for algorithm development and embedded implementation.

7.1.1 Battery Pack Selection

The battery pack employs 18650 cylindrical lithium-ion cells (18 mm × 65 mm) arranged in a 16S3P configuration. Lithium Nickel Manganese Cobalt Oxide (NMC) chemistry was selected because of its high gravimetric energy density, favorable power capability, and wide adoption in light electric vehicles [58, 59]. Its performance characteristics make it suitable for the constrained volume of electric scooter decks and other compact electric mobility platforms.

Each cell has a nominal capacity of 2.5 Ah, giving the pack a total capacity of:

$$C_{\text{pack}} = 2.5\,\text{Ah} \times 3 = 7.5\,\text{Ah} \tag{7.1}$$

With a nominal voltage of 3.7 V per NMC cell, the total pack voltage and energy are:

$$V_{\text{nominal, pack}} = 16 \times 3.7 = 59.2\,\text{V} \tag{7.2}$$

$$E_{\text{pack}} = 59.2\,\text{V} \times 7.5\,\text{Ah} = 444\,\text{Wh} \tag{7.3}$$

The allowable operating voltage range based on NMC chemistry is [60]:

$$V_{\text{min}} = 16 \times 2.8 = 44.8\,\text{V} \tag{7.4}$$

$$V_{\text{max}} = 16 \times 4.2 = 67.2\,\text{V} \tag{7.5}$$

To supply a 1000 W motor, the required peak current at minimum voltage is:

$$I_{\text{peak}} = \frac{P}{V_{\text{min}}} = \frac{1000}{44.8} \approx 22.3\,\text{A} \Rightarrow \text{rounded to } 25\,\text{A} \tag{7.6}$$

This battery configuration provides sufficient energy and discharge capability while maintaining compactness for integration in standard electric mobility designs.

FIGURE 7.1: Electric scooter typical battery pack size

7.1.2 System Architecture

A centralized BMS topology is adopted, a configuration widely recommended for compact light electric vehicles due to its reduced wiring complexity, ease of integration, and cost effectiveness [61]. This topology supports up to 16 series-connected cells and integrates measurement, protection, and balancing circuitry on a single PCB.

Key system features include:

- High-accuracy cell voltage measurement ($< 10\,\text{mV}$), consistent with modern AFE capabilities [62, 63]
- Shunt-based current sensing with $\pm 200\,\text{mV}$ resolution
- Temperature sensing via NTC thermistors (three-point measurement)
- Fault detection including over/undervoltage, over/undercurrent, over/temperature, short-circuit, and open-wire conditions [55]
- Passive balancing up to 100 mA per cell
- Estimation of SOC and SoH using embedded algorithms
- On-board data logging for diagnostics and validation

- SPI, I2C, CAN (500 kbit/s), UART communication interfaces
- Optional wireless modules: Bluetooth, Wi-Fi
- Debug interfaces: UART and USB
- Regulated 3.3 V rail for digital subsystems

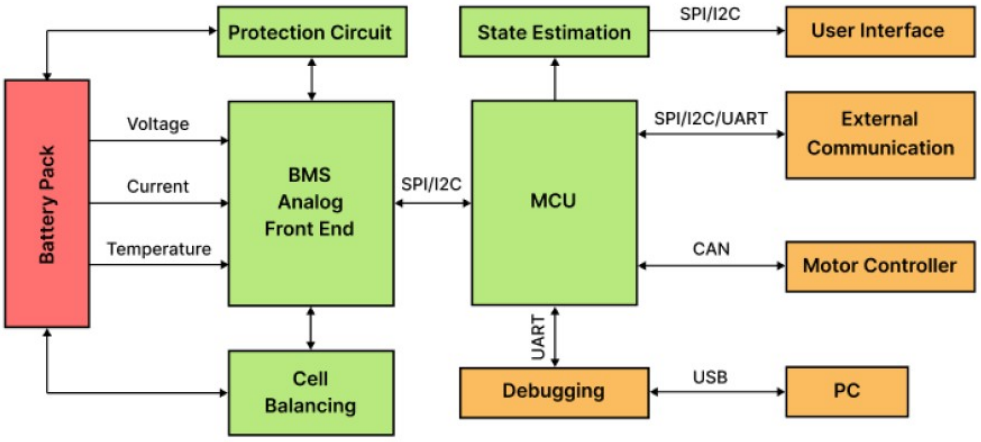

FIGURE 7.2: Proposed Centralized Battery Management System Design

7.2 Hardware Development

The proposed BMS is organized into three principal hardware blocks. The control block includes the microcontroller (MCU), analog front-end (AFE), communication interfaces (UART, CAN), and passive cell balancing circuitry, all of which are standard building elements in modern lithium-ion BMS architectures [55, 56]. The protection block consists of switching MOSFETs and fault-handling components to ensure the pack is electrically isolated during overvoltage, overcurrent, or overtemperature events, following safety practices recommended in EV battery protection literature [54]. The power supply block delivers a regulated 3.3 V derived directly from the battery pack, used to power all digital and analog control circuits.

Hardware design was carried out using Autodesk Eagle for schematic capture and PCB layout [64], allowing for precise footprint placement and efficient routing. Circuit simulation and behavioral validation were conducted in TINA-TI [65], which enabled early-stage performance verification under fault and nominal conditions. The hardware development workflow includes block-level definition, schematic design, simulation, PCB layout, and

prototype validation through field testing, consistent with standard embedded hardware development methodologies [66].

7.2.1 Analog Front-End (AFE)

High-voltage battery packs in electric mobility applications demand accurate and robust monitoring. Selecting a suitable AFE integrated circuit (IC) requires balancing measurement precision, stability, fault protection, cell support, power consumption, and cost. Several devices are widely used in industry, including the MAX14921 [67], the ISL94216 [63], and the BQ76952 [62]. Table 7.1 summarizes their key characteristics for 16-series cell battery systems.

AFE	**MAX14921**	**ISL94216**	**BQ76952**
Cells in Series	16	16	16
Accuracy	±0.5 mV	±5 mV	±5 mV
Current Consumption	10 μA	200 μA	200 μA
ADC	N/A	1 (16-bit)	2 (16-bit)
Cell Balancing	Passive	Passive	Passive
Communication Interfaces	SPI	SPI/I2C	SPI/I2C
Cost	$14.69	$7.16	$5.98

TABLE 7.1: Comparison of common AFEs used in electric mobility BMS applications

The chosen AFE is the Texas Instruments BQ76952 [62], which offers the most cost-effective and feature-rich solution for mid-voltage battery management applications. It supports up to 16 cells in series, features dual 16-bit ADCs, and provides comprehensive monitoring, fault handling, and balancing capabilities consistent with recommendations in TI's technical reference manual [68].

Figure 7.3 illustrates the implemented analog front-end based on the BQ76952. The AFE measures voltages across a 16S cell configuration via pins VC0 to VC16. Each input line is protected by a 20 Ω resistor (R2–R18) and filtered using 100 nF decoupling capacitors (C1–C17), following the filtering guidelines recommended in the datasheet to improve measurement stability and noise immunity [68].

Current sensing is performed across a shunt resistor (R1), connected to the differential inputs SRP and SRN, which the BQ76952 conditions through its internal amplifiers. The internal 1.8 V regulator (REG18) is stabilized with a 2.2 µF capacitor (C21), while the

programmable regulators REG1 and REG2 supply external circuitry and are filtered with capacitors (C22–C25) according to manufacturer recommendations [68].

The BAT pin is connected to the top of the battery stack through a Schottky diode (D1) and a 100 Ω resistor (R19), along with capacitors (C18 and C19), to mitigate voltage spikes and ensure transient protection during switching events. This configuration aligns with TI's protection circuitry recommendations for high-voltage inputs [68].

For regulator input supply, the REGIN pin is driven through a discrete pass element (Q1) and an RC network (R49, C26–C28). Control and protection pins such as `ALERT`, `CFETOFF`, `DFETOFF`, and `RST_SHUT` are pulled up with 10 kΩ resistors (R23, R24), while communication with the MCU is achieved over the I^2C bus using SDA and SCL lines, following the interface configuration described in [62].

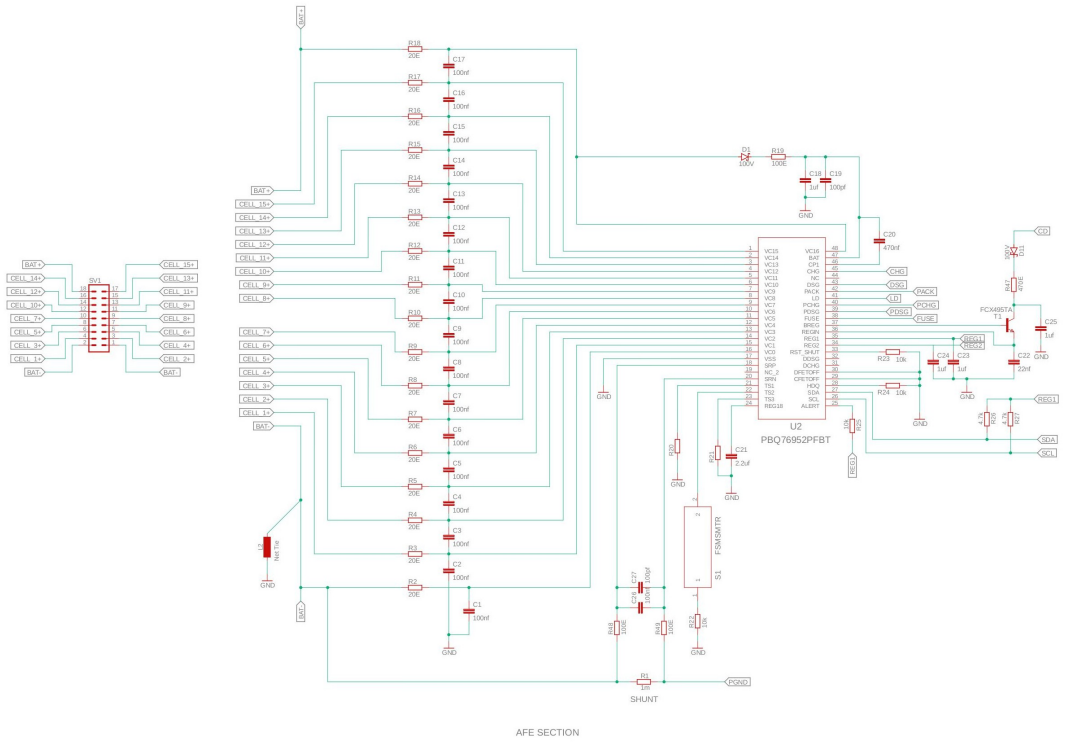

FIGURE 7.3: Full BQ76952 AFE schematic with cell monitoring, shunt current sensing, regulators, and communication interface

7.2.2 Microcontroller

The microcontroller unit (MCU) serves as the brain of the battery management system, responsible for processing the voltage, current, and temperature data acquired from the

AFE. It estimates essential battery states such as SOC and SoH, and performs necessary decisions to ensure reliable operation of the system. In this project, the selected MCU is the STM32H563RIT6 from STMicroelectronics, chosen for its high-speed processing, extensive peripheral set, and industrial-grade reliability suitable for electric mobility applications [69, 70].

Table 7.2 presents a comparison between the STM32H563 and other potential candidates for BMS applications. The ESP32-WROOM-32E is widely used in IoT and low-cost embedded systems [71], while the STM32F303RB [72] and MSP430FR2155 [73] represent established automotive-grade microcontrollers frequently referenced in battery management and power-electronics control platforms.

Brand	**MCU**	**STMicrocontrollers**	**Texas Instruments**
Espressif Systems	ESP32-WROOM-32E	STM32F303RB	MSP430FR2155
Architecture	Dual-core 32-bit	Single-core 32-bit	Single-core 16-bit
Clock Frequency	240 MHz	72 MHz	24 MHz
Flash Size	4 MB	64 KB	20 KB
RAM Size	520 KB	16 KB	32 KB
ADC	2 (12-bit, 18 ch)	2 (12-bit, 21 ch)	1 (12-bit, 12 ch)
Communication Interfaces	UART, I2C, SPI, CAN	UART, I2C, SPI	UART, I2C, SPI
Other Features	Wi-Fi, BLE	N/A	N/A
Cost[2]	$3.00	$8.70	$4.01

TABLE 7.2: Comparison of microcontrollers for BMS applications

The STM32H563RIT6 microcontroller is powered by a stable 3.3 V rail and connected to multiple system components including temperature sensors for each cell. It is interfaced with an external 24 MHz crystal oscillator (XTAL1) for clock generation and a 32.768 kHz oscillator (XTAL2) for RTC operation, in line with recommended hardware layouts in ST application notes [74]. The RESET and BOOT functionalities are supported with appropriate passive components as shown in Figure 7.4.

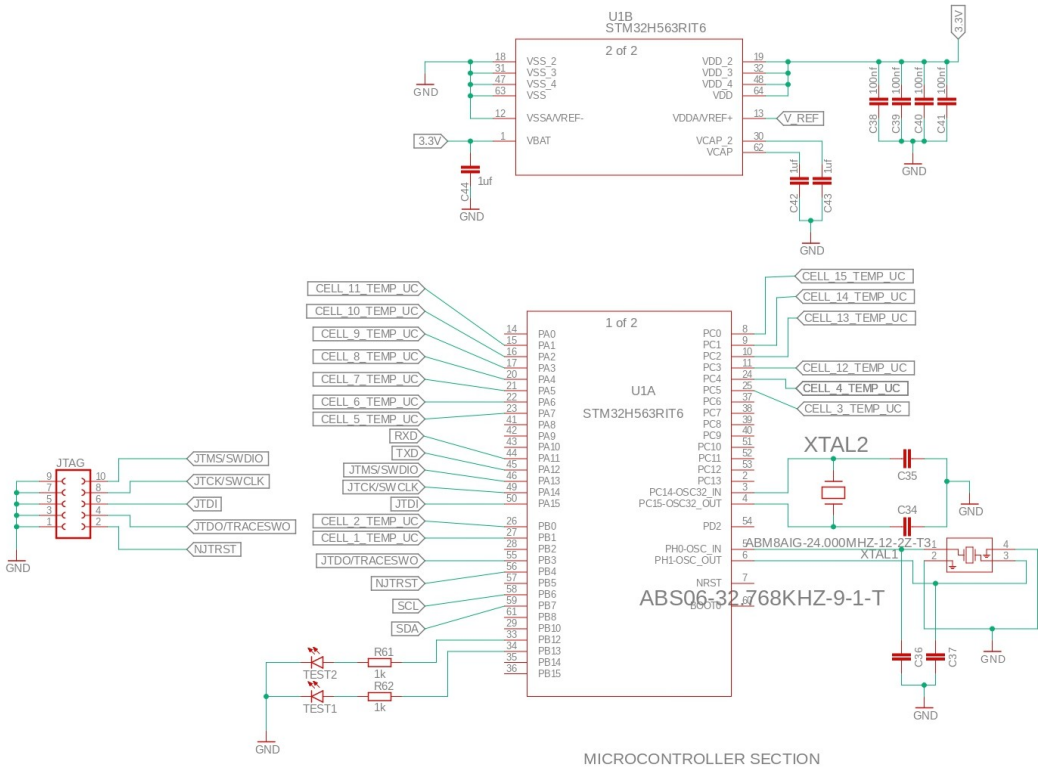

FIGURE 7.4: STM32H563RIT6 MCU schematic section

For robust and reliable vehicle-grade communication, the MCU is interfaced with the TJA1042T CAN transceiver, a high-speed CAN device compliant with ISO 11898-2 [75]. This transceiver is widely used in automotive and light electric vehicles due to its high EMC robustness and deterministic timing [76]. It is powered via the 3.3 V regulator (REG2) output and includes 100 nF decoupling capacitors (C69, C70). The CAN lines (CANH and CANL) are protected against electrostatic discharge and transient spikes using a PESD1CAN diode [77], and 1 kΩ termination resistors (R63, R64), as shown in Figure 7.5.

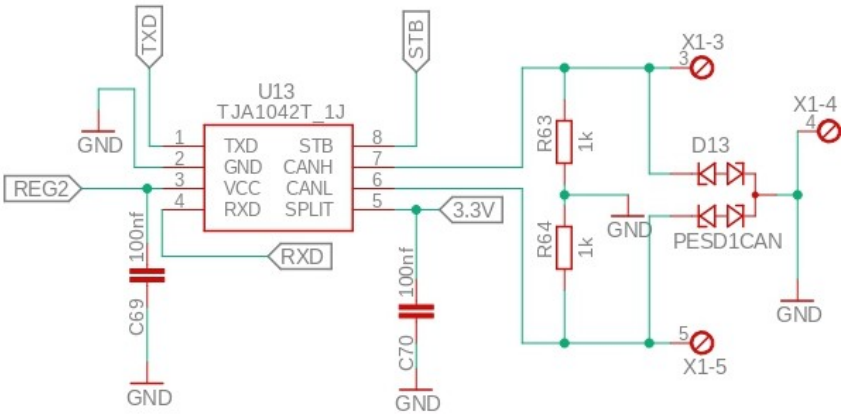

FIGURE 7.5: TJA1042T CAN transceiver circuit

We ran a simulation to test the functioning of the CAN transceiver circuit using an electrical model designed based on the *ISO 11898-2* standard [75]. The model is defined as a two-wire differential bus (CANH and CANL) with a characteristic impedance of 120 Ω, terminated with 120 Ω resistors at both ends. The theoretical voltage levels for dominant and recessive logic states are illustrated in Figure 7.6, adapted from [78]. In the dominant state, the voltage difference between CANH and CANL exceeds 1.5 V, while in the recessive state both lines converge near 2.5 V.

Figure 7.7 shows the simulation results, comparing theoretical behavior with the actual waveforms from the CANH and CANL lines. The dominant and recessive voltage levels align well with the thresholds specified in the TJA1042T datasheet [76], validating compliance with the CAN physical layer.

Despite minor transient distortions, likely due to parasitic cable capacitance and line inductance, the results confirm the electrical integrity of the CAN communication system. This ensures safe, deterministic, and real-time communication between the BMS and vehicle powertrain modules.

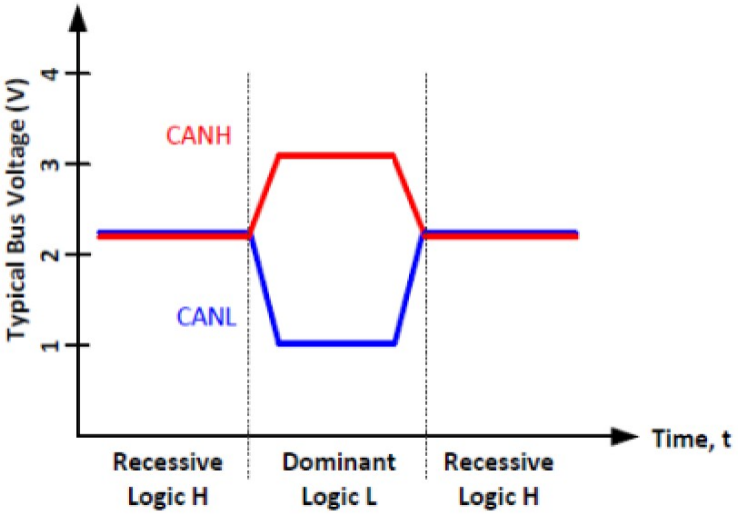

FIGURE 7.6: CAN bus logic states

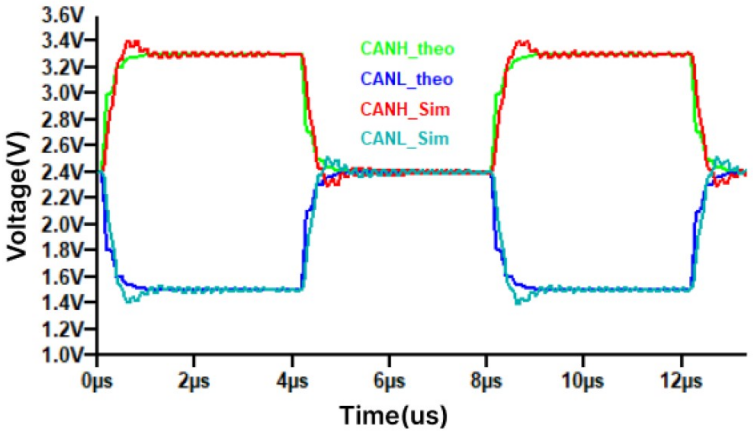

FIGURE 7.7: Simulated vs theoretical CAN bus voltages

This integration ensures safe, deterministic, and real-time communication for power delivery control between the BMS and other vehicle modules.

7.2.3 Current Sensor

As shown in Figure 7.8, a 1 mΩ precision shunt resistor (R1) is placed in the low-side path of the battery pack, allowing the voltage drop across it to be monitored by the `SRP` and `SRN` inputs of the BQ76952 analog front-end [62]. This resistor enables current measurement for both charging and discharging scenarios, with a full-scale voltage drop well below the AFE's ±200 mV input range.

To suppress high-frequency noise and transients, a second-order RC low-pass filter is implemented using 100 Ω resistors (R48 and R49) and two capacitors (C26 = 100 nF, C27 = 100 pF) in parallel. This filter minimizes voltage spikes from switching events and improves the stability and accuracy of current readings.

The chosen shunt resistor (R1) must have a low temperature coefficient, sufficient power rating, and precision terminals. A 3 W, 1 % tolerance, four-terminal (Kelvin-type) shunt resistor, such as the WSK1216L000FEA from Vishay [79], is recommended to achieve high measurement accuracy, especially under dynamic load conditions.

This configuration enables accurate real-time current monitoring with minimal cost and component count, which is essential for SOC, SOH, and protection algorithms in the electric scooter battery management system.

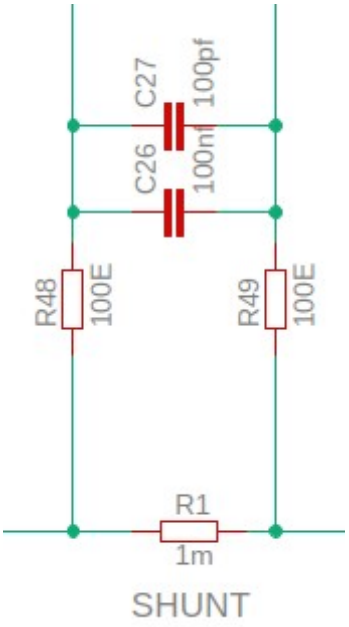

FIGURE 7.8: Low-side shunt resistor current sensing implementation.

7.2.4 Temperature Sensing

Temperature sensing in the BMS is implemented using Vishay's NTCLE203E3103FB0 thermistors, which have a nominal resistance of 10 kΩ at 25 °C and are specified for operation from −40°C to +125°C [80]. These thermistors are integrated into voltage divider networks, each paired with an 18 kΩ pull-up resistor and biased using a 1.8 V reference

voltage. As temperature increases, the thermistor resistance decreases, lowering the divider output voltage. This behaviour is illustrated in Figure 7.9, where the output voltage V_{NTC} follows the nonlinear NTC characteristic.

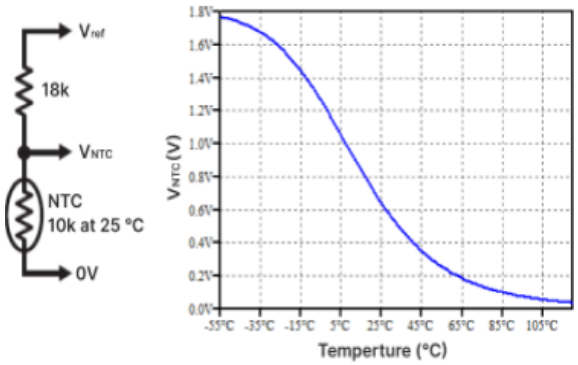

FIGURE 7.9: Voltage divider circuit using a 10 kΩ NTC thermistor with an 18 kΩ pull-up resistor.

The BQ76952 analog front-end (AFE) includes three dedicated temperature sensing inputs (TS1, TS2, TS3), which support external NTC thermistors through internal biasing and filtering networks [62]. Each input is routed through a low-pass RC filter consisting of 100 Ω series resistors, 100 nF and 100 pF capacitors, a 10 kΩ pull-down resistor, and a 1 MΩ bleeder resistor. This filtering suppresses high-frequency noise from long wiring harnesses and improves measurement stability. The implemented TS1 hardware interface is shown in Figure 7.10.

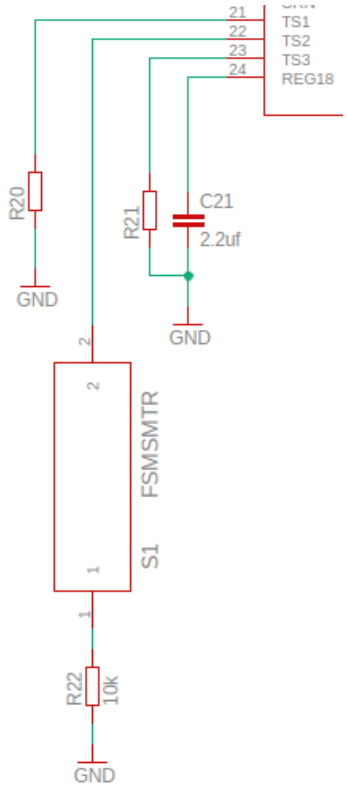

FIGURE 7.10: RC filter and input protection network for TS1 pin of the BQ76952 AFE.

In addition to AFE-based sensing, the BMS includes a distributed NTC interface that monitors individual cell temperatures. Up to sixteen thermistors are connected through 10 kΩ pull-up resistors and 220 nF decoupling capacitors, which filter noise before the signals reach the microcontroller's ADC inputs. The STM32 ADC acquisition supports NTC measurement using look-up tables or the Steinhart–Hart equation, following ST's recommended temperature-sensing design practices [81]. The overall per-cell NTC measurement network is shown in Figure 7.11.

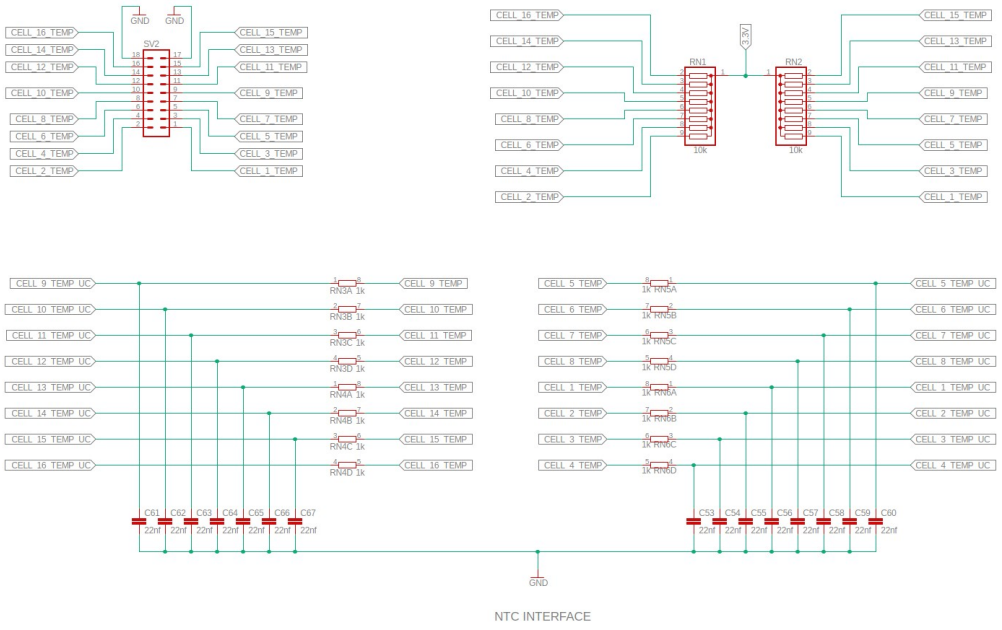

FIGURE 7.11: NTC interface circuit for per-cell temperature monitoring using microcontroller ADC channels.

This dual-layer temperature sensing strategy, centralized pack monitoring through the AFE and distributed cell-level monitoring through the MCU, enhances thermal reliability and resolution. It provides critical safety information such as overtemperature, undertemperature, and thermal runaway indicators, enabling proactive thermal protection and improving battery pack longevity.

7.2.5 Protection

To ensure safety of the battery pack and prevent operation outside its Safe Operating Area (SOA), an active protection strategy is implemented using switching elements. N-channel MOSFETs are selected due to their low on-resistance ($R_{DS(on)}$), high current capability, fast switching performance, and cost efficiency, which make them ideal for battery protection applications [82]. Although MOSFETs conduct current preferentially in one direction, bidirectional current flow is required for both charging and discharging. Therefore, separate MOSFET banks are used for each path, driven by the dedicated charge (CHG) and discharge (DSG) gate outputs of the BQ76952 analog front-end [62].

The switching architecture uses eight STL110N10F7 automotive-grade MOSFETs [83], arranged with four devices in parallel for charging and four for discharging. Paralleling reduces conduction losses, improves thermal distribution, and enhances reliability under

high load conditions. The MOSFETs are placed at the positive end of the pack and arranged in a back-to-back drain configuration, which is standard practice for bidirectional battery protection stages [84].

During charging, the CHG MOSFET bank is activated by the BQ76952 gate driver, allowing current to flow from PACK+ through the body diode of the discharge MOSFETs and then through the CHG FETs to BAT+. Conversely, during discharging, the DSG MOSFETs are turned on, allowing current to flow in the opposite direction, as illustrated in Figure 7.12. The primary electrical characteristics of the STL110N10F7 MOSFETs used in this system are listed in Table 7.3.

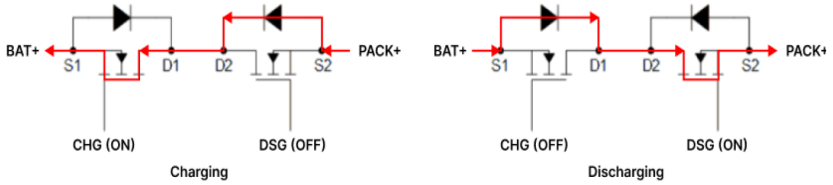

FIGURE 7.12: Protection FETs driving during charging and discharging

TABLE 7.3: STL110N10F7 MOSFET specifications

Parameter	**Rating**
V_{DS} maximum voltage	100 V
V_{GS} maximum voltage	±20 V
$V_{GS(th)}$ threshold voltage	2–4 V
$R_{DS(on)}$	6.5 mΩ at $V_{GS} = 10$ V
I_D maximum drain current	80 A at 25°C
Q_g total gate charge	48 nC at $V_{GS} = 10$ V
Power dissipation	125 W

Pre-Charge Control Mechanism

High-voltage battery systems connected to capacitive loads are highly susceptible to inrush currents during initial energisation. When the high-voltage contactor closes while the downstream DC-link capacitor is fully discharged, a large surge current flows as the capacitor attempts to charge instantaneously. Such inrush events can damage contactors, stress MOSFETs, and trigger nuisance tripping of protection circuits. For this reason, pre-charge control is a standard requirement in traction and industrial battery systems [85, 86].

To mitigate this, the BMS implements a pre-charge control mechanism that ensures a controlled and safe voltage ramp-up before the main power path is fully enabled. Figure 7.13 illustrates the pre-charge architecture. Instead of immediately closing the main contactor, the BMS first activates a dedicated pre-charge contactor that routes current through a pre-charge resistor. This resistor limits the inrush current and gradually charges the load (DC-link) capacitor. Once the capacitor voltage approaches the battery voltage, typically above 90–95%, the BMS closes the main contactor and subsequently disables the pre-charge path [87].

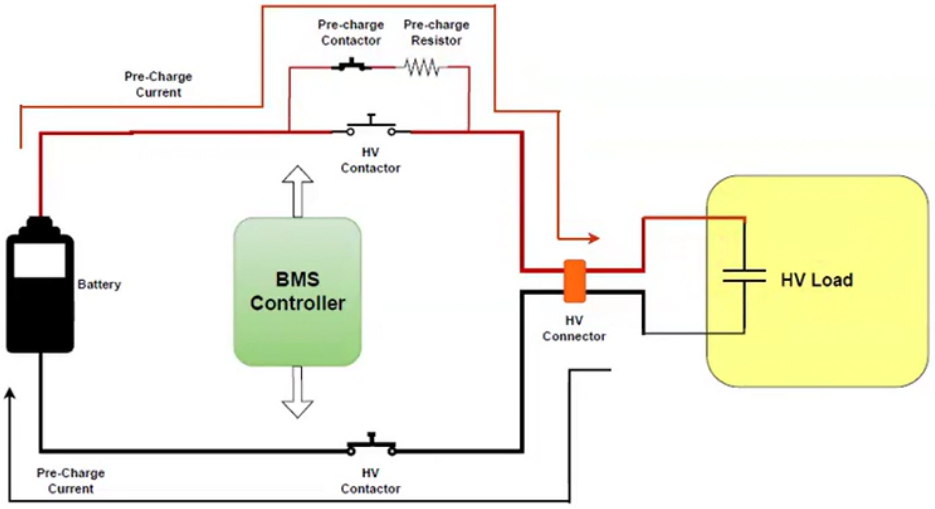

FIGURE 7.13: Pre-charge circuit managed by the BMS. The pre-charge contactor and resistor limit inrush current while the load capacitor charges to a safe level.

The capacitor voltage follows the standard exponential RC charging profile:

$$V_C(t) = V_S \left(1 - e^{-t/RC}\right) \tag{7.7}$$

where $\tau = RC$ is the circuit time constant. As described in classical RC charging theory [88], the capacitor reaches approximately 63% of the supply voltage after one time constant and more than 98% after four time constants. This behaviour is illustrated in Figure 7.14.

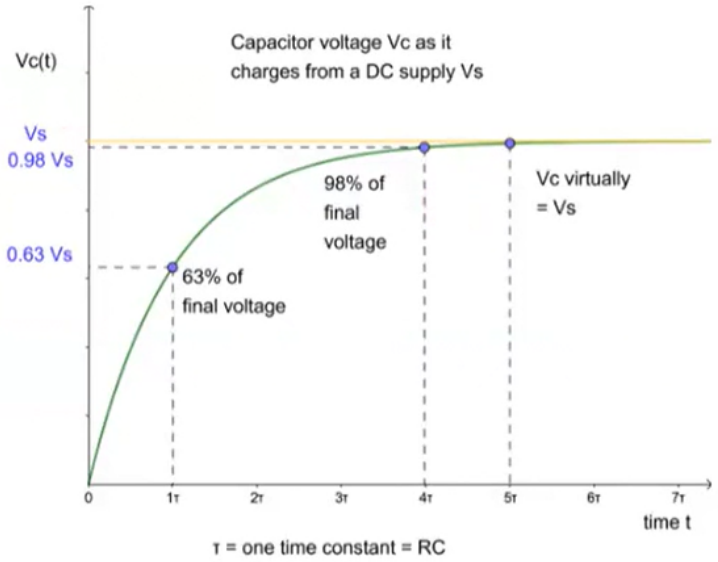

FIGURE 7.14: Exponential rise of capacitor voltage during charging through a pre-charge resistor.

To validate the behaviour, a TINA-TI simulation was performed using the circuit shown in Figure 7.15. The resulting waveforms in Figure 7.16 closely match the theoretical profile, confirming that the pre-charge resistor effectively limits inrush current.

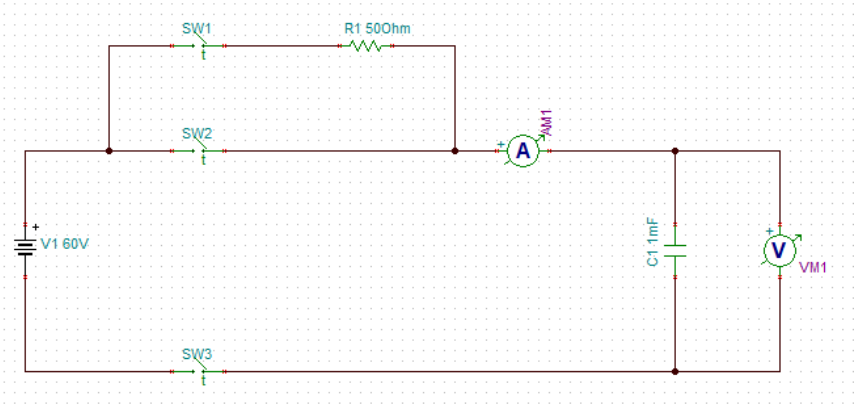

FIGURE 7.15: TINA-TI simulation schematic of the pre-charge circuit.

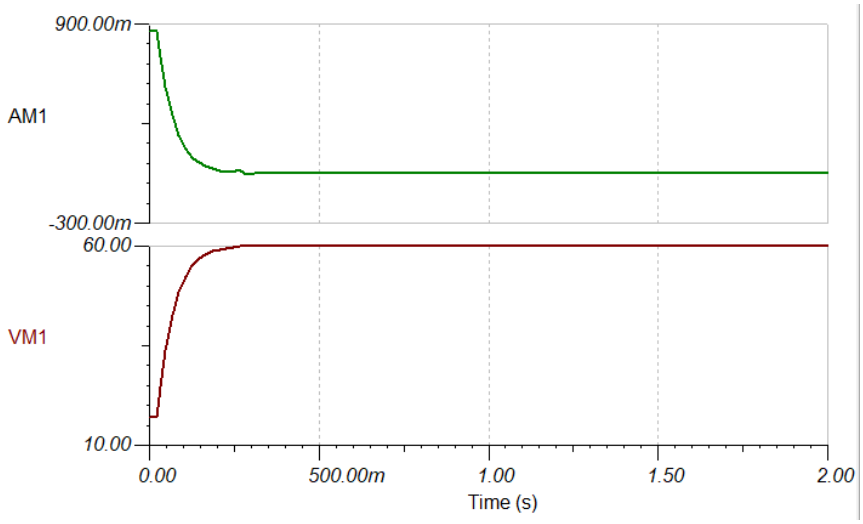

FIGURE 7.16: Simulation results showing capacitor voltage (VM1) and inrush current (AM1) during pre-charge.

Charge and Discharge FET Switching Behaviour

In modern Battery Management Systems, power-path control is commonly implemented using back-to-back N-channel MOSFET configurations, enabling safe and efficient gating of charge and discharge currents [89, 90]. This topology provides bidirectional blocking capability, low conduction losses, and fast switching response, making it well-suited for electric mobility applications where current transients and regenerative braking introduce rapid load variations [91].

To analyse the dynamic behaviour of the charge and discharge switching stages in the proposed BMS, a simplified power-stage model was developed in the TINA-TI simulation environment. The model uses two NMOS transistors representing the charge-FET and discharge-FET, respectively. Each transistor is driven by an independent gate signal (VG1 for charging and VG2 for discharging), replicating the control scheme implemented by the BQ76952 gate drivers. This abstraction allows evaluation of switching transitions, conduction phases, and the effect of body diode conduction during direction reversals, consistent with MOSFET operation theory [92, 88].

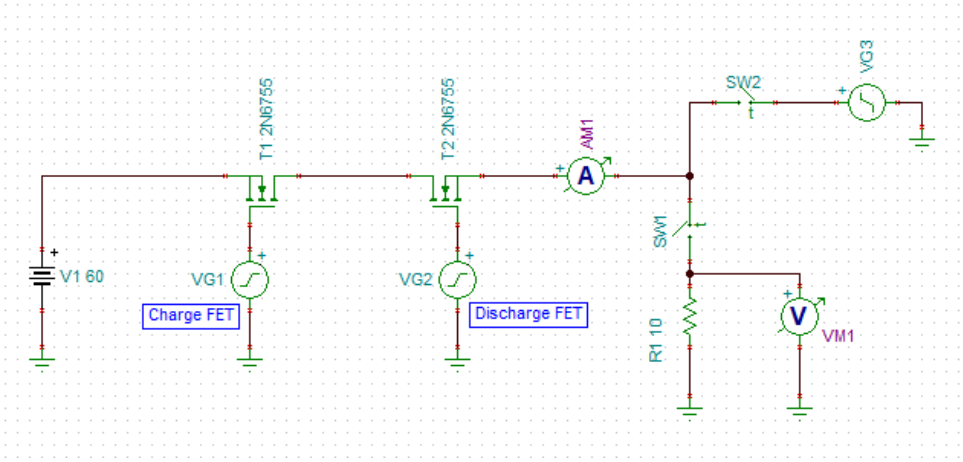

FIGURE 7.17: Simulation schematic of the charge and discharge FET control.

The simulation circuit is shown in Figure 7.17. When VG1 is asserted, the charge path becomes active, enabling controlled current flow into the battery pack. Conversely, asserting VG2 activates the discharge path, allowing current delivery to the load. The resulting current and voltage behaviour is plotted in Figure 7.18. The measured current (AM1) and voltage (VM1) exhibit clean switching transitions aligned with the applied gate signals, confirming correct bidirectional conduction and validating the design assumptions used in the hardware implementation.

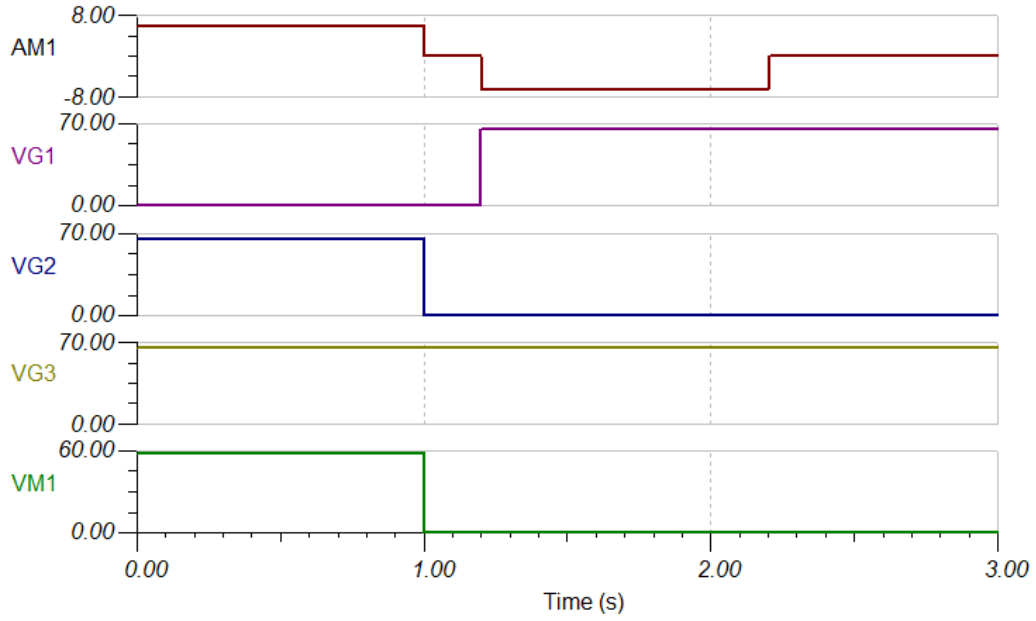

FIGURE 7.18: Simulated waveforms showing gate-drive signals and resulting current/voltage behaviour.

These simulations provide insight into gate-drive timing, conduction symmetry, and switching losses, factors that are crucial for ensuring MOSFET reliability and preventing thermal overstress in high-current battery systems [93].

The full switching implementation of the protection MOSFETs is shown in Figure 7.19. Gate resistors (100 Ω) are used to control the MOSFETs' turn-on and turn-off speeds and to mitigate high-frequency ringing caused by parasitic inductances, consistent with standard gate-drive design guidelines [90, 94]. Zener diodes are placed between gate and source to clamp voltage spikes and protect the gate oxide from transient overvoltage, as recommended in automotive high-side MOSFET applications [93]. Large-value resistors (10 MΩ) are added to ensure residual charge is discharged from the gate during idle states, preventing unintended turn-on due to leakage currents.

An additional N-channel MOSFET is used as a reverse-polarity protection element. Compared with diode-based protection, MOSFET reverse-blocking significantly reduces conduction losses and is widely adopted in electric mobility and battery protection architectures [95]. When $PACK^+$ is pulled below VSS due to incorrect connection, the MOSFET isolates the battery by cutting off the conduction path, thereby preventing device or cell damage.

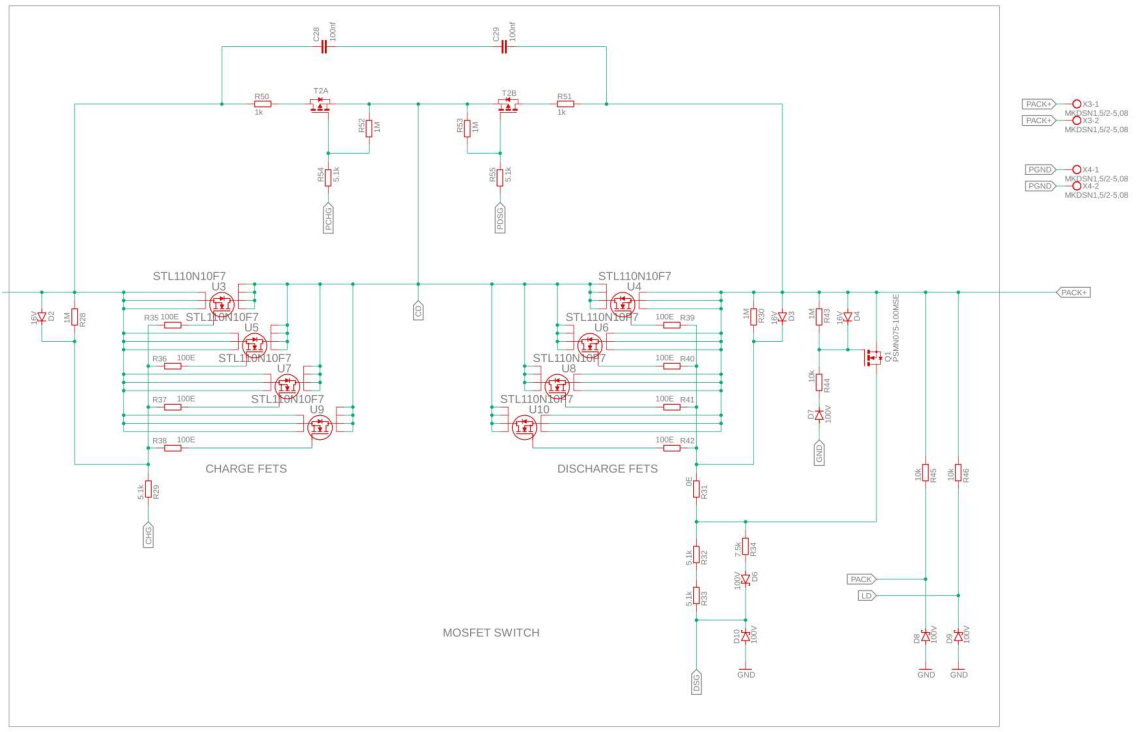

FIGURE 7.19: MOSFET switching protection circuit (Charge/Discharge paths)

Electrostatic discharge (ESD) protection is ensured by decoupling capacitors placed across the high-voltage rails to attenuate high-frequency transients, while 60 V transient voltage suppression (TVS) diodes clamp surge voltages induced by inductive loads or cable transients. TVS devices are commonly deployed in BMS high-voltage interfaces to meet automotive transient immunity standards such as ISO 7637-2 [96]. A secondary protection stage is implemented using a resettable fuse (ITV9550L5030HMR) and a P-channel MOSFET that disconnects the output under sustained overcurrent conditions, functioning as a backup isolation mechanism in accordance with industry practices for redundant battery protection [97].

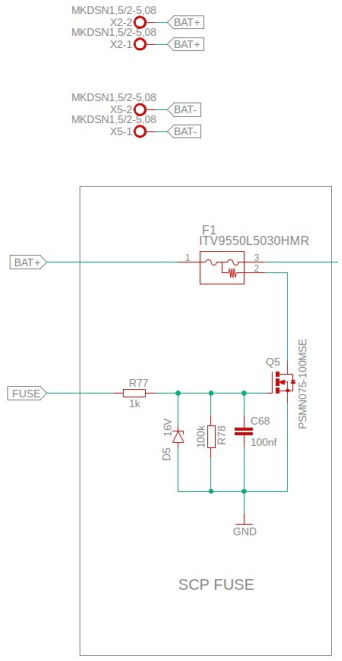

FIGURE 7.20: Secondary overcurrent protection fuse circuit

7.2.6 Cell Balancing

Cell balancing is a crucial functionality in BMS that ensures uniform charge distribution across all cells in a series-connected battery pack, thereby extending battery life and improving performance. In this design, internal passive cell balancing is adopted and implemented through the BQ76952 analog front-end device. Internal balancing is widely used in cost-sensitive and space-constrained applications due to its simplicity and integration level [98, 99].

Passive balancing operates by bypassing the charge of higher-voltage cells through resistive discharge paths, allowing lower-voltage cells to equalize over time. The BQ76952 integrates dedicated balancing FETs that can be activated when a cell exceeds a programmable threshold, controlled through register configurations or MCU commands [68]. This internal architecture reduces external component count and PCB complexity compared with discrete balancing circuitry.

As shown in Figure 7.21, when a specific cell (e.g., C_n) reaches the balancing threshold, the internal switch corresponding to that cell is turned on, creating a discharge path through the series resistor R_n. The current then flows through the balancing resistor network and the internal FET, dissipating excess energy as heat. The balancing current I_b can be

approximated as:

$$I_b = \frac{V_{cell}}{2R_n + R_{DS(on)}} \tag{7.8}$$

where V_{cell} is the cell voltage (typically 4.2 V at full charge), R_n is the input resistor (20 Ω), and $R_{DS(on)}$ is the internal FET on-resistance (25 Ω). Substituting these values yields:

$$I_b = \frac{4.2\,V}{2 \times 20\,\Omega + 25\,\Omega} \approx 65\,\text{mA} \tag{7.9}$$

While passive balancing currents in this range are insufficient for large-capacity energy storage systems, they are appropriate for moderate-capacity lithium-ion packs such as those used in light electric vehicles. The method is thermally stable, reliable, and cost-effective, avoiding the need for external MOSFETs, driver ICs, and complex control logic [100]. This makes it well-suited for compact BMS designs like the one developed in this work.

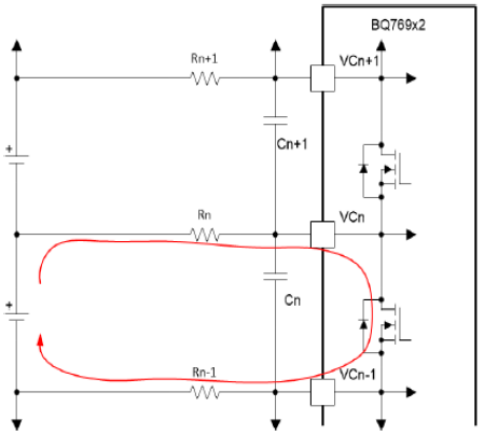

FIGURE 7.21: Internal cell balancing mechanism used by the BQ76952 AFE.

7.2.7 Power Supply Design

The BMS is powered directly from the battery pack. Although the BQ76952 includes integrated low-dropout regulators (LDOs) that provide fixed 1.8 V and programmable 3.0 V/5.5 V outputs, their maximum current capability of 45 mA is insufficient to supply the full system, particularly the microcontroller, voltage-reference circuitry, and communication interfaces [68]. To ensure stable and reliable operation, a dedicated power-management stage was designed, consisting of three functional blocks: a 3.3 V buck regulator, a high-precision reference voltage regulator, and an input filtering and reverse-polarity protection network.

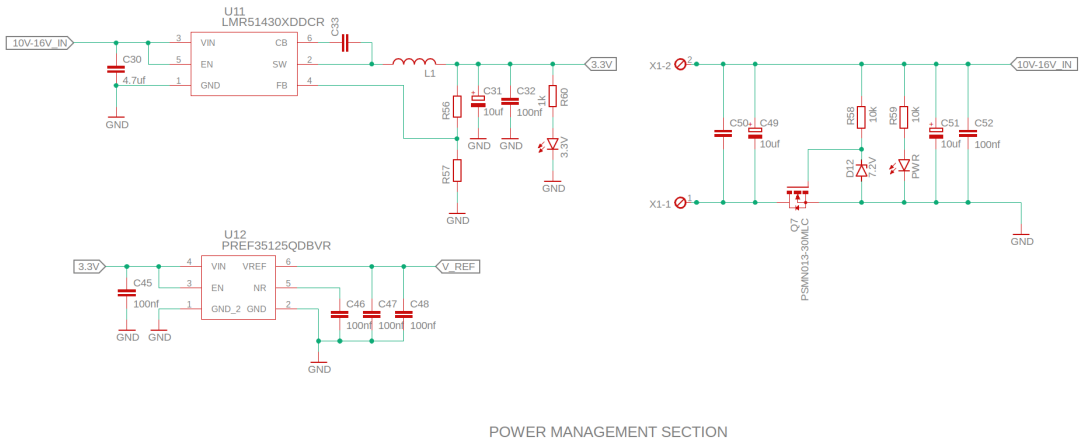

FIGURE 7.22: Power management section schematic

The first stage is a 3.3 V buck regulator built around the LMR51430XDDCR, a high-efficiency synchronous step-down converter from Texas Instruments [101]. It converts the battery voltage (10–16 V) into a stable 3.3 V rail capable of powering the MCU and communication peripherals. A 10 μH inductor (L1) and output capacitors (C31, C32) ensure low output ripple, while resistors R56 and R57 configure the feedback loop. A fast-recovery Schottky diode (D22) is used for reverse-polarity protection, chosen for its low forward voltage and suitability for automotive power stages [102].

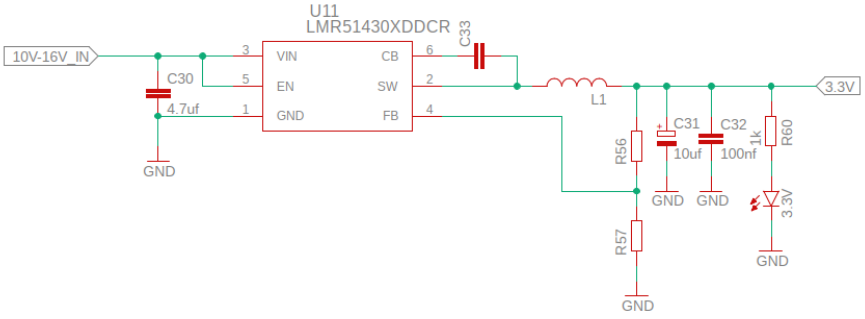

FIGURE 7.23: 3.3 V buck regulator using the LMR51430XDDCR

The second stage provides an accurate voltage reference using the PREF35125QDBVR precision LDO. Precision references are essential for stable analog measurements, particularly for ADC-based current and temperature sensing [103]. The NR and VREF pins are decoupled by three 100 nF capacitors (C46–C48) to minimize high-frequency noise coupling and ensure low output drift.

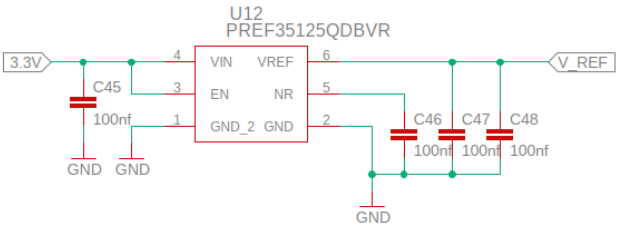

FIGURE 7.24: Precision reference voltage regulator using PREF35125QDBVR

The final stage ensures robustness against wiring errors and electrical disturbances. Reverse-polarity protection is implemented using a PSMN013-30MLC MOSFET from Nexperia [104], configured as a high-side ideal-diode switch. A 12 V Zener diode protects the buck input by clamping transient overvoltages, consistent with recommendations in automotive supply-front-end design guidelines [105]. An array of capacitors (C49–C52) forms a multi-frequency input filter, reducing both switching noise and line disturbances.

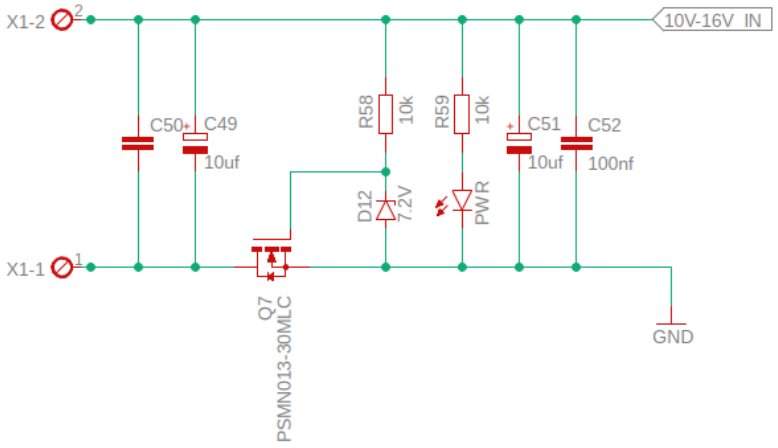

FIGURE 7.25: Input protection and filtering circuit

Overall, this power-management architecture delivers clean and stable supply rails to the MCU, sensors, communication peripherals, and the AFE. Its modular and noise-resilient design follows best practices for mixed-signal automotive systems, ensuring reliable BMS performance across all operating conditions.

7.3 Hardware Implementation Overview

Following the complete schematic design, component selection, and subsystem-level validation, the hardware architecture of the proposed BMS is consolidated into a single integrated platform. All functional blocks, including cell voltage monitoring, current and temperature sensing, power management, protection circuitry, communication interfaces, and control logic, are combined on a custom-designed 2 layer PCB tailored for electric scooter applications.

The hardware development workflow progresses from system-level architecture definition to detailed schematic capture and circuit verification. Key subsystems are validated through analytical calculations and circuit-level simulations to ensure correct electrical behaviour under both nominal and fault conditions. Particular attention is given to safety-critical elements such as protection MOSFETs, current sensing paths, pre-charge control, and power regulation, ensuring robust operation within the battery's safe operating area.

Once the schematics are finalized, the design is translated into a manufacturable PCB layout that respects signal integrity, thermal performance, and high-current routing constraints. The resulting layout integrates all hardware functions into a compact form factor suitable for light electric mobility platforms. Detailed PCB routing views and layout-specific considerations are provided in Appendix B for completeness and documentation purposes.

At this stage, the complete hardware design is considered ready for fabrication, assembly, and experimental testing. The finalized PCB provides the physical foundation for deploying the embedded firmware and SOC/SOH estimation algorithms developed in the previous chapters, enabling future hardware-in-the-loop validation and on-board experimentation.

Chapter 8

Discussion, Future Work, and Conclusion

8.1 Discussion and Future Work

The objective of this thesis was to design and implement a complete BMS for a 16 S lithium-ion battery pack dedicated to an electric scooter application. The project covered both software aspects, such as battery modelling, SOC estimation, and system simulation, and hardware development, including schematic design, protection architecture, PCB layout, temperature and current sensing circuits, and CAN-based communication with the motor controller. The proposed system targets compact light electric vehicles, where safety, efficiency, and reliability are crucial, and where integration constraints require a compact and cost-efficient design.

All hardware blocks were designed, simulated, and integrated into a 100 mm × 80 mm two-layer PCB. The BMS incorporates the Texas Instruments BQ76952 analog front-end, the STM32H563 microcontroller, passive cell balancing, dual-stage protection using MOSFET arrays, a pre-charge mechanism, reverse-polarity protection, and a dedicated power supply stage. Despite the significant progress in design and simulation, the final phases, namely PCB fabrication, hardware prototyping, firmware development, and full validation on an electric scooter, could not be completed due to time constraints, component lead times, and limited access to laboratory testing equipment.

From the modelling perspective, the work built on the Dual Polarisation (2RC) equivalent circuit model developed in this thesis. This model was used to implement an enhanced

Coulomb Counting method with OCV-based drift correction. These algorithms were validated through simulations in MATLAB/Simulink and prepared for later embedded deployment. On the hardware side, each subsystem, including sensing interfaces, MOSFET protection, CAN communication, and power management, was evaluated through circuit-level SPICE simulations, confirming correct functional behaviour.

The following tasks represent the main opportunities for further development:

- **Advanced SOC and SOH Estimation:** Implementation of real-time estimation algorithms, such as Extended or Unscented Kalman Filters, or data-driven approaches, to improve accuracy during dynamic e-scooter operation with high current transients.
- **Enhanced Cell Balancing:** Investigation of higher-current passive balancing or active balancing topologies to extend battery lifetime in intensive daily e-scooter usage.
- **Hardware Prototyping and Road Testing:** Fabrication and assembly of the PCB, followed by full validation on a customized electric scooter platform, including thermal stress tests, fault-injection scenarios, and ride-cycle evaluations.
- **Complete Firmware Development:** Implementation of the embedded software stack: data acquisition, protection logic, SOC/SOH estimation, CAN communication with the motor controller, and event logging.
- **Graphical User Interface (GUI):** Development of a desktop or mobile application for viewing real-time telemetry, adjusting configuration parameters, monitoring battery health, and performing diagnostics.
- **Real-World Data Collection:** Deploying the system on an electric scooter to collect real-world operational data for refining lookup tables, improving estimation accuracy, and validating long-term performance.

8.2 Conclusion

This thesis presented the development of a complete Battery Management System tailored for a 16 S lithium-ion electric scooter battery pack. Beginning with the creation of an accurate electrochemical model based on the Dual Polarisation (2RC) architecture, the work

incorporated an enhanced Coulomb Counting algorithm with OCV-based correction, yielding a practical and robust SOC estimation method suited for embedded implementation.

On the hardware side, a fully integrated centralized BMS architecture was designed. This included voltage, current, and temperature sensing, a multi-layer protection strategy, passive cell balancing, a pre-charge mechanism, CAN communication, and a multi-stage power supply, all optimized for compact integration into an electric scooter's chassis. A complete PCB layout was produced, incorporating industry-standard routing practices, thermal management considerations, and EMC-aware design rules.

Although real-world prototyping and testing remain future work, the thesis successfully delivers a validated, simulation-based design that is ready for fabrication. The system provides a strong technical foundation for building a fully operational BMS for electric scooter applications and can be further extended to other light electric vehicle platforms or small-scale energy storage systems.

Appendix A

Experimental Data for OCV and 2RC Model Parameters

The numerical datasets used to construct the lookup tables for the 2RC equivalent circuit model are summarized in this section. These datasets include the open-circuit voltage (OCV) as a function of the state of charge (SOC), as well as the SOC-dependent parameters R_0, R_1, R_2, C_1, and C_2.

The parameter values are derived from Hybrid Pulse Power Characterization (HPPC) experiments reported by Wenhui Zheng *et al.* [106] and were directly used to populate the one-dimensional lookup tables implemented in the MATLAB/Simulink model.

A.1 Open-Circuit Voltage as a Function of SOC

Table A.1 lists the open-circuit voltage values measured at discrete SOC levels. These values were obtained after pulse–rest discharge tests, where the terminal voltage was recorded once the cell reached electrochemical equilibrium.

TABLE A.1: OCV–SOC data used for lookup table construction (adapted from [106])

SOC (%)	**OCV (V)**
100	4.20
95	4.12
90	4.08
85	4.04
80	4.00
75	3.97
70	3.94
65	3.91
60	3.89
55	3.87
50	3.85
45	3.83
40	3.81
35	3.79
30	3.77
25	3.75
20	3.73
15	3.71
10	3.69
5	3.65

A.2 SOC-Dependent 2RC Model Parameters

Table A.2 summarizes the SOC-dependent parameters of the 2RC equivalent circuit model. The parameters were identified from voltage relaxation curves during HPPC testing using curve-fitting techniques.

TABLE A.2: SOC-dependent 2RC model parameters (adapted from [106])

SOC (%)	R_0 (mΩ)	R_1 (mΩ)	C_1 (F)	R_2 (mΩ)	C_2 (F)
100	2.1	1.8	2400	3.5	8200
90	2.2	1.9	2300	3.6	8000
80	2.4	2.0	2200	3.8	7800
70	2.6	2.1	2100	4.0	7600
60	2.8	2.3	2000	4.3	7400
50	3.0	2.5	1900	4.6	7200
40	3.3	2.8	1800	5.0	7000
30	3.6	3.1	1700	5.5	6800
20	4.0	3.5	1600	6.0	6600
10	4.5	4.0	1500	6.8	6400

Appendix B

PCB Layout and Routing

The PCB layout integrates all major functional blocks required for an electric scooter BMS, including the Analog Front-End (AFE), microcontroller unit (MCU), power MOSFET switching stage, current sensing circuitry, protection elements, and communication interfaces. The following figures illustrate the physical implementation and routing organization of the board.

B.1 Top Layer PCB Layout

Figure B.1 shows the top-layer layout of the PCB, highlighting the placement of the main functional blocks such as the AFE circuit, MCU, MOSFET switching circuit, current sensing stage, and power management circuitry. Component placement prioritizes short high-current paths, reduced loop areas, and physical separation between analog, digital, and power domains.

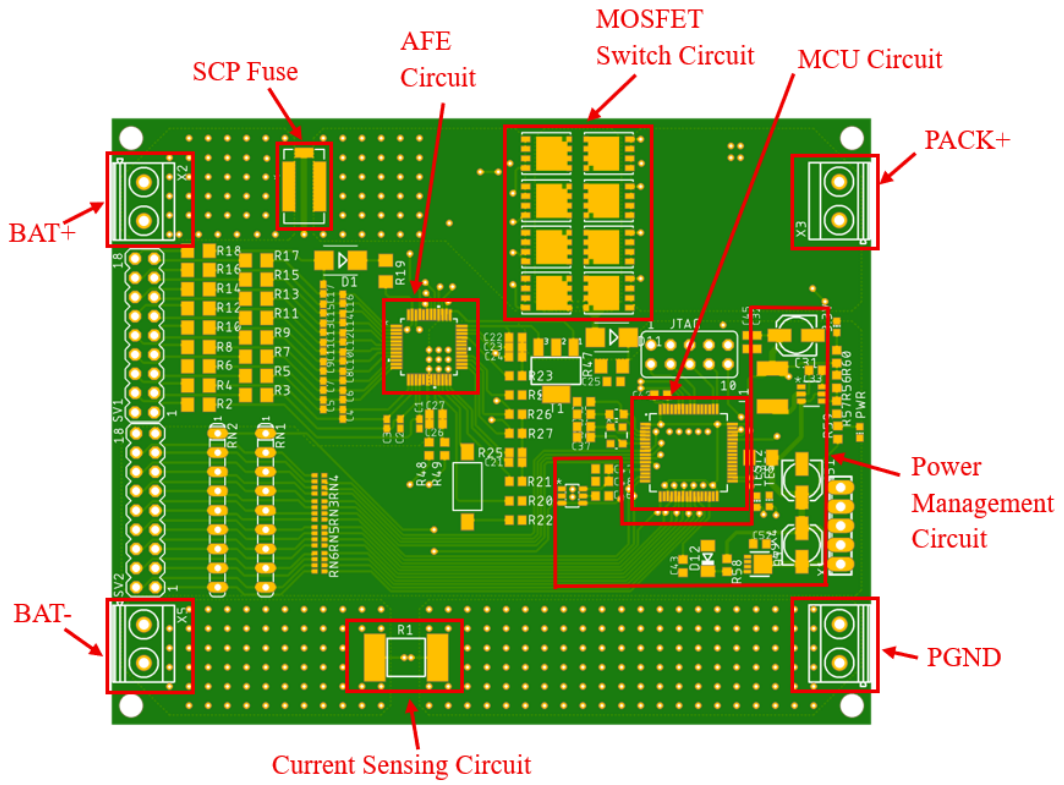

FIGURE B.1: Top-layer PCB layout showing the main functional blocks of the BMS

B.2 Bottom Layer PCB Layout

Figure B.2 presents the bottom-layer layout of the PCB. This layer hosts supporting circuits such as the CAN transceiver, NTC temperature sensing interface, and short-circuit protection (SCP) fuse components. It also serves as a return path through large ground copper pours to improve signal integrity and reduce impedance.

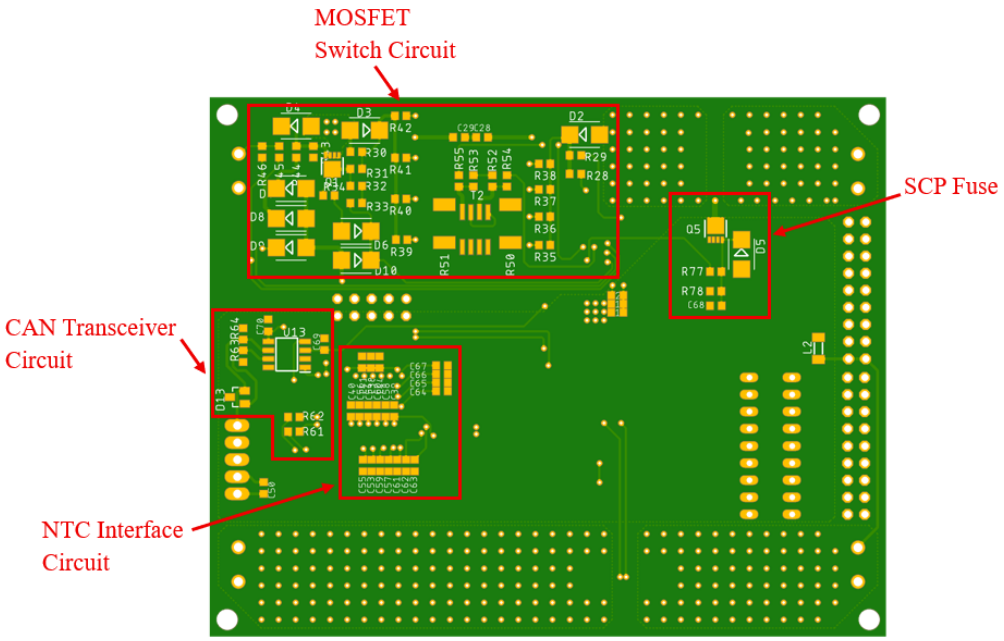

FIGURE B.2: Bottom-layer PCB layout showing support circuits and ground routing

B.3 PCB Routing and Copper Distribution

Figure B.3 illustrates the complete PCB routing with top and bottom copper layers, including power polygons and ground pours. High-current paths are implemented using wide copper areas to reduce resistive losses and thermal stress, while signal traces are routed to minimize coupling and electromagnetic interference.

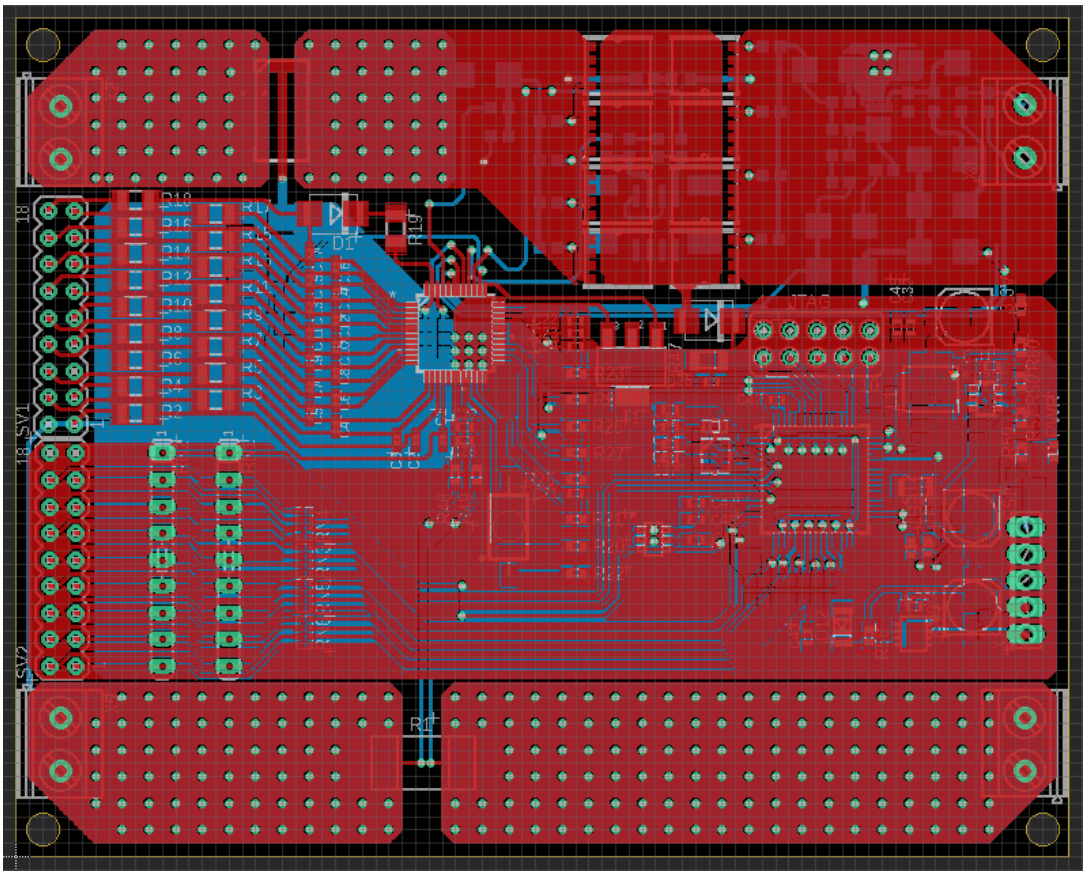

FIGURE B.3: Complete PCB routing showing top and bottom copper layers and power polygons

Bibliography

[1] D. Linden and T. B. Reddy, *Handbook of Batteries*. New York: McGraw-Hill, 2010.

[2] G. L. Plett, *Battery Management Systems, Volume 1: Battery Modeling*. Norwood, MA: Artech House, 2015.

[3] Y. Wu, *Lithium-Ion Batteries: Fundamentals and Applications*. CRC Press, 2015.

[4] J. M. B. Systems, *Our Guide to Batteries*. Johnson Matthey Battery Systems, 2015.

[5] J. S. Newman, *Electrochemical Systems*. Englewood Cliffs: Prentice-Hall, 2nd ed., 1991.

[6] T. Fuller, M. Doyle, and J. Newman, "Simulation and optimization of the dual lithium ion insertion cell," *Journal of the Electrochemical Society*, vol. 141, pp. 1–10, 1994.

[7] M. Doyle, T. Fuller, and J. Newman, "Importance of the lithium ion transference number in lithium/polymer cells," *Electrochimica Acta*, vol. 39, pp. 2073–2081, 1993.

[8] T. Fuller, M. Doyle, and J. Newman, "Relaxation phenomena in lithium-ion-insertion cells," *Journal of the Electrochemical Society*, vol. 141, pp. 982–990, 1994.

[9] C. Y. Wang and V. Srinivasan, "Computational battery dynamics (cbd)-electrochemical/thermal coupled modeling and multi-scale modeling," *Journal of Power Sources*, vol. 110, pp. 364–376, 2002.

[10] M. Doyle and Y. Fuentes, "Computer simulations of a lithium-ion polymer battery and implications for higher capacity next-generation battery designs," *Journal of the Electrochemical Society*, vol. 150, pp. 706–713, 2003.

[11] V. R. Subramanian, V. Boovaragavan, V. Ramadesigan, and M. Arabandi, "Mathematical model reformulation for lithium-ion battery simulations: Galvanostatic boundary conditions," *Journal of the Electrochemical Society*, vol. 156, pp. 260–271, 2009.

[12] J. P. Wang, Q. S. Chen, and B. G. Cao, "Support vector machine based battery model for electric vehicles," *Energy Conversion and Management*, vol. 47, pp. 858–864, 2006.

[13] J. P. Wang, L. Xu, J. G. Guo, and L. Ding, "Modelling of a battery pack for electric vehicles using a stochastic fuzzy neural network," *Journal of Automobile Engineering*, vol. 223, pp. 27–35, 2009.

[14] M. Chen and G. A. Rincon-Mora, "Accurate electrical battery model capable of predicting runtime and i-v performance," *IEEE Transactions on Energy Conversion*, vol. 21, pp. 504–511, 2006.

[15] G. L. Plett, "Extended kalman filtering for battery management systems of lipb-based hev battery packs, part 2. modeling and identification," *Journal of Power Sources*, vol. 134, pp. 262–276, 2004.

[16] X. Hu, S. Li, and H. Peng, "A comparative study of equivalent circuit models for li-ion batteries," *Journal of Power Sources*, vol. 198, pp. 359–367, 2012.

[17] W. He, N. Williard, M. Osterman, and M. Pecht, "Prognostics of lithium-ion batteries based on dempster–shafer theory and the bayesian monte carlo method," *Journal of Power Sources*, vol. 196, no. 23, pp. 10314–10321, 2011.

[18] J. Vetter, P. Novák, M. R. Wagner, *et al.*, "Ageing mechanisms in lithium-ion batteries," *Journal of Power Sources*, vol. 147, no. 1–2, pp. 269–281, 2005.

[19] A. Barré, B. Deguilhem, S. Grolleau, M. Gerard, F. Suard, and D. Riu, "A review on lithium-ion battery ageing mechanisms and estimations for automotive applications," *Journal of Power Sources*, vol. 241, pp. 680–689, 2013.

[20] R. Xiong, H. He, Y. Peng, and F. Sun, "A double-layer kalman filtering based parameter and state estimation approach for advanced lithium-ion battery management systems," *Energy*, vol. 121, pp. 739–750, 2017.

[21] W. Q. T. Kim and L. Qu, "Real-time estimation of battery power capability under uncertainty using an electro-thermal model," in *2016 IEEE Transportation Electrification Conference and Expo (ITEC)*, pp. 1–6, 2016.

[22] S. F. Schuster, T. Bach, E. Fleder, J. Müller, M. M. Fleischer, M. Sextl, and A. Jossen, "Nonlinear aging characteristics of lithium-ion cells under different operational conditions," *Journal of Energy Storage*, vol. 1, pp. 44–53, 2015.

[23] J. Smith, *Battery Management Systems: Design and Implementation.* New York, NY: TechPress Publishing, 2018.

[24] R. Jones and S. Patel, "Advances in battery monitoring for electric vehicles," in *Proceedings of the 10th International Conference on Power Systems*, pp. 50–55, 2019.

[25] K. C. P. Lee and R. Zhang, "Battery thermal management in electric vehicles," *Journal of Energy Systems*, vol. 32, no. 4, pp. 123–135, 2021.

[26] M. P. A. Kumar and V. Gupta, "Current sensing and isolation in battery management systems," *Journal of Power Electronics*, vol. 28, no. 2, pp. 234–245, 2022.

[27] T. Instruments, "bq76952: 3- to 15-cell battery monitor and protection ic," in *Texas Instruments Technical Documentation*, 2019.

[28] X. W. L. Zhao and T. Liu, "Battery management system algorithms for soc and soh estimation," *International Journal of Battery Technologies*, vol. 18, no. 6, pp. 456–467, 2020.

[29] F. Harris and J. Stevens, "Balancing techniques in battery management systems: Passive vs active," *Battery Technology Review*, vol. 24, no. 3, pp. 112–120, 2019.

[30] H. B. G. Adams and T. Green, "Communication protocols in battery management systems," *Journal of Embedded Systems*, vol. 21, no. 1, pp. 45–56, 2018.

[31] M. Clark, "Fault detection and logging in bms design," in *Proceedings of the International Battery Conference*, pp. 98–107, 2021.

[32] H. Miller and R. Turner, "Voltage sensing techniques in battery monitoring systems," *Sensors and Actuators*, vol. 34, no. 5, pp. 789–801, 2017.

[33] S. M. D. Walker and F. Torres, "Current measurement techniques for battery management," *Power Electronics Journal*, vol. 15, no. 2, pp. 122–134, 2019.

[34] A. W. L. Davis and G. Bell, "Thermal management in li-ion batteries," *Thermal Science and Engineering*, vol. 19, no. 4, pp. 67–78, 2020.

[35] M. Johnson and S. Lee, "Active balancing techniques for battery equalization," *Energy Storage Journal*, vol. 40, no. 2, pp. 134–142, 2021.

[36] R. Anderson and K. Moore, "Forward-flyback converter applications in battery equalization," *Power Conversion Technology Review*, vol. 8, no. 3, pp. 56–67, 2022.

[37] A. T. J. Harris, "Passive balancing for battery management systems: A cost-effective solution," *Journal of Energy Management*, vol. 11, no. 1, pp. 32–45, 2019.

[38] T. Smith and R. Nelson, "Precharge control in high-voltage battery systems," in *Journal of Power Systems*, pp. 54–63, 2020.

[39] M. H. A. Wright and T. Taylor, "Safety features in battery management systems," *Safety and Reliability Journal*, vol. 27, no. 2, pp. 98–110, 2018.

[40] J. M. Aden Seaman, Thanh-Son Dao, "A survey of mathematics-based equivalent-circuit and electrochemical battery models for hybrid and electric vehicle simulation," *Journal of Power Sources*, vol. 256, pp. 410–423, 2014.

[41] M. Tekin and M. İhsan Karamangil, "Comparative analysis of equivalent circuit battery models for electric vehicle battery management systems," *Journal of Energy Storage*, vol. 86, p. 111327, 2024.

[42] H. Rahimi-Eichi, U. Ojha, F. Baronti, and M.-Y. Chow, "Battery management system: An overview of its application in the smart grid and electric vehicles," *IEEE Industrial Electronics Magazine*, vol. 7, no. 2, pp. 4–14, 2013.

[43] S. Piller, M. Perrin, and A. Bürke, "Methods for state-of-charge determination and their applications," *Journal of Power Sources*, vol. 96, pp. 113–120, 2001.

[44] X. Hu, S. Li, and H. Peng, "Battery state-of-charge estimation in electric vehicles: A review," *IEEE Transactions on Vehicular Technology*, vol. 64, pp. 100–118, 2015.

[45] R. e. a. Xiong, "Battery management system for electric vehicles—a review," *Journal of Power Sources*, 2018.

[46] H. e. a. He, "State-of-charge estimation of batteries using neural network modeling and unscented kalman filter," *Applied Energy*, 2012.

[47] I. e. a. Baccouche, "Implementation of a coulomb counting algorithm for soc estimation of li-ion battery," in *12th International Multi-Conference on Systems, Signals & Devices*, 2015.

[48] Y. Shen, "State of charge estimation of batteries: A review," *Renewable and Sustainable Energy Reviews*, 2012.

[49] O. Tremblay and L.-A. Dessaint, "A generic battery model for the dynamic simulation of hybrid electric vehicles," in *IEEE Vehicle Power and Propulsion Conference*, 2007.

[50] M. Chen and G. Rincon-Mora, "Accurate electrical battery model capable of predicting runtime and i–v performance," in *IEEE Transactions on Energy Conversion*, 2006.

[51] F. e. a. Sun, "Adaptive extended kalman filter for state of charge estimation of lithium-ion batteries," *Applied Energy*, vol. 96, pp. 201–210, 2011.

[52] G. Plett, "Extended kalman filtering for battery management systems," *Journal of Power Sources*, vol. 134, pp. 252–261, 2004.

[53] X. e. a. Feng, "A review of thermal management for lithium-ion batteries," *Energy Storage Materials*, vol. 10, pp. 246–267, 2018.

[54] S. Piller, M. Perrin, and A. Jossen, "Methods for state-of-charge determination and their applications," *Journal of Power Sources*, vol. 96, no. 1, pp. 113–120, 2001.

[55] L. Lu, X. Han, J. Li, J. Hua, and M. Ouyang, "A review of the key issues for lithium-ion battery management in electric vehicles," *Journal of Power Sources*, vol. 226, pp. 272–288, 2013.

[56] W. Waag, C. Fleischer, and D. U. Sauer, "Critical review of the methods for monitoring of lithium-ion batteries in electric and hybrid vehicles," *Journal of Power Sources*, vol. 258, pp. 321–339, 2014.

[57] R. Xiong, Q. Yu, H. Chen, and C. Wang, "Lithium-ion battery health diagnosis: A systematic review," *IEEE Access*, vol. 6, pp. 28005–28017, 2018.

[58] J.-M. Tarascon and M. Armand, "Issues and challenges facing rechargeable lithium batteries," *Nature*, vol. 414, pp. 359–367, 2010.

[59] T. Nagaura and K. Tozawa, "Lithium ion rechargeable battery," *Progress in Batteries & Solar Cells*, vol. 9, pp. 209–217, 1990.

[60] Panasonic Corporation, "Lithium-ion nmc 18650 cell datasheet," 2020. Accessed: 2025-02-01.

[61] J. Zhang *et al.*, "A review on distributed battery management systems for electric vehicles," *Applied Energy*, vol. 240, pp. 918–934, 2019.

[62] Texas Instruments, *BQ76952: 3-16 Cell Battery Monitor and Protector*, 2021. Accessed: 2025-02-01.

[63] Renesas Electronics, *ISL94216: 16-Cell Battery Monitor and Balancer*, 2019. Accessed: 2025-02-01.

[64] Autodesk, *Autodesk Eagle PCB Design Software*, 2023.

[65] Texas Instruments, *TINA-TI SPICE Simulation Tool*, 2022.

[66] D. Linden, T. Reddy, and G. Jurgen, *Battery Management Systems for Large Lithium-Ion Battery Packs*. Artech House, 2017.

[67] Analog Devices, *MAX14921: 12-Channel High-Voltage Battery-Cell Monitor*, 2020. Accessed: 2025-02-01.

[68] Texas Instruments, *BQ76952 Technical Reference Manual*, 2023.

[69] STMicroelectronics, *STM32H563/573 Microcontroller Datasheet*, 2023.

[70] STMicroelectronics, *STM32H5 Reference Manual*, 2023.

[71] E. Systems, *ESP32-WROOM-32E Datasheet*, 2022.

[72] STMicroelectronics, *STM32F303RB Datasheet*, 2018.

[73] T. Instruments, *MSP430FR2155 Microcontroller Datasheet*, 2021.

[74] STMicroelectronics, *STM32H5 Hardware Design Guidelines*, 2023.

[75] "Iso 11898-2: Road vehicles — controller area network (can) — part 2: High-speed medium access unit," 2016.

[76] N. Semiconductors, *TJA1042 High-speed CAN Transceiver Datasheet*, 2021.

[77] Nexperia, *PESD1CAN ESD Protection Diode Datasheet*, 2019.

[78] "Can bus logic levels explained," 2020.

[79] V. Intertechnology, *WSK1216 Kelvin-Connected Power Shunt Resistor*, 2022.

[80] V. Intertechnology, *NTCLE203E3 Series NTC Thermistors*, 2020. Datasheet.

[81] STMicroelectronics, *STM32 Microcontroller ADC Peripheral — Application Note AN2834*, 2022. ST Application Note.

[82] T. Instruments, *Power MOSFET Basics*, 2020. Application Note.

[83] STMicroelectronics, *STL110N10F7 Power MOSFET*, 2021. Datasheet.

[84] T. Instruments, *Designing MOSFET Power Switches for Battery Protection*, 2019. Application Note.

[85] T. Instruments, *Precharge Circuit Design Guide for Battery Packs*, 2017. Application Note.

[86] T. Connectivity, *Managing Inrush Current in High-Voltage Contactor Systems*, 2020. Technical White Paper.

[87] I. Technologies, *Design Considerations for Electric Vehicle Battery Packs*, 2021. Design Guide.

[88] A. S. Sedra and K. C. Smith, *Microelectronic Circuits*. Oxford University Press, 7th ed., 2014.

[89] T. Instruments, *BQ76952: 3-Series to 16-Series High-Voltage Battery Monitor*, 2020.

[90] I. Technologies, *Power MOSFET Basics*, 2019.

[91] N. Semiconductors, *Power Electronics for Electric Vehicles*, 2021.

[92] L. Balogh, *Design and Application Guide for High-Side MOSFETs*, 1999.

[93] O. Semiconductor, *MOSFET Thermal Characteristics and Safe Operating Area*, 2018.

[94] R. Boylestad, *Design Fundamentals for Power Electronics*, 2017. Pearson Education.

[95] T. Instruments, *Reverse Polarity Protection Using a MOSFET*, 2016.

[96] "Road vehicles — electrical disturbances from conduction and coupling," 2011.

[97] Littelfuse, *ITV9550 Series Resettable Fuse*, 2023. Datasheet.

[98] D. A. Andrea, *Battery Management Systems for Large Lithium-Ion Battery Packs*. Artech House, 2010.

[99] T. Instruments, *BQ769x2 Technical Reference Manual*, 2022.

[100] S. Piller, M. Perrin, and A. Jossen, "Methods for balancing lithium-ion batteries: A comparative review," *Journal of Power Sources*, vol. 154, pp. 330–344, 2006.

[101] T. Instruments, *LMR51430 4-V to 36-V, 3-A Synchronous Buck Converter Datasheet*, 2022.

[102] O. Semiconductor, *Automotive-Grade Schottky Diodes Overview*, 2021.

[103] A. Devices, *Voltage Reference Basics and Best Practices*, 2019.

[104] Nexperia, *PSMN013-30MLC Automotive MOSFET Datasheet*, 2021.

[105] T. Instruments, *Designing Robust Automotive Front-End Power Supplies*, 2020.

[106] W. Zheng, B. Xia, W. Wang, Y. Lai, M. Wang, and H. Wang, "State of charge estimation for power lithium-ion battery using a fuzzy logic sliding mode observer," *Energies*, vol. 14, p. 14, 2019.

[107] P. Shanthraj, P. Eisenlohr, M. Diehl, and F. Roters, "Numerically robust spectral methods for crystal plasticity simulations of heterogeneous materials," *International Journal of Plasticity*, vol. 66, pp. 31–45, 2015.

[108] U. R. Kiran, A. Panchal, M. Sankaranarayana, G. N. Rao, and T. Nandy, "Effect of alloying addition and microstructural parameters on mechanical properties of 93% tungsten heavy alloys," *Materials Science and Engineering: A*, vol. 640, pp. 82–90, 2015.

[109] A. Jahan, K. L. Edwards, and M. Bahraminasab, *Multi-criteria decision analysis for supporting the selection of engineering materials in product design*. Butterworth-Heinemann, 2016.

[110] M. Doyle, T. Fuller, and J. Newman, "Importance of the lithium ion transference number in lithium/polymer cells," *Electrochimica Acta*, vol. 39, pp. 2073–2081, 1994.

[111] V. R. Subramanian, V. Boovaragavan, V. Ramadesigan, and M. Arabandi, "Mathematical model reformulation for lithium-ion battery simulations: Galvanostatic boundary conditions," *Journal of the Electrochemical Society*, vol. 156, pp. 260–271, 2009.

[112] J. P. Wang, Q. S. Chen, and B. G. Cao, "Support vector machine based battery model for electric vehicles," *Energy Conversion and Management*, vol. 47, pp. 858–864, 2006.

[113] J. P. Wang, L. Xu, J. G. Guo, and L. Ding, "Modelling of a battery pack for electric vehicles using a stochastic fuzzy neural network," *Journal of Automobile Engineering*, vol. 223, pp. 27–35, 2009.

[114] STMicroelectronics, *STM32H563xx Microcontroller Reference Manual*, 2023.

[115] E. Systems, *ESP32-WROOM-32E Datasheet*, 2022.

[116] N. Semiconductors, *TJA1042 High-Speed CAN Transceiver Datasheet*, 2020.

[117] Nexperia, *ESD Protection for Power MOSFET Circuits*, 2020. Application Note.

[118] O. Semiconductor, *Reverse Battery Protection Using a MOSFET*, 2018. Application Note.

[119] Littelfuse, *TVS Diode Selection Guide for Automotive Power Lines*, 2022. Design Guide.

[120] IPC, *IPC-2221: Generic Standard on Printed Board Design*. IPC International, 2019.

[121] I. Group, *FR-4 Laminate Material Datasheet*, 2020.

[122] T. Instruments, *PCB Layout Guidelines for Mixed-Signal Systems*, 2017.

[123] A. Devices, *AN-1142: PCB Layout Guidelines for Low-Noise Analog Circuits*, 2021.

[124] T. Instruments, *Design Considerations for Electric Vehicle Battery Management Systems*, 2020.

[125] IPC, *IPC-7351: Generic Requirements for Surface Mount Design and Land Pattern Standard*, 2018.

[126] IPC, *IPC-2152: Standard for Determining Current-Carrying Capacity in Printed Board Design*, 2010.

[127] T. Instruments, *High-Side Current Shunt Monitoring: PCB Layout Guidelines*, 2018.

[128] A. Devices, *Shunt Resistor Current Sensing: Best PCB Layout Practices*, 2019.